UNIVERSITY OF SOUTHAMPTON

Faculty of Engineering & Applied Science

TOPOLOGY AND MORPHOLOGY OF PULMONARY ANATOMICAL FEATURES FOR AEROSOL DEPOSITION APPLICATIONS USING MEDICAL IMAGING

by

Véronique Sauret

A thesis submitted for the degree of

Doctor of Philosophy

Department of Electronics & Computer Science

September 2000

UNIVERSITY OF SOUTHAMPTON

ABSTRACT

FACULTY OF ENGINEERING & APPLIED SCIENCE
DEPARTMENT OF ELECTRONICS & COMPUTER SCIENCE

Doctor of Philosophy

TOPOLOGY AND MORPHOLOGY OF PULMONARY ANATOMICAL FEATURES FOR AEROSOL DEPOSITION APPLICATIONS USING MEDICAL IMAGING

by Véronique Sauret

In inhalation therapy, aerosol deposition studies play a significant role in developing our understanding of the correlation between deposition site in the lungs and clinical effect to the patient. Pulmonary aerosol deposition distribution can be assessed by radionuclide imaging. It can also be predicted using computer-modelling of the particle paths in the airways. Both techniques, however, use anatomical models of the airways that lack three-dimensional (3D) reality, as little information is available on airway topology. Consequently, they cannot relate the aerosol deposition distribution to the subject's own anatomy. The thesis is concerned with the improvement of these methods.

An algorithm is developed to obtain the 3D topology and morphology of the airways, from computed tomography (CT) imaging. Realistic 3D airway models are then created by reconstructing the CT image of the airway tree and assigning a different intensity to each airway or to each airway generation. These methods are applied to the CT images of a human tracheobronchial tree cast and of a volunteer. Modelling of realistic 3D pulmonary lobes and segments, based on a region growing process to simulate the "fight for space" that occurs during lung formation, is attempted and applied to the volunteer's magnetic resonance lung images. The aerosol deposition distribution in two radionuclide imaging studies performed on the volunteer is then assessed, using the models representing his own anatomy.

The algorithm quickly provides data on the 3D topology and morphology of the airways, from both *in vivo* and cast analysis, that contribute to the knowledge of the lung anatomy. A non-planar geometry of the airways at bifurcations and clear lobar patterns are shown in the central airways of the datasets studied. The tabulated data and the 3D models of the airways are useful to predict the 3D aerosol deposition and simulate flow patterns in the airways. The study demonstrates that better knowledge of the anatomy allows improved interpretation of the aerosol deposition. A vertical gradient of the concentration of aerosol, increasing from the upper to the lower lobes, is quantified.

Contents

List of Figures

List of Tables

Acknowledgements

I would like to thank my two supervisors, Professor Adrian G. Bailey and Dr. John S. Fleming, for offering me a comprehensive academic training through a research subject that challenged my brain cells so much, and for their helpful advice and encouragement during the three years. I am indebted to Dr. Fleming for sharing his expertise in Nuclear Medicine imaging and Aerosol Deposition during extensive discussions and for communicating his enthusiasm.

I am grateful to Dr. Keith Goatman of the Department of Medical Physics and Bioengineering, who helped me with numerous computing queries and very valuable discussions on the work, and who gave general support. I am also grateful to Mr. Peter Halson for answering other computing questions and showing interest in my work.

Dr. Sonka of the Department of Electrical Engineering, Iowa University, sent us the thinning algorithm that forms the foundation of the algorithm developed in Chapter 4. Mr. Boggust of the Department of Medical Physics and Bioengineering built the phantom object (Fig. 4-2). Mr. Halson organised the use of the CT scanner for the *in vivo* anatomical investigation and wrote the imaging protocol (Section 5.2). Dr. Brown of the Department of Cardiothoracic Radiology, assisted with the CT scan and with the manual segmentation of the airways and lobes (Sections 5.2 and 6.2.4).

I am grateful to Professor Caro of the Department of Biological and Medical Systems, Imperial College, for his critical reading of Chapter 5, to Professor Kauczor of the Department of Radiology, Mainz University and Dr. Tastevin of the Department of Physics, Ecole Nationale Superieure, for their very valuable views on hyperpolarized Helium MR imaging.

I would like to thank my family for all the love and continuous support given throughout this work, as always. This thesis is dedicated them.

I would like to thank my friends: I have appreciated their encouragement and all the visits, phone calls, dances, meals, strolls, squash games and Scrabble games.

I acknowledge the financial assistance provided by the Department of Electrical Engineering, Southampton University and the Departments of Medical Physics and Bioengineering and Nuclear Medicine, Southampton General Hospital.

Abbreviations

2D Two-Dimensional

3D Three-Dimensional

B Pulmonary Segmental Bronchus

CFD Computational Fluid Dynamics

CT X-ray Computed Tomography

d.f. Degree Of Freedom

L Left

LB Lobar Bronchus

LL Left Lower

LU Left Upper

MR Magnetic Resonance imaging

PET Positron Emission Tomography

R Right

RM Right Middle

RL Right Lower

ROI Region Of Interest

RU Right Upper

S Pulmonary Segment

SD Standard Deviation

se Standard Error

SPECT Single Photon Emission Computed Tomography

Chapter 1

Introduction

1.1 Need Of Pulmonary Anatomical Models For Therapeutic Aerosol Deposition Applications

Aerosolised medications (powder or droplets) and nebulisation therapy (atomised liquid) are replacing both orally administered and intravenously or intramuscularly injected drugs, in the treatment of respiratory diseases and some systemic circulation disorders in humans. The lungs are the target organ for the aerosol delivery of, for instance, bronchodilators and bronchoconstrictors, used in asthma to reverse bronchospasm and diagnose airway hyper-responsiveness. Antibiotics for the treatment of infection in cystic fibrosis patients and for the prevention of infection in HIV-positive patients also aim for deposition in the lungs.

It is well-known that the effectiveness of aerosolised medications varies between patients; some being much improved, while others fail to improve. Variations in the dose of aerosol deposited within the lungs account for these failures in treatment but the effectiveness of therapies utilising inhaled aerosols cannot be compared unless the distribution of the deposition can be described [Laube (1996)]. For each clinical application, it is important to assess this deposition accurately in relation to the lung anatomy, to be able to identify the relationship between deposition site and clinical effect. In addition, such quantification has become an important economic issue in the last decade as it allows comparison of results among different laboratories and with different drug delivery devices.

The two approaches used for investigating the *in vivo* aerosol deposition in relation to the lung anatomy are (1) external measurements and (2) prediction computer-

modelling of the aerosol deposition. Both techniques use anatomical models of the airway tree. Such models have been created using physical measurements on lung casts to obtain measurements on lengths and diameters and information on average angles of branching. Data collection and analysis by these methods is tedious and very little topological information is available in the literature. Thus current models do not fully describe the airway anatomy in three dimensional space relative to a real lung shape. The lung space has also been partitioned into "regions of interest", however it is difficult to relate aerosol deposition in these areas to the patient's anatomy because of its large variability between subjects.

1.2 Objectives Of The Thesis And Contributions

This thesis is concerned with the development of realistic three-dimensional (3D) models of the airways, lobes and segments in the lungs, *in vivo*, using medical image data. The objectives are:

- to develop an automated method to tabulate airway dimensions and 3D orientation using medical image data.
- to collect pilot data on the spatial location of the central conductive airways in humans and analyse their use for 3D modelling.
- to create methods for realistically modelling airways, lobes and segments in the lungs.
- to investigate the use of the resulting models for assessing aerosol deposition radionuclide images, and to validate aerosol deposition predictions.

This study is a project within the Southampton Aerosol Group which is a multidisciplinary team from the Department of Electronics & Computer Science (formerly, Department of Electrical Engineering) at Southampton University and the Departments of Medical Physics and Bioengineering, Nuclear Medicine and University Medicine at Southampton General Hospital. Its researchers are working on the assessment of the deposition of inhaled aerosol in the lung airways using both computer modelling and 3D radionuclide imaging, but using simplified models of the lung. Our results are hoped to provide data to improve the 3D realism of the models. The new methods developed are also intended to be adapted for clinical studies of the fate of inhaled aerosols relating to the subject's anatomy. Moreover, our work will provide the scientific community with *in vivo* data, especially on the

topology of the airways, in both tabulated and imaged forms, which have several other biological and medical applications relating to lung anatomy and physiology.

1.3 Layout

The thesis is presented in seven chapters and one appendix.

Chapter 2 describes the structures constituting the human lungs, especially the lobes, segments and pulmonary airway tract. The different ways each anatomical feature has been modelled in the literature are reviewed, highlighting the lack of 3D reality of the current description of the airways.

Chapter 3 is concerned with pulmonary aerosol deposition. The physical mechanisms involved are presented. The methods to assess and predict aerosol deposition in the lungs are examined. This review shows how improvement in the 3D realism of the pulmonary anatomical models used could increase the clinical significance of the outcome of aerosol deposition studies.

Chapter 4 presents the algorithm that was developed to tabulate the morphometry and topology of the airways using 3D medical images. It is applied to test objects including a human tracheo-bronchial airway tree cast, as part of the validation study.

In Chapter 5, the algorithm is applied to *in vivo* 3D medical images, obtained from a scan that was performed on a volunteer. The orientation in space of the airways and dimensions are analysed, together with the cast data, from a 3D modelling point of view.

Chapter 6 describes the methods developed to realistically model the airways, lobes and segments in 3D. They are then applied to the volunteer's and cast data. The realism of the current model used at Southampton General Hospital is also evaluated.

Chapter 7 investigates the use of different anatomical models to assess the aerosol deposition distribution with respect to the volunteer's anatomy.

In Chapter 8 conclusions are drawn from our study and suggestions made for further work.

Appendix A contains the application that was submitted to the relevant Ethics Committee for the investigation on the volunteer and a copy of the approval.

Chapter 2

Description and modelling of the pulmonary anatomy

2.1 Introduction

This chapter first briefly summarises the human respiratory system and the measures of pulmonary function, that are defined by specific air volumes and capacities. The lobar and segmental structure of the lung, the bronchial tree and the acini are then detailed, including the anatomical information that medical imaging offers. The major works modelling the air spaces in the lungs are also reviewed.

2.2 Anatomy And Function Of The Respiratory System

The respiratory organs include the nose, pharynx, larynx, trachea, bronchi and lungs (Fig. 2-1). They act with the cardiovascular system to supply oxygen (O_2) and remove carbon dioxide (CO_2) from the blood. The conducting portion consists of a series of interconnecting cavities and tubes, namely the nose, pharynx, larynx, trachea, bronchi, bronchioles, and terminal bronchioles, that direct air into the lungs. The respiratory portion consists of those parts of the respiratory system where the exchange of gases occurs, namely the respiratory bronchioles, alveolar ducts, alveolar sacs, and alveoli.

The upper respiratory system refers to the nose and the pharynx. The nose warms, moistens and filters air and functions in olfaction and speech. The pharynx (throat) is a muscular tube lined by a mucous membrane. The upper part

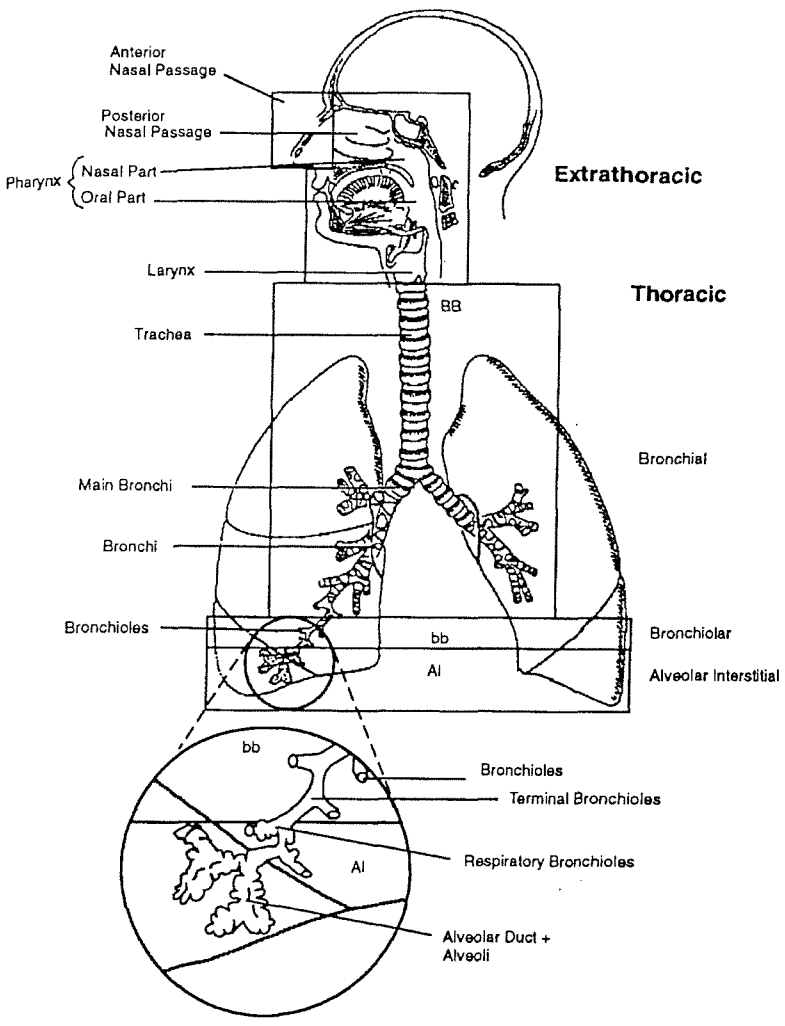

Figure 2-1: Anatomical regions of the respiratory tract (Reproduced by kind permission of the ICRP, from International Commission on Radiological Protection Task Group (1994)).

(nasopharynx) functions in respiration and acts as an impinger with the nose causing inhaled particles to impact on these structures. The middle and lower parts (oropharynx and laryngopharynx) are both a respiratory and a digestive pathway.

The lower respiratory system refers to the larynx, the trachea and all the bronchi down to alveoli. The larynx (voice box) is a short air passageway that connects the pharynx with the trachea. It contains the epiglottis which prevents food from entering the larynx, the thyroid cartilage (Adam's apple) and vocal folds. The airway from the trachea downwards is described in detail in the following sections.

2.3 Air Volumes And Capacities

The healthy adult averages 12 respirations a minute (one respiration is one inspiration plus one expiration, it is also called ventilation) and moves about 6 litres into and out of the lungs while at rest. A lower-than-normal volume of air exchanges is usually a sign of pulmonary malfunction. Figure 2-2 shows the various specific air volumes for an average adult [Tortora and Reynolds-Grabowski (1996)]. They however vary a lot depending on the size of the subject: larger volumes are found for males and young adults than for females, children and elderly. They are in general measured by spirometry.

About 500 ml of air (tidal volume V_T) moves into and then out of the airways with each inspiration and expiration during normal quiet breathing (tidal breathing). In an average adult, about 70%, i.e. 350 ml (spirometry measurements), of the tidal volume actually reaches the respiratory portion of the respiratory system and participates in respiration. The other 30%, i.e. 150 ml (anatomic dead space V_D), remains in air spaces of the conducting portion of the respiratory system (single-breath nitrogen washout). A rule of thumb is that the anatomic dead volume in ml is about the same as the person's weight in pounds.

By taking a very deep breath, the additional air, called inspiratory reserve volume, is about 3100 ml above the 500 ml of V_T for a total of 3600 ml. More air can be inhaled if inspiration follows forced expiration. Inhaling normally and then exhaling as forcibly as possible gives 1200 ml of air, the expiratory reserve volume, pushed out in addition of V_T. The FEV_1 is the volume of air that can be expelled from the lungs in 1 second with maximal effort following a maximal inhalation, i.e. the forced expiratory volume in 1 second. Even after the expiratory reserve volume is expelled, considerable air remains in the lungs because the alveoli are

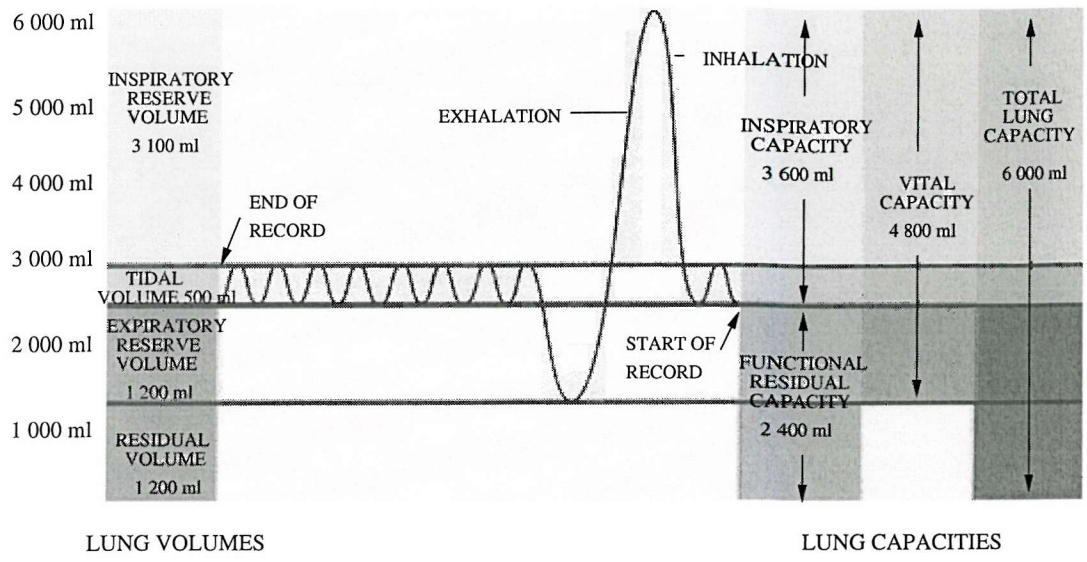

Figure 2-2: Typical air volumes in the respiratory system (Copyright ©1996 by Biological Sciences Textbooks, Inc. and S. Reynolds Gabrowski. Reprinted by permission of John Wiley & Sons., Inc., from Tortora and Reynolds-Grabowski (1996)).

always kept slightly inflated and some air also remains in the non collapsible airways. This volume is called the residual volume and amounts to about 1200 ml.

Lung capacities, the sum of two or more volumes, include functional residual (FRC) which is the sum of the residual volume plus expiratory reserve volume (2400 ml), and total lung capacity (TLC), which is the sum of all air volumes (6000 ml).

2.4 The Lungs

Lungs are paired organs in the thoracic cavity. The lung tissue contains the bronchi and the acini as well as blood and lymphatic vessels and nerves. The two lungs are separated from each other by the heart and other structures. The pleural membrane encloses and protects each lung. Both lungs extend from the diaphragm to just slightly inferior to the clavicles and lie against the ribs anteriorly and posteriorly. The surface of the lung lying against the ribs, the costal surface, is rounded to match the curvature of the ribs. The mediastinal (medial) surface of each lung contains a region, the hilum, through which bronchi, pulmonary blood

vessels, lymphatic vessels, and nerves enter and exit. The broad inferior portion of the lung, the base, is concave and fits over the convex area of the diaphragm. The narrow superior portion of the lung is termed apex (cupula). The cardiac notch is the name given to the concavity (depression) on the right hand side of the left lung, where the heart lies. The right lung is approximately 10% thicker and broader than the left. It is also somewhat shorter than the left because the diaphragm is higher on the right side to accommodate the liver that lies inferior to it.

The right lung has three lobes, namely right upper (RU), right middle (RM) and right lower (RL), separated by two fissures (pleural envelopes), one oblique and one horizontal; the left lung has two lobes, left upper (LU) and left lower (LL), separated by one oblique fissure. Ten substructures of lung tissue, called bronchopulmonary segments and independent from each other can be identified *ex vivo* in each lung. Morphogenesis of these structures is detailed in Section 6.2.2, page 114. The shape of each lobe and segment can be visualised from posterior, anterior and profile photographs of excised lungs in anatomical atlases (e.g. Fogelman and Maisey (1988)). Schematic views are illustrated in Netter (1991). All authors will however warn the reader about the great variability between subjects observed in both the size and the shape of the pulmonary lobes and segments. Unfortunately, no quantification of this variability has been found in the literature.

2.4.1 Imaging The Lungs

The *in vivo* size and shape of the lungs and its features can be viewed, to some extent, using medical imaging techniques.

X-ray imaging

X-rays have been used to produce medical images ever since their discovery in 1895. The images are formed by the interaction of X-ray photons with photon detectors. It is therefore a distribution of those photons which are transmitted through the patient and are recorded by the detectors.

For a given energy, the attenuation of the X-rays through bone is higher than that of soft tissue. In an image, the greater the difference between the two attenuation coefficients, the higher the contrast. Muscle and blood, for the typical diagnostic X-ray beam have about the same linear attenuation coefficient. Bone attenuates the beam almost three times more than blood and muscle. In a radiography of the

chest, the ribs, for example, show up as a light structure because they attenuate the X-ray beam more strongly than the surrounding soft tissue, so the X-ray film (i.e. photon detector) receives less exposure in the shadow of the bone. Correspondingly, the air-filled lungs show up as darker regions. An abnormality, such as hard tissue in the lungs, will therefore appear with high contrast. An inherent problem with the conventional radiograph is the loss of the depth information.

X-ray Computed Tomography

X-ray tomographic imaging has been developed to (i) be able to distinguish soft tissue and (ii) resolve spatially structures along the direction of X-ray propagation. It is known as X-ray Computed Tomography (CT) and is based on a sectional imaging of the patient, who lies in the CT scanner. A planar slice of the body is defined and X-rays are passed through it only in directions that are contained within, and are parallel to, the plane of the slice. The CT image is as though the slice had been physically removed from the body and then radiographed by passing X-rays through it in a direction perpendicular to its plane. The resulting images show the human anatomy in section with a spatial resolution of about a millimetre. The slices covering a given volume of the patient's anatomy are stacked on top of each other in a 3D volume (image). Transverse, coronal or sagittal slices of the CT volume can then be viewed. The method of converting the X-ray measurements into image such as Figure 6-6 is described in Webb (1988).

CT images provide clear anatomical detail to define the lung 3D limits at normal and quiet breathing when images are taken at 16 mm intervals (gap between two slices) with a beam width (slice thickness) of 8 mm. In this examination, the possible biological damage per unit dose of X-ray radiation to the lung tissue, i.e. the effective radiation dose, is estimated to 4.5 mSv [Perring et al. (1994)]. The concepts of radiation dose and effective radiation dose are explained in the Glossary (Effective Radiation Dose).

CT imaging has also been used to image the lobar fissures, defining the contours of the lobes. The locations of the fissures are inferred from areas of relatively sparse pulmonary vascularity and from the portions where the shadow created by the visceral pleural layers composing the fissures, is identifiable. The task remains rather difficult although imaging settings, such as no gap between slices and thin slices, ease the process. In some cases, indents in the lung outlines may be visible and help (or confuse!) the operator. Thus trained eyes are required. In practice,

lobar fissures are sought for only in part(s) of the lung rather than for the whole lung (e.g. Higashi (1998), Thompson et al. (1999)), as there is no direct clinical interest in having a picture detailing the five lobes in one scan.

Contours of the segments, because they are not defined by any material envelope enclosing them, cannot be imaged. However, estimation of their contours in part(s) of the lung has been documented using CT imaging. This is because a CT scan of a part of the lungs is used to further clarify abnormalities seen on X-ray film. CT then plays a major role in pre-operative planning to localise pathology as specifically as possible. Radiologists look first for the lobar fissures and lobar bronchi. Partition of the lobe into segments to define precisely the region of interest is then performed by identifying proximate segmental bronchi. Definition of the contours of the segments is based on the location and orientation of the latter, as well as on empirical knowledge of the shape and location of each segment [Thompson et al. (1999)].

Magnetic Resonance Imaging

To image the anatomy using Magnetic Resonance (MR) imaging, the subject is placed within a powerful magnet. Pulsed radio waves are then passed through the object. These radio waves cause atomic nuclei to emit weak radio signals which are detected and used to reconstruct MR images. These images can then be viewed as transverse, coronal or sagittal slices.

The magnetic resonance signal is the result of excitation of the individual magnetised protons within the object by irradiation with radiofrequency (RF) energy of a specific frequency. This energy absorption causes the displacement of the magnetic moment from equilibrium resulting in an excited system. As the system returns to equilibrium MR signals are emitted in proportion to the number of excited protons in the sample. The detection and acquisition of the signals constitute the basic information necessary for MR imaging. Details of the image reconstruction are described in Webb (1988).

When placed within a magnetic field, protons align parallel or anti-parallel to the magnetic field and "precess", i.e. the proton rotates about its axis. The frequency of the precession is dependent on the strength of the magnetic field and the properties of different tissues. The Larmor equation describes this relationship:

$$W_0 = \gamma \, B_0, \tag{2.1}$$

where W_0 is the precession frequency (Hz or MHz), γ is the gyro-magnetic ratio which has a value different for each material, and B_0 is the strength of the external magnetic field (Tesla, T).

Slightly more protons align parallel to the magnetic field than anti-parallel, creating a net magnetic moment aligned with or longitudinal to the external magnetic field. An RF pulse with the same frequency as the precessing protons can cause resonance, transferring energy to the protons. This results in more protons aligning anti-parallel thus reducing the longitudinal magnetisation. The RF frequency pulse also causes the protons to precess in phase. This results in a new magnetic vector, the transverse magnetisation. When the RF pulse is turned off, longitudinal magnetisation increases again. The time for this vector to be restored is called the longitudinal relaxation time, or T1. Transverse magnetisation also decreases and disappears; transverse relaxation is described by the time constant T2.

The time T1 is longer than T2 and the ratio T1:T2 characterises different structures. Water and liquids have a long T1 and a long T2. Fats have a short T1 and a short T2. In general the higher the water content of the tissue, the longer the relaxation times. T1 depends on tissue composition and structure. Energy transfer is difficult in a pure liquid/water lattices, therefore the relaxation times are longer. Fats have a short relaxation period due to carbon bonds in fatty acids, facilitating effective energy transfer. The strength of the magnetic field also influences T1: the stronger the magnetic field, the longer the T1. Tissue contrast sensitivity can be obtained by exploiting the differences in T1 and T2.

MR volume image using a T1-weighted procedure (T1-weighted MR image) also gives the outlines of the lungs in 3D (e.g. Fleming et al. (1996b)). Such images have been obtained by RF pulse sequences designed to emphasise the T1 characteristics of tissues, whilst de-emphasising the T2 characteristics. Two RF pulses are sent in successively. If the second pulse is sent in after longitudinal relaxation has recovered, the signal received for imaging will be the same (TR_{long}). Different tissues have different relaxation times, as already discussed. Therefore, if the second pulse is sent after a shorter time (TR_{short}), longitudinal relaxation will not have time to recover in some tissues, thus emitting a different signal for different tissues. A T1-weighted image will thus be valuable to view anatomical structures. The image is required in the same plane as where the RF was sent in. Therefore, moving fluids, such as blood, will not be imaged.

MR imaging has the advantage over CT of being radiation free. Breathing motion and heart beating that may blur the images can be gated, i.e. the images are performed always at the same time in the breathing or cardiac cycle by monitoring them.

2.4.2 Modelling The Lungs

Three dimensional atlas image volumes (3D models), based on *in vivo* tomographic imaging of the lung outlines have recently been developed. Their general purpose is to describe the pulmonary lobes and segments to then simulate for instance ventilation, perfusion or aerosol deposition in each lobe or segment. These images, in turn, allow studies of various aspects of their interpretation, such as the quality of the image processing. Their principal advantage is then to minimise *in vivo* studies that may be of no benefice to the volunteers and expensive. Moreover, anatomical defects can be simulated and their effect studied.

To our knowledge, the only one published was from a collaborative work at Sydney. Their model was based on the lung outlines segmented out from a CT scan performed on a man of height of 178 cm and weighing 70 kg in supine position. The lobar fissures were then marked by an experienced radiologist, using patient CT data that showed the interlobar fissures. The lobes were a guide to the segments. The segmental bronchi of human cadavers lungs were injected with colour-coded dyes. They were finely sectioned and digitised. The lobar and segmental boundaries were transferred to the phantom dataset with reference to anatomical books [Magnussen et al. (1997)]. Since the segmental model merged information from several subjects, it could be viewed as an "average" model. A year later, a segmental model was also developed at Southampton General Hospital. The lung outlines were segmented out from a T1-weighted MR study performed on a healthy male volunteer in supine position. Partition of the lung space into the various pulmonary segments was done with reference to a tracheobronchial tree cast of which the airways belonging to a same segment are painted with the same colour. The cast anterior, posterior, right lateral and left lateral views are illustrated in Fogelman and Maisey (1988). For each view, the outlines of the segments were stretched to match the subject's lung outlines. The boundary of each segment was then drawn manually, on each slice of the 3D volume, proportionally to the distances that were measured on the 2D illustrations [Salam (1998)]. The Southampton model, which is referred to, in the thesis, as the in-house model, is

shown in Figure 2-3 and the relative sizes of the segments is given in Table 6.2. As the construction relies only on the cast segment position, size and shape, except for the lung outlines, the in-house model could be viewed as a "standard" model.

2.5 The Bronchial Tree

The trachea, primary bronchi, secondary bronchi, tertiary bronchi, bronchioles, and terminal bronchioles form the bronchial tree (Fig. 2-1). They are also referred to as the conducting airways.

2.5.1 Anatomy Of The Bronchial Tree

Figure 2-4 shows the branching structure of the bronchial tree. Because it resembles a tree trunk with its branches, the vocabulary to describe relationships between the airways is often analogous to those in a family tree (e.g. parent branch, daughter branches/children, generations).

The trachea (windpipe) extends from the larynx to the superior border of the fifth vertebra (T5). It is a tubular passageway for air about 12 cm in length and 2.5 cm in diameter. It is composed of C-shaped rings of cartilage, smooth muscle and is lined with pseudo-stratified ciliated columnar epithelium (mucosa). The 16-20 incomplete rings of cartilage are arranged horizontally and stacked one on top of another. They may be felt through the skin inferior to the larynx. Transverse smooth muscle fibres and elastic connective tissue hold the open ends of the cartilage rings together. The solid C-shaped cartilage rings provide a semirigid support so the tracheal wall does not collapse inward (especially during inspiration) and obstruct the air passageway. The epithelium provides the same protection against dust as the membrane lining the nasal cavity and larynx.

At the point where the trachea divides into right and left primary bronchi (superior border of the fifth thoracic vertebra), there is an internal ridge called the carina, the mucous membrane of which is one of the most sensitive areas of the entire larynx and trachea for triggering a cough reflex. The right primary bronchus goes into the right lung and the left primary bronchus, less vertical, longer and narrower than the right, goes into the left lung. On entering the lungs, the primary bronchi divide to form smaller bronchi -the secondary (lobar) bronchi-, one for each lobe of the lung. The secondary bronchi continue to branch, forming still smaller

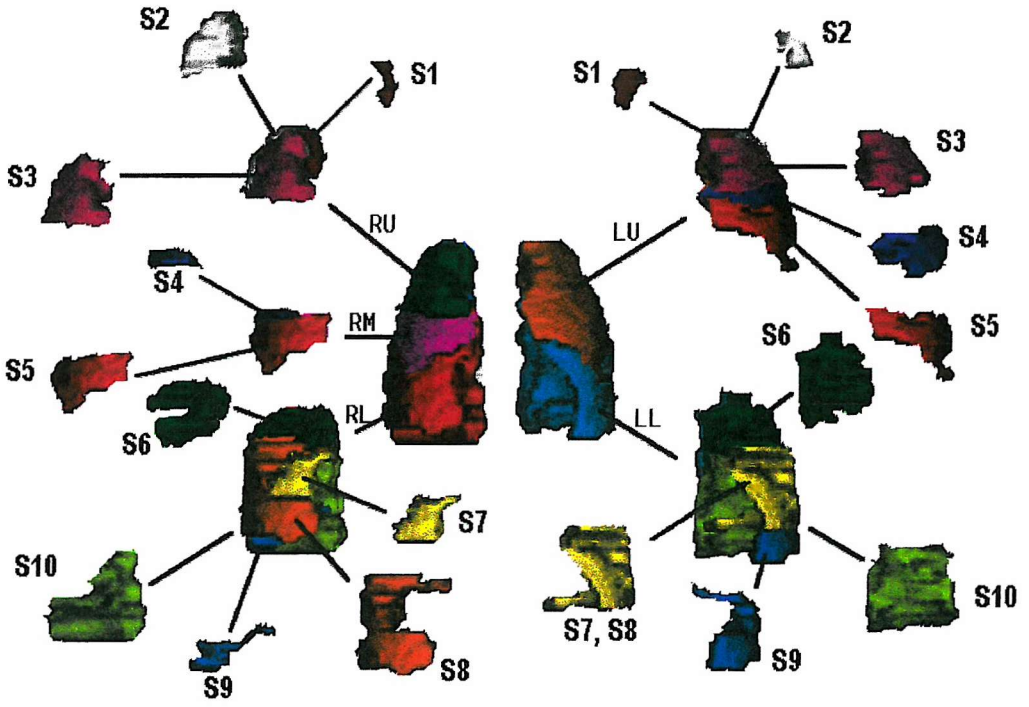

Figure 2-3: Southampton General Hospital (SGH) segmental model. The segmental partition of the lungs was done manually with reference to a segment-colour-coded tracheobronchial tree cast. *Legend*: RU, RM, RL, LU and LL correspond to the five lobes of the lungs, S1 to S10 partition the lobes further into the segments (see text, Section 2.4).

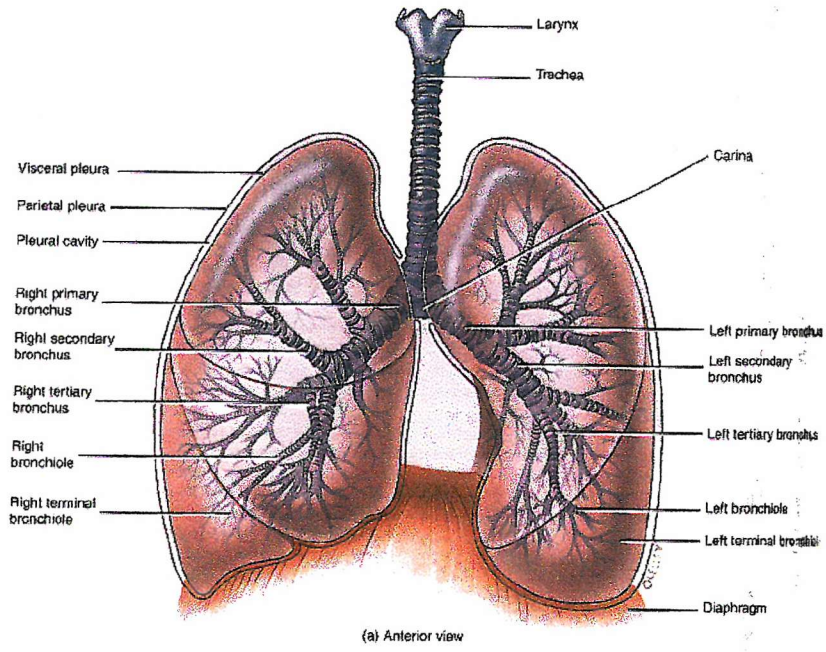

Figure 2-4: Drawing of the bronchial tree structure. Note that the branching pattern is not symmetrical *in vivo*. (Copyright ©1996 by Biological Sciences Textbooks, Inc. and S. Reynolds Gabrowski. Reprinted by permission of John Wiley & Sons., Inc., from Tortora and Reynolds-Grabowski (1996))

bronchi, called tertiary (segmental) bronchi. Each tertiary bronchus supplies one bronchopulmonary segment of the lungs and divides into bronchioles. Bronchioles, in turn, branch repeatedly and the smallest bronchioles branch into even smaller tubes called terminal bronchioles. The general branching pattern is dichotomous, but trifurcations may appear.

At 17 weeks gestation the bronchial divisions are almost completely established and the growing of primitive air spaces (unexpanded until birth) and capillary vessels begins. This process continues until term, by which time the pattern of airway branching is complete. Only slight remodelling of the smallest airway branches occurs after birth.

As the branching structure becomes more extensive in the bronchial tree, several structural changes in the epithelium may be noted. Incomplete rings of cartilage insure the primary branches a fair rigidity. They are gradually replaced by plates of cartilage that finally disappear in the distal bronchioles. As the amount of cartilage decreases, the amount of smooth muscle increases.

During breathing, the cross-section of the airways varies depending on the amount of cartilage in the airway walls. Where there is no cartilage, the compliance of the airways increases. The design of the airways is optimal for the purpose of conducting the air between the atmosphere and the gas-exchange apparatus, since changes in calibre (airway cross-section) and angles at branching points are such that resistance to airflow is minimised (see Section 2.5.2, p. 32). However those dimensions are not static since the airways are distensible: the wall compliance alters airway dimensions *in vivo*. As lung volume changes during the breathing cycle, airway length and diameter also change. Soong et al. (1979) suggested this change in proportion to the cube root of lung volume, which implies the distensibility of airways to be isotropic with respect to lung volume. More recent *in vivo* studies [Brown and Zerhouni (1998)], using CT imaging (see Section 2.5.3), demonstrate that airways do not expand in that simple radial tethering. Airway resistance decreases as airway diameter increases during inspiration. The effect of change in length is small by comparison to diameters. However because of relatively high air flow velocities normally present in the airways even during quiet breathing, such changes in airway dimensions will produce insignificantly small changes in velocity of less than 0.1 $cm.s^{-1}$. Airway compliance does assume importance whenever there is a flow limitation, as for example during forced expiration. However some evidence exists which indicates that large transmural forces are present at these

airways which, because they lack support by surrounding structures, can and often do collapse [Macklem et al. (1963)].

Contraction of smooth muscle in the walls of airways is the means by which airway calibre changes in response to a specific stimuli. This is probably the most important factor altering airway compliance and therefore calibre. During an asthma attack the smooth muscle of bronchioles contracts, reducing the diameter of the airways. Because there is no supporting cartilage, the muscle spasms can even close off the airways. Disorders causing obstruction of the airways decrease lung air volumes, FEV_1 and capacities. Among the symptoms that might indicate airflow obstruction are coughing, wheezing and dyspnea (painful or laboured breathing). With advancing age, the airways and tissues of the respiratory tract, including the alveoli, become less elastic and more rigid. The chest wall also becomes more rigid. As a result there is a decrease in the vital capacity and in blood level of oxygen and elderly people are more susceptible to pneumonia, emphysema, bronchitis and other pulmonary disorders.

Particles which were deposited on the wall of the conducting airways are carried by the layer of mucus covering the surface of the airways which is slowly propelled by ciliary action to the pharynx. Here, the mucus is swallowed, sneezed away or spat out in a matter of hours.

2.5.2 Morphology And Topology Of The Conducting Airways

Data on human lung morphometry (diameter, length, branching angles and angles of inclination to gravity) are derived from measurements of a few human lung casts. Several authors have measured branches of the lung casts manually, which is a very time-consuming method. Weibel (1963) used resin and silicon rubber casts, Horsfield and Cumming (1968) used the resin cast of a 25 year old male, the Lovelace group [Raabe et al. (1976)] used silicon rubber casts of two males, 50 and 60 years old. Mortensen et al. in 1983 used 11 casts of children aged 0 to 21 years old [Menache and Graham (1997)]. Schlesinger and McFadden (1981) used wax casts of a 29-year old male and a 54-year old female to build a negative hollow cast.

Horsfield and Cumming's cast was made from excised lungs inflated to 5 litres. The other authors used lungs inflated *in situ*. The casting techniques were similar

to or adapted from Phalen et al. (1973) or Haefeli-Bleuer and Weibel (1988). The casts are representative of the end inspiratory state, i.e. about 3/4 of the total lung capacity (TLC). Disagreement on rubber casts being prone or not to deformation is pointed out in Thurlbeck and Horsfield (1980).

Number of conducting airways and identification system

The number of branches in the casts is estimated between approximately 30 000 and 60 000 in Menache and Graham (1997) but the number actually measured varies between authors.

The branches are always gathered by generation: the trachea is generation 1 in the Lovelace data and Mortensen's but is generation 0 for Weibel and Horsfield, the first branching point being then the carina. The branching pattern is almost always irregular dichotomous, which means that each branch divides into two branches not symmetrical in either size or space orientation.

Different systems of identification of the airways have been used. Weibel (1976) labels the airways with their generation number, subsequent generations being numbered distally (trachea identification number is 0). Thus airways of the same generation number have the same name. Mortensen et al. (1983) assigns each airway a unique identification number (ID) with the number of digits being its branching generation from the trachea (trachea ID is 1). The second digit "1" indicates the primary bronchus of the right lung, while a second digit "2" indicates the primary bronchus of the left lung. Thus any airway in the right lung would have 11 as its first two digits. All the subsequent digits in the ID for any airway are assigned according to that airway's general anatomic distribution ("0" indicates the airway constitutes a direct continuation of (rather than a branch from) the proximal parent airway, "1" indicates a branch which is distributed superiorly, "2" anteriorly, "3" medially, "4" laterally, "5" posteriorly and "6" anteriorly). The Lovelace group also assigns each airway with a unique identification number (trachea ID is 1) and implies a strictly dichotomous branching pattern. This number is formed by taking the ID number of the parent segment and then adding either a 1 to that number if the segment was the major daughter or a 2 to that number if the segment was the minor daughter segment [Phalen et al. (1978)]. Unlike the previous identification systems, Horsfield et al. (1971) published an ordering of the bronchial tree that numbers the branching order (also defined as "divisions up" in Horsfield and Cumming (1968)) from the periphery to the

trachea. The most distal branches comprise the first order, two of these meet to form a second-order branch, and so on. Where branches of different order meet, the order of the parent branch is one greater than the higher of the two daughter branches. Branches of the same order have therefore the same name and the trachea has the highest order (32 in their cast).

Diameters and lengths of the conductive airways

General observations of the casts showed that both the range and the average of diameters and lengths decrease with progressive generations of branching. Finer quantification is provided by the ratio of the diameters and the lengths of conjugate daughter branches. This is a measure of the degree of the branching. For the human lung, in generations 5 to 7 (trachea is in generation 0), the ratio of the smaller to larger diameter ranges from 0.5 to 1, averaging 0.86 [Weibel (1963)], value confirmed by Phalen et al. (1978), whereas the ratio of lengths averages 0.62 [Weibel (1963)]. This shows therefore that the irregularity of branching is due primarily to variation in the length but is also caused, to a lesser degree, by variations in diameter or cross-sectional area of conjugate branches. A further estimator is the ratio of length to diameter of airway segments, which is assumed constant in a regular tree. The length-to-diameter distribution may have a consistent pattern for most generations of conducting airways; Weibel (1963) found the average length-to-diameter ratio to be consistently around 3.25 for all diameter classes of airway from 1 to 4.5 mm; in Phalen et al. (1978), this ratio was slightly smaller (namely 2.8). The lengths in Yeh and Schum (1980) were estimated the same way but the diameters were found to be 20-30% higher than Weibel's measurements. The slight discrepancies between those authors were explained partly by the use of different casting material and partly by the standardisation of the data to the same lung capacity.

In order to model the bronchial tree, Weibel (1963) plotted the mean airway diameters, in the first ten generations of a resin cast, against generation number j and derived the following diameter-generation number relationship:

$$d_j = d_0 * 2^{\frac{-j}{3}}, \tag{2.2}$$

where d_j is the mean diameter of conductive airway generation j and d_0 is the diameter of the trachea. The equation was later explained by Wilson and Horsfield in 1967 by the theory of dichotomy: the minimal resistance for any bronchial

dichotomy is achieved for the ideal ratio

$$\frac{d_{j+1}}{d_j} = 0.79, \tag{2.3}$$

which is equivalent to equation 2.2. It shows that the diameters of the conductive airways are such that alveolar ventilation can be maintained with a minimum entropy production [Wilson (1969)]. Horsfield and Cumming (1967) based their mathematical demonstration on minimal volume occupancy compatible with air flow. They then measured branch diameters from a cast down to 0.7 mm and found the ratio d_{j+1}/d_j averaging 0.76, which concurs with the ideal value of 0.79. West et al. (1986) also explained this airway diameter and generation number relationship but with fractal analysis.

The total path from carina to distal respiratory bronchioles was estimated ranging from 7.7 to 22.4 cm, with a median value of 13.9 cm [Horsfield and Cumming (1968)]. This calculation was based on the path length from the carina to lobular branches ranging from 7.5 to 21.5 cm, with a median of 12.5 cm (Horsfield in 1968 arbitrarily defined the branches with a diameter less than 0.7 mm as lobular branches). The path length from the lobular airways to the distal respiratory bronchioles ranged from 2 to 9 mm.

Phalen et al. (1985) have also shown that the dimensions of airways depend on body length.

The volume in the conducting airways has been estimated using the anatomical data (Weibel, Horsfield and Cumming) and physiological methods (spirometry). The following volumes have been estimated: 80 ml for the upper respiratory system and larynx, 70 ml from the carina to the lobular branches and 43 ml from lobular bronchioles to terminal bronchioles (total 193 ml).

Branching and gravity angles

The branching angle has been found to be related to the diameter of the daughter. Indeed a very small branch will take off at almost a right angle from the parent, whereas the other daughter whose diameter remains large deviates only slightly from the direction of the parent: Phalen et al. (1978) observed that the minor daughter branches form an angle between 30° and 65°, the angle of the conjugate major branch being about 20° smaller.

The theory for dichotomy forecasts as well that for the minimal volume of the system the angles of branching are a function of the cross sectional areas of the branches, with an ideal figure of 37° 28' as calculated by Horsfield and Cumming (1967). The latter found from a cast study that the mean branching angles varied between 30° and 43°. The angle of branching and the ratio daughter-to-parent diameter increased distally.

The larger set of angle data is from the 60-year old male silicone rubber cast of Raabe et al. (1976). They were published, averaged per generation for the whole lung and per lobe, up to generation 12-15, in Yeh and Schum (1980). The mean branching angles per generation ranged from 18° to 51° (0° describes the alignment of a daughter branch with its parent direction). The individual values of gravity angle ranged from 0° (straight down) to 180° (straight up). However Yeh et al. (1979) converted gravity angles, γ, greater than 90° to (180-γ)°, before calculating their mean value at a given generation. This was because they were not concerned with the true spatial distribution of the airways, but rather with their fluid dynamic properties. The largest averaged gravity angle in the Right Upper Lobe is 68° in generation 7. In the Left Upper Lobe, it is 50° in generation 3. Naturally, this set cannot show the distribution of the airways in space.

Recently, Phillips and Kaye (1997) analysed the branching angles in this same airway data set, as a function of the area asymmetry for parent airways of 0.8 mm or more, rather than averaging over bifurcations with different degrees of asymmetry (as above). The area asymmetry was the square of the ratio of the major diameter daughter to the minor diameter daughter, which describes the asymmetry of the airways. They showed that the sum of daughter branching angles was dependent on the asymmetry of the bifurcation. This sum was also reduced as the parent diameter increased. In 18% of the bifurcations, the major daughter's branching angle was actually larger than that of the minor daughter.

Data to allow 3D studies, for instance looking at the planarity of bifurcations, were not available.

Intersubject variability

Very few studies on intersubject variability are available in the literature, mainly because of the difficulty of manual measurements. They may nevertheless be of value to help understanding both pulmonary physiology and pathology. In their

paper, Phillips and Kaye (1997) also commented: "it appears that there is only one human subject for which comprehensive data is in the public domain [Raabe et al. (1976)] ... we believe there is a pressing need for further measurements before it is clear how great the variations between subjects are, and to what extent the geometrical features identified are universal".

For use in dosimetry method, Menache and Graham (1997) studied the inter-subject variability as a function of age, measuring manually the branches in Mortensen's casts up to generation 10. They found the diameter distribution in generation 6 to 10 within each lobe to be well-described by a normal distribution. The branching structure appeared similar in these 11 casts despite numerous differences between subjects in conducting airway geometry. The branching patterns were generally similar but there was substantial variability in the branching angles and airway lengths. In general the airways branched dichotomously. However trifurcation at the generation 4 in the Right Upper lobe appeared in five of seven casts of children younger than 10 years old. The median value of length and diameter in generation 10 slightly decreased with age and an increase in variability was visible with age, but generally the distributions overlapped. The average ratio length/diameter equated to 2 in all generations and at all ages, this value being much lower than Weibel's but not explained. In general, subjects of similar ages had similar distributions but the spread of the distribution was shown greater with age. Expansion in the lower lobar airway diameters was observed and suggested associated with aging.

2.5.3 Imaging The Airways

In the past X-ray bronchography has been used to image the bronchial tree in two dimensions (2D). This was used for diagnosis of abnormalities. An intratracheal catheter was passed into the right or left bronchus through the mouth or the nose. Then an opaque contrast medium was inhaled, causing it to distribute throughout the bronchioles. Radiographs of the chest in various positions were taken, and the developed film, a bronchogram, provided a picture of the bronchial tree. Physiotherapy was needed to then remove the catheter (!). This technique was stopped two decades ago.

Nowadays, X-ray CT scanning at end inspiration allows some details on the bronchial tree to be obtained, however the imaging time is limited by the breathing (breath-hold required to avoid blurring) and the X-ray flux density is limited

by the dose delivered to the patient. Typically, the dose associated with a clinical chest high resolution CT scan is 8 to 10 mSv. What is of clinical relevance and what can be interpreted from this procedure are the appearances of 1) the large bronchi and vessels and 2) the secondary pulmonary lobule and its various components. In normal subjects, the large bronchi are distinguishable as their wall is outlined by lung on one side and air in the bronchial lumen on the other, appearing smooth and of uniform thickness. Some smaller bronchi can be noticed as they appear black, surrounded by the grey lung tissue. However bronchi closer than 2-3 cm to the pleural surface are not normally visible on CT [Webb et al. (1992)]. Bronchi smaller than the gap between two slices will not be seen, and decreasing the gap would mean more slices are required, thus a longer scanning time leading to a higher X-ray dose and a longer breath-hold.

High resolution CT imaging has been shown a successful diagnostic and investigational tool for the evaluation of airway hyper-responsiveness. Research studies on the airways are divided into two types: (1) anatomic descriptions of abnormalities of airways associated with asthma, and (2) physiologic correlations of airway calibre changes during bronchoconstriction and bronchodilation, in airways of diameter greater than 2 mm [Brown and Zerhouni (1998)]. It has also been used to simulate bronchus endoscopy [Mori et al. (1995)]. In these studies, the CT scan covers a maximum of 12 cm of the length of the lungs.

MR imaging, that images the proton (H^+) density, cannot be used to visualise the airways because, as they are filled with air, they do not contain enough protons to create a detectable signal. Like for CT imaging, it is the lack of signal that may allow the "visualisation" of some of them, i.e. their very black aspect surrounding by a grey lung tissue. However, it has recently been proposed to fill the airways via normal respiration with hyperpolarized noble gases, such as xenon-129 (Xe-129) or helium-3 (He-3), for MR imaging examinations of the lung because such gases open a new field of promising possibilities to enhance the signal. In these examinations, the source of the MR signal is the large nonequilibrium polarisation in the nuclei of the hyperpolarized noble gases. Xenon can be used in perfusion studies because it mixes with time in the blood stream, and helium in ventilation studies, because of its property of being insoluble. Nuclear spin polarisation is achieved by optical pumping techniques, reaching the order of the unit (whereas in a normal 1.5T magnetic field, the polarisation of protons is as small as 5.10^{-6}). The high spin density of the He-3 gas compensates for the otherwise very low

signal of He-3, which is caused by the low density of the gas. Subsequently, a high degree of polarisation is essential to allow detection of an adequate MR signal. Helium gas can be inhaled in considerable amounts and concentrations (80% helium, 20% oxygen) without risk. After hyperpolarized He-3 gas is inhaled, the airways and alveolar air spaces can be visualised with a strong intensity, as has been demonstrated in the guinea pig lung and in preliminary studies in humans [Johnson et al. (1998)]. Findings in these studies suggest that He-3 MR imaging can depict lung morphology and can help assessment of pulmonary ventilation. Just a few centres in the world have He-MRI facilities and only one (Mainz, Germany) does clinical studies. The imaging sequences recalled in literature [Kauczor et al. (1996)] used either 42 seconds breath-hold to get a 170 mm long scan of the chest with slice thickness of about 7 mm or 22 seconds breath-hold on patients and 10 mm slice thickness, both using a fast imaging sequence (FLASH). Gating the breathing movement and imaging for a longer time is not possible because the Brownian motion of the gas then blurs the images (personal communication Tastevin-Sauret). For the time being, HRCT seems then finer in its resolution. However it is of note that He-3 MR imaging is a new, promising imaging modality to help visualise and assess pulmonary ventilation. It will also help provide further insights into the pathophysiology of breathing and the slice thickness will go down more so the conductive airways will be visible with an appropriate resolution. Since only a few accessory tools are needed to perform He-3 MR imaging -with the exception of a dedicated coil- this technique could become widely available within a short time. Further developments such as improvements in sequences, use of smaller volumes of He-3, and recycling of He-3 are under way. At the moment the cost of non-polarised He-3 is about 100-150 US$ per litre and its availability is limited (product of tritium decay). Reviews of the technique, characteristics and potential of He-3 MR imaging are available in Kauczor (1998) and Kauczor et al. (1998).

2.6 The Pulmonary Acini

The pulmonary acini (singular: acinus) are defined as the complex of airways distal to the terminal bronchioles.

2.6.1 Anatomy Of The Pulmonary Acini

Figure 2-5 shows the structure of a pulmonary acinus. Terminal bronchioles subdivide into microscopic branches called first-order respiratory bronchioles (called also transitional bronchioles because they often contain an initial purely conducting segment). The volume of the respiratory bronchioles in the transitional zone is estimated to equal 865 ml. The respiratory bronchioles, in turn, subdivide into several (2-11) alveolar ducts. The transition from respiratory branches to alveolar ducts is gradual; Haefeli-Bleuer and Weibel (1988) estimated that respiratory bronchioles comprise about the first three generations of the human pulmonary acinus. The number of alveolated tubes connecting the last terminal bronchiole of the bronchial tree with an alveolar sac varied from 6 to 12, with an average of 9. Alveoli also appeared along the lower border of the terminal bronchiole in Boyden's acinus. Terminal sacs are developed in the period from the 26th week to term, when primitive alveoli are formed around alveolar sacs and at birth, alveoli are shallow and small and number less than 8% of those present in the adult. During the months after birth, rapid alveolar proliferation occurs but is not complete until approximately the 8th year. More than half of the adult complement of alveoli is developed by the end of the first year, after which alveoli proliferate at a much slower rate.

From the trachea to the alveolar ducts, there are about 25 orders of branching of the respiratory passageways. That is, the trachea divides into primary bronchi (first order), the primary bronchi divide into secondary bronchi (second order), and so on. Around the circumference of the alveolar ducts are numerous alveoli (singular: alveolus) and alveolar sacs. An alveolus is a cup-shaped outpouching supported by a thin elastic basement membrane. Alveolar sacs are two or more alveoli that share a common opening. Fine connections, called pores of Kohn, occur between alveoli of the same acinus or between neighbouring acini. Gas exchange occurs across the alveolar-capillary (respiratory) membranes. The distance from the terminal bronchiole to the most distal alveolus is a few millimetres. The branching structure from the terminal bronchioles is such that the total cross-sectional area of airways increases by a factor of 437 500 from the trachea (about

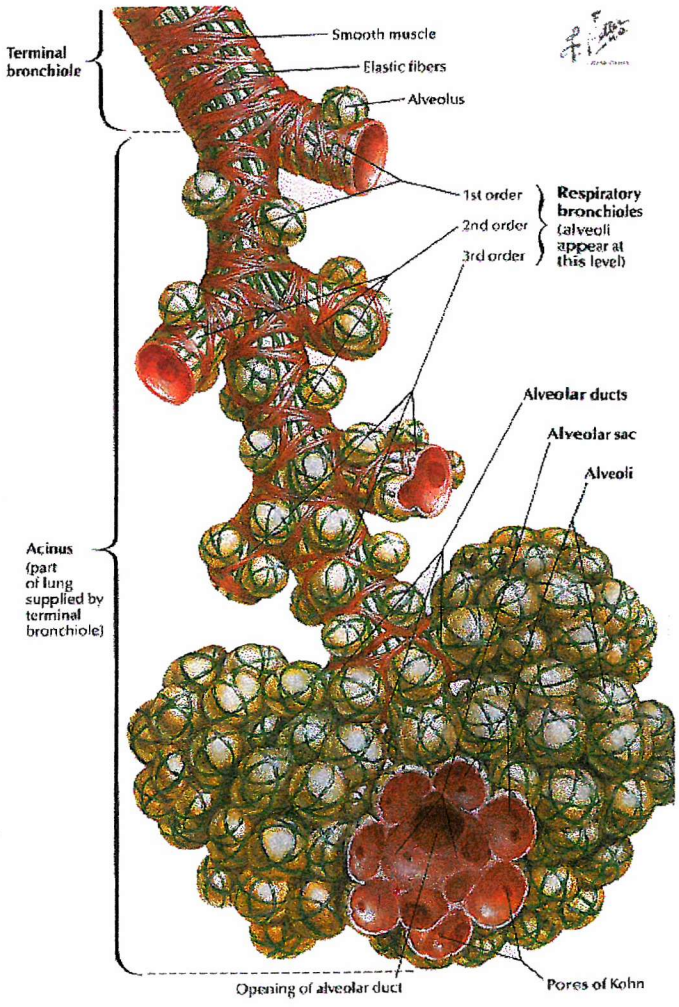

Figure 2-5: Drawing of the pulmonary acinus structure (Copyright ©1989 by Novartis. Reprinted with permission from Netter (1991), Plate 192. All rights reserved).

1.6 cm^2) down to the alveolar-capillary surface (700 000 cm^2). 96% of this increase occurs over the final 2.6 mm of the airways, within the respiratory zone. Compared to this enormous increase in total cross-sectional area, the average total length of the airway system is a mere 36 cm.

Alveolar walls consist of type I alveolar cells, type II alveolar cells, and alveolar macrophages. The acini do not have the protective mucous layer like the conducting airways because of its gas-exchange function. Insoluble particles deposited in the acini are cleared very slowly over a period of months. Soluble particles pass through the thin alveolar membrane into the blood stream.

2.6.2 Morphology And Geometry Of The Pulmonary Acini

There is no information in literature on the acinar region as detailed as in the conducting airways. The morphometric data in Haefeli-Bleuer and Weibel (1988), collected from the study of two silicone rubber casts from two adult lungs, are the most recent data describing the features of the geometry and dimensions of the intra-acinar airways in human lungs. The acini were inflated to nearly the total lung capacity and the detailed analysis of the morphology was done on a statistically representative sample. Extensive drawings of an acinus studied on a wax cast (about 20% shrinkage) of a 80 months old male child (6 years and 8 months), whose lung had attained about a third or more of the adult volume are provided in Boyden (1971).

Number of acini

The acinar volume averaged 187 mm^3 (SD $\pm$ 79 mm^3) (weight technique) with the shape of the volume distribution curve described as slightly skewed log-normal distribution. The number of alveoli forming these complexes was difficult to estimate because the demarcation of the single alveoli is not always obvious. The branching pattern to prevail in the acini was found irregular dichotomous. This was in agreement with the description of the human bronchial tree by Weibel (1963) and also with airway morphogenesis in the fetal lung, which occurs by dichotomy of the airway tubes. Assuming a total acinar volume at total lung capacity of about 5-6 litres and a mean acinar volume of 187 mm^3, Haefeli-Bleuer and Weibel (1988) estimated that the human lung should contain some 26 000-32 000 acini, whereas Boyden (1971) considered there are 80 000.

Shape and size of the acinar components

The acinus studied by Boyden (1971) measured 7.4 mm in diameter, but had a conical shape.

In Haefeli-Bleuer and Weibel (1988), the longitudinal path length of acinar airways averages 8.8 mm (Standard Deviation $\pm$ 1.4 mm). The difference between the outer and inner diameter of the airways reflected the mean depth of the alveolar sleeve, which increases towards the periphery. On a large sample of acini, the diameter of the transitional bronchiole (d_{tb}) was weakly, but significantly (correlation test: r=0.61, p$\leq$0.01), related to the air volume it supplied, i.e. the volume of the acinus V_{ac}:

$$d_{tb}(\mu m) = 389 + 0.54 * V_{ac}(mm^3). \tag{2.4}$$

Acinar airway diameters were shown not to follow the same decrease as the bronchial tree airway diameters (Eq. 2.2) but to decrease to a much lesser degree (the outer diameter remained practically constant). This was justified by the fact that the design of the conducting and respiratory airways follows different laws and abides by different constraints since mass flow of air is the governing physical principle in the conducting airways, whereas O_2 diffusion in the air phase along the acinar airways dominates the process of alveolar ventilation (i.e. the supply of O_2 to the gas-exchange surfaces). Transport energy must be minimised by reducing the airway diameter in the first case, whereas diffusion is favoured by keeping the airway cross-section large. The surface area of the gas-exchange membrane, generally agreed to equal about 80 m^2, is functionally important. The alveolar surface area S_a is about 160 m^2, varying with body size [Forrest (1979)].

Intersubject variability

Like previous authors [Forrest (1979), Boyden (1971)], Haefeli-Bleuer and Weibel (1988) found a great variability in the shape and the size of the pulmonary acini they studied. Boyden introduced also the concept of "fight for space" accompanying the growth of the lung and concluded his paper as follows: "One leaves [the] study with the feeling that so great is the fight for space in the post-natal years of growth and differentiation that the end-result is a highly variable and individualist pattern".

This shows that morphological and geometrical differences probably exist between different areas of the lung [Forrest (1979)] and also between individuals. However

information on how different they are is not available.

2.6.3 Imaging The Acini

High resolution CT imaging is not able to image the acini as the wall is not thick enough to appear on the CT images.

2.7 Modelling Of The Bronchial Tree And Pulmonary Acini

In attempting to describe the overall morphometric properties of the bronchial tree and the pulmonary acini, models have been derived from the previous morphometric data. Each model is based on a number of assumptions, stated to be aware of their limitations, by which it stresses certain aspects at the expense of others. Two general approaches have been taken: a descriptive approach and a stochastic one. The next chapter will show how conducting airways and acini modelling is used 1) in particle deposition assessment, and 2) in particle deposition modelling but that it could be more useful if more 3D realistic.

2.7.1 Descriptive Approach

The "model A" [Weibel (1963)], also called "typical path lung model" [Phalen et al. (1978), Yeh and Schum (1980)] is the simplest model. The airways are assumed to be a regular dichotomous branching system with 23 generations. The airway geometry is approximated by a sequence of straight cylindrical tubes that are 2^j branches starting at the trachea which is given generation number $j = 0$. Every airway of each generation has the same dimensions, thus creating a perfectly symmetric model. Only lengths and diameters are modelled with dimensions derived from averages of manual measurements of airway casts (see Section 2.5.2, p. 31). From the 17th generation, increasing number of alveoli are present on the surface of the airways and the last 3 generations are completely alveolated. Thus, the alveolar region in this model consists of all the airways in the last 7 generations. The drawbacks of the model A are its lack of asymmetry in the bronchial tree, that is seen in life and that it suggests that all gas-exchange units are found at equal distance from the carina. Also, it does not contain any information on the airways structure in the 3D space.

Because the model A is a relatively simple approach to a complex organ, other models have been derived from it. Among them are the Lovelace model [Yeh and Schum (1980)], the trumpet model [Taulbee and Yu (1975), Yu and Diu (1982), Egan and Nixon (1985), Hashish et al. (1988)], Martonen's model [Martonen et al. (1995)] and the shell-generation model [Fleming et al. (1995)].

Yeh and Schum (1980) used the same symmetric dichotomous idea as Weibel's (their diameter data were 20-30% higher than Weibel's, as cited above) but their airway model is presented for each lobe of the lungs. Airway lengths and diameters are represented by log-normal probability density functions and the model also includes, up to generation 15, a branching angle and an angle of inclination with gravity for each airway generation, calculated as the average values of all the branches of the same generation (see Section 2.5.2, p. 32). In higher generations the gravity angles are fixed at 60° (average of a 0°-90° range in 3D) and branching angle at 45° (average of a 0°-90° range in 2D). This was an attempt to describe the regional variations that exist within the lung, generally called intra-subject variability and also to give some 3D reality to their model. The average data of the airways are available for the whole lung and per lobe.

The trumpet model represents the variation of the cross-sectional area of all the airways in each generation against airway depth in the lung (i.e. length from the trachea), showing a massive increase in the total cross-section in the last millimetres of the lung resembling a trumpet shape. At the last portion of the trumpet, additional cross-sectional area is present to account for the alveolar volume per unit length of the airways. This model cannot differentiate the air volume in the right lung from the one in the left lung.

The conceptual shell-generation model is similar to the above models in the sense that it also describes the air volume in each airway with respect to their depth in the lung. However their spatial distribution in each lung is standardised to a hemisphere, via a hemispherical transform of each lung shape, whose concept is described in Perring et al. (1994). Briefly, it transforms the real lung shape into a series of ten concentric hemispherical shells. The basic assumptions of this 3D model of the airways are (1) that the conducting airways (defined as generations 1 to 14) can be considered as consisting of airway paths, each of which branches outwards from the centre of the lung around a radial path terminating in an acinus and (2) that the acini (defined as generations 15 to 23) fill the remaining volume uniformly [Fleming et al. (1995)]. The total volume of each airway generation in

each shell is still based on Weibel's lengths and diameters data. The model itself consists in an air volume two-dimensional (2D) matrix that represents the whole lung. Information in lobar and segmental air volumes cannot be extracted from this matrix. The model assumptions cannot be validated with the current data in literature.

Martonen's model is the first attempt, to our knowledge, to describe the airways truly in space and in a 3D volume image. The airway lengths and diameters are these of Weibel's, re-arranged by Soong et al. (1979); the branching angle is set to 35°, the mean branching angle value found by Horsfield and Cumming (1968), as reported above. The airways, starting with the vertical trachea, are regarded as a series of Y-shaped bifurcations units with an arbitrary angle of 90° for the relative orientation of the successive bifurcations. The resulting model has the two lungs symmetrical and overlapping, which is quite unrealistic. A new version of the model has been recently described [Martonen et al. (1999)], where constraints on airway branching were imposed forcing the airways to fit into a realistic lung shape. Again validation of the resulting model is difficult.

In the real lung, the airways are not symmetric and Weibel's model overestimates the number of airway structures and ignores the appearance of alveoli in the early airway generations. In order to bring models closer to the real lung, asymmetry in the branching pattern has been introduced [Horsfield et al. (1971), Weibel (1976)'s model B), where airways may branch into daughter tubes of different orders; however, tubes of the same order still have identical geometric parameters. Models of asymmetric airways were proposed by Horsfield et al. (1971) for the tracheobronchial tree and by Parker et al. (1971) for distal airways. An average complete asymmetric lung model compatible with both measurements was proposed by Olson et al. (1970). The bifurcation angles were set to 40°. Olson et al.'s model resembles the model of Weibel. Although the number of airways at high orders is considerably less, it is also overestimated.

Very recently, Kitaoka et al. (1999) and Suki et al. (1999) proposed a 3D volume image model of the airway tree down to terminal bronchioles using a deterministic algorithm based on two principles: (1) the amount of fluid delivery through a branch is proportional to the volume of the region it supplies, and (2) the terminal branches are arranged homogeneously within the organ. Initial conditions specifying the outer boundary of the organ and the configuration of the trunk have to be provided. Currently, the algorithm uses a combination of mathematical surface

expressions to mimic lung shape and the trunk is described following anatomical text books description. This asymmetrical model appears to be the closest to a realistic description in terms of number of terminal bronchioles and total airway volume created, although validation of the distribution in space of the airways and the lobar structures formed was not possible because of the lack of relevant information in the literature.

2.7.2 Stochastic Approach

The parameters defined in the above so-called deterministic models have been derived by averaging data on lung dimensions obtained from various casts. Thus each individual lung is described by the same anatomical structure. To model the inter-subject variability seen in life, stochastic approaches have been taken.

The first attempt to describe the geometry of the human tracheobronchial tree per generation in a statistical manner was made by Soong et al. (1979). They considered the Weibel geometry as the underlying average model and derived distributions of the actual data around these averages from published morphometric measurements. Airway lengths and diameters were represented by log-normal probability density functions, however, the unrealistic symmetric branching concept of Weibel was preserved. In 1982, this approach was extended to the acinar region and a probabilistic lung model was proposed in which inter-subject differences in airway dimensions are simulated by two random scaling factors for tracheobronchial and air volumes, respectively, assuming again the simplification that the Weibel model represents the population mean [Yu and Diu (1982)].

Koblinger and Hofmann (1985) described the asymmetry and randomness of the human tracheobronchial tree in their stochastic model, given the morphometric data available on the bronchial tree from the Lovelace ITRI files [Raabe et al. (1976)]. Averages and distributions of diameters and lengths of tubes in the different generations, ratio of parent tube cross-sections to the combined cross-sections of both daughters, ratio of the diameters of minor and major daughters, branching angles for minor and major daughters, were derived. In addition, correlations of diameters and lengths of tubes of the same generation, as well as the probability of reaching the acinar region as a function of both tube diameter and generation number (termination probability), were obtained from a systematic statistical analysis of those files. Information on gravity angles being very poor in literature (see Section 2.5.2, p. 32), a uniform distribution of the azimuth angle

over (0, 2π) and a downward preference were assumed. This stochastic model allowed for variations in diameters, lengths, branching and gravity angles and also in the number of bifurcations leading to the end of each bronchial pathway. At this stage each acinus closing the last terminal bronchiole was approximated by a single sphere [Koblinger and Hofmann (1990)], which diameter was calculated from Haefeli-Bleuer and Weibel (1988), Hansen et al. (1975) and Schreider and Raabe (1981). The model was constructed in the view of reflecting variations within a given individual airway system, i.e the model incorporates parameter variability (i.e. intra-subject variability) as well as asymmetric branching. Not enough information was available to derive distributions required for the consideration of inter-subject variations. It has recently been said (Hofmann-Fleming personal communication) that the resulting stochastic lung is too flat, problem due to the gravity angles selection.

Phillips et al. (1994) have developed an asymmetrical model based on the analysis of the Lovelace ITRI files, an approach similar to Koblinger and Hofmann (1985). They used a statistical reconstruction technique to restore the contributions of the missing airways in the ITRI files on the basis of the branching patterns observed in the parts that were measured by grouping the airways by their diameter, rather than according to their position in the tree, in term of generation. Their model allows the diameters of daughter airways to be determined, in a statistical sense, given the diameter of the parent. Similarly, the length of an airway has characteristic probability distribution that depends on its diameter. Predictions for the total number of airways of each diameter, for the distribution of bronchial surface area and volume between airways of different diameters and for the probability distribution of the lengths of different pathways through the bronchial tree are consequently presented. Diameter and length comparisons with Weibel (1963)'s symmetrical lung model showed qualitative differences, whereas generally good agreement was found with Horsfield and Cumming (1968)'s asymmetrical model.

2.8 Conclusion

Anatomical information available in text books on the respiratory system describes the general structure of the lungs, bronchial tree and pulmonary acini. But detailed studies from observations and manual measurements on lung casts show both inter- and intra-subject variability. Medical imaging, such as CT and MR imaging, offers, to a certain extent, an insight of the *in vivo* pulmonary anatomy

for each subject. However, detailed visualisation of the pulmonary anatomical features within the whole lung is limited. This is true in particular for the pulmonary segments and airway tree, although their definition in terms of size and spatial location is of clinical interest.

Segmental anatomical models (atlases) have therefore been developed: they represent a standard or average partitioning of the lungs. The task of modelling the complex airway branching network has initially been simplified to a basic symmetrical and dichotomous branching tree. Asymmetry and variability parameters have then been added. Efforts have been made in the more recent models to give an overall realistic shape to the lung, i.e. to locate the airways in the 3D space correctly, but the small amount of information available in the literature on branching and gravity angles has limited the validation of the resulting models.

The next chapter is concerned with aerosol deposition in the lungs and will show in particular, why improvement in the 3D realism of the current pulmonary anatomical models can be beneficial to research.

Chapter 3

Aerosol deposition in the lungs

3.1 Introduction

The work presented in this thesis is focused on the use of anatomical models to describe the pulmonary aerosol deposition. This chapter first relates the different particle deposition mechanisms that occur in the lungs. The current state of research in measuring the *in vivo* anatomical distribution of aerosol deposition and the existing computed prediction models are then examined. Particular emphasis is placed on the way some of the models of the pulmonary airway reviewed in the previous chapter have been used, despite their limitations. In conclusion, the areas of research on which the following chapters concentrate will be justified.

3.2 Deposition Mechanisms

Deposition refers to the initial processes that determine what fraction of the particles in the inspired air are caught in the lungs and fail to exit with the expired air. Distinct physical mechanisms operate on inspired particles to move them across streamlines of air and toward the surface of the respiratory tract: these are gravitational sedimentation, inertia, Brownian diffusion and electrostatic forces.

3.2.1 Deposition Mechanisms

Generally, gravity and inertia dominate the transport and deposition of particles larger than 1 μm in diameter, and diffusion dominates the transport and deposition of particles smaller than 0.1 μm. For particles between 0.1 and 1 μm, sedimentation and diffusion are both important. To understand each mechanism that makes particles deposit in the airways, a physical approach rather than a

purely mathematical one is given here, based on Brain and Blanchard (1993). The reader is referred, for example, to Yeh and Schum (1980) and Owen (1969) for the mathematic formulae needed for calculations in the lungs.

Gravitational Sedimentation

All particles with density greater than that of air experience a downward force due to gravity. The bigger the particles are and the longer they stay in the lung, the more likely they are to deposit. The probability that a particle deposits by gravitational settling, P_{set}, is related to the sedimentation parameter which is expressed as

$$P_{set} \propto d_{ae}^2 t, \tag{3.1}$$

where t is the residence time in the respiratory tract. The aerodynamic diameter d_{ae}, measured with a cascader impactor, is the diameter of the unit-density (1 g/cm^3) sphere that has the same gravitational settling velocity in air as the particle in question. It is useful to define it for different aerosol particles to be able to compare particles of unknown density or shape.

Sedimentation is important for particles larger than 0.1 μm within the terminal bronchioles and acini where flowrates are slow and residence times are long. Breath holding will enhance the residence time and, therefore, the deposition by sedimentation.

Inertial Impaction

Inertial impaction is the result of what occurs when an airstream carrying a particle at velocity u makes a sudden change in direction by an angle Θ as occurs at airway bifurcations. The value of Θ determines the new magnitude of the velocity that the particle suddenly attains, $u \sin \Theta$. The velocity vector is at right angles to the original particle velocity. Hence, the particle moves a total distance x proportional to $u \sin \Theta$ in the deflecting air streamlines before it loses its original momentum and again passively follows the airstream lines in the new direction. If the travelling distance x brings it in contact with a wall, the particle is assumed to deposit. This displacement increases with airstream velocity, angle of airstream deflection and the square of the particle diameter. The ratio of the stop distance to the radius r of the tube upstream of the bend (Stokes number) relates to the probability of deposition by impaction. The larger this ratio, the less the particles can follow the airstream lines around the bend and the more likely they are to impact.

Inertial impaction is an important deposition mechanism for particles with a d_{ae} larger than 2 μm and may occur both during inspiration and during expiration in the upper respiratory system, the larynx and at central airway bifurcations. Therefore the knowledge of the angle of branching of each conducting airway bifurcation is essential to assess this deposition probability correctly.

Brownian Diffusion

The constant random collisions of gas molecules with small aerosol particles push the particles about in an irregular fashion called Brownian movement. Thus even in the absence of gravity, a particle in still air moves about in a "random walk". This is a stochastic process that allows motion in 3D. The smaller the particle, the more vigorous its movement and the longer it stays in the lungs, the more likely it is to be deposited. In both cases, the Brownian diffusion coefficient describing the particle is high. Diffusion is important for particles with diameters less than 1 μm whose size approaches the mean free path of gas molecules. The probability that a particle is deposited by diffusion, P_{dif}, is related to the diffusional parameter which is expressed as

$$P_{dif} \propto (t/d_{ae})^{\frac{1}{2}}. \tag{3.2}$$

In the lungs, diffusion, like sedimentation, is important in the peripheral airways and acini. Decreasing particle size or increasing residence time in the lungs increases the chance of diffusional deposition. As particle size decreases, inertial impaction and sedimentation become less important, but diffusion increases in importance.

Electrostatic Forces

Electrical forces may cause particles to deposit in the respiratory tract. The surfaces of the respiratory tract are uncharged but are electrically conducting. When an electrically charged particle approaches the airway wall, the particle induces an image charge of opposite polarity on the wall surface which attracts the particle. The more charged the particle, the higher the image force. The attraction force is proportional to the square of the ratio charge to mass of the particle and to the inverse of the square of the distance of the particle to the wall. This attraction may cause the particle to deposit. The particle probability to deposit is also related to its charge. Melandri et al. established that the probability

of electrostatic deposition, P_{elec}, is

$$P_{elec} \propto \left(\frac{(ne)^2}{d}\right)^{\frac{1}{3}}, \tag{3.3}$$

with ne the total electrical charge on the particle (number of elementary units of charge times the elementary charge e) and d the particle diameter.

Naturally occurring aerosols tend to be at a low level of charge. However, if the particles are charged deliberately, not to the maximum level of charging, but higher than this natural level, experimental studies [Melandri et al. (1983), Chan et al. (1978)] show that the electrostatic attraction may be an important deposition mechanism in the lung. The deposition occurs mainly in the alveoli, where the particles are close enough to the airway wall, for particles (especially fibres) that are both charged above a certain threshold and have a diameter of 0.1-5.0 μm. Theoretical studies [Hashish and Bailey (1991a), Hashish and Bailey (1991b), Hashish et al. (1993)] have also shown that it could be a control factor to ensure deposition in desired regions of the airway tree.

Interception And Other Forces

Deposition can also occur when the particles have dimensions that approach those of the airways. As particles move into smaller and smaller airways, some may reach a point where the distance to a surface from the centre of a particle is less than the particle size. The resulting contact is called interception.

Other forces acting to promote deposition, such as magnetic, acoustic, thermal and radiational, are normally not significant in the lung.

3.2.2 Effects Of The Lung Anatomy On The Aerosol Deposition

The mechanisms that contribute to the deposition of a specific particle depend on the aerodynamic characteristics of the particle, the subject's breathing pattern, the geometry of the respiratory tract, and hence, the flow and mixing pattern of the aerosol within the respiratory tract. The configuration of the lungs and airways is important since the efficiency of deposition depends in part on the diameters of the airways, their angles of branching, and the average distances of particles to lung surfaces in the alveoli. Along with the volumetric flow rate, airway anatomy

specifies the local linear velocity of the airstream and thus determines whether the flow is laminar or turbulent. In this section we concentrate on some of the observations made in the literature on the importance of the geometry of the lung anatomy.

Studies of aerosol behaviour in hollow casts of the upper airways or in bifurcating tubes where the local distribution of deposition can be measured most precisely, show the effects presented above. A localised area of high deposition was found at bifurcations along the carinal ridge, which is caused by impaction. In the deeper lung, sedimentation caused particles to deposit only on the bottom half of lung surfaces, while diffusion deposited particles on all surfaces. In addition, there may be enhanced particle deposition on the parent airway wall directly opposite the opening for the daughter airways [Martonen (1983), Martonen (Southampton General Hospital seminar, June 1999)].

Gender differences in laryngeal and airway geometries may cause women to have greater upper airway deposition by impaction compared to men [Pritchard et al. (1986)]. Among normal individuals breathing in the same manner, total deposition fraction has a coefficient of variation as large as 27%. This is largely due to intersubject differences in airway geometry [Yu and Diu (1982), Blanchard et al. (1991)]. Within the same individual, the dimensions of the respiratory tract change with lung volume, age and pathologic processes. The way it affects aerosol deposition has been examined by several authors. Among these studies, Agnew (1984) showed that, within a person, decreasing lung volume increases deposition fraction and also causes the major site of particle deposition within the airways to shift from the lung periphery to more central airways. At low lung volumes, airways have smaller cross-sectional areas, higher linear velocities, and thus enhanced deposition by impaction in central airways for a given flow rate.

3.3 Measurement Of Particle Retention

The actual amount of aerosol found in the lungs at any time is called the retention. It is determined by deposition and clearance. As the particles deposit in the airways, the defence system (mucociliary clearance and alveolar macrophages) acts to move them away. The chemical composition of the aerosolised drug can also vary with time. Therefore it is important to note that clearance and translocation occur as well as redistribution of the deposited dose, this latter being due to

bronchial circulation, and may thus be a problem for retention assessment.

Once the particles have been introduced in the respiratory tract, the amount and distribution of dose are to be quantified. The measurement techniques vary in expense, resolution, the extent to which the subject must be disturbed and the interest that the results will have in clinical practice. Relative aerosol deposition in the lobes and segments, in airway generations and in specific airways are information of major concern in aerosol therapy, as they specify the deposition site in relation to the subject's anatomy itself. Furthermore, it is necessary to know more about the distribution and metabolism of the drugs given, in particular to be able to relate deposition site to clinical effect or to target drugs to a specific area. This section reviews the existing non-invasive and non-destructive (!) methods of quantification of aerosol deposition in the human lungs. Methods using non radioactive material are the simplest and are limited to measurement of the total pulmonary aerosol deposition. The use of radio-labelled aerosol allows total and, to a certain extent, regional deposition to be measured. Non-radioactive methods are described first, followed by the radioactive methods.

3.3.1 Non Radioactive Methods

The first approach to estimate the drug deposition in the lungs is based on measurements of the percentages of drug dose recovered in mouth-washings, from the exhaled air and from the inhalation apparatus.

Some aerosol particles are magnetisable and sensitive magnetopneumography can be used to measure their concentration and distribution in the lungs. This technique consists of applying a magnetic field to the whole thorax or to localised areas and detecting the resultant alignment of ferromagnetic domains in retained lung particles. Accumulations of magnetic particles have been measured in foundry workers, arc welders, coal miners and asbestos miners. The greatest advantage of this technique is that the duration of measurement is not limited by radioactive decay (see below the use of radioactivity to measure aerosol deposition). Measurements can be made as long as sufficient dust remains in the lungs. Thus, one can describe clearance kinetics over years. Two magnetic dusts suitable to study retention of dust in the lung are Fe_3O_4 (magnetite) and γ-Fe_2O_3 (a magnetic form of hematite). Both are inert, relatively insoluble at physiological pH and can be aerosolised. The magnitude of the remnant field quantifies the amount of dust remaining in the lungs.

The information obtained with these methods is limited to the total pulmonary retention of inhaled particles. To our knowledge the use of hyperpolarized gas for labelling particles has not been suggested. If possible, this would be a non-radioactive imaging technique to view aerosol deposition in the airways in 3D (see Section 2.5.3, p. 35).

3.3.2 Methods Involving Measurements Of Radioactivity

Because of its potential for non-invasive measurement and its sensitivity and resolution, radioactivity can be used for tracking the fate of particles in the body. First, this requires the radiolabelling of the particles: the radiolabelling of the drug is obtained by coating or chemically linking the particles with a radionuclide. For aerosol studies, the drug is radiolabelled before inhalation. Once inhaled, the radiolabelled aerosol is traced by recording the radioactivity in the lungs, based on the hypothesis that aerosol particle and radiolabel will not dissociate during the time of the study. The radiolabel is usually a gamma-emitter with a short decay half-life to minimise retention of radioactivity (see Glossary, Effective Radiation Dose), but long enough to conduct the study. Gamma emitters penetrate through tissue and are therefore suitable for making measurements externally. The ideal radionuclide for radioactivity imaging should have an energy between 80 and 200 keV (if exceeded, problems with shielding and collimator design increase). Deposition of the drug in regions of interest can then be monitored using probes or a gamma camera. Descriptions of the technology involved are summarised in several books such as Webb (1988). In brief, these devices are sensitive to the gamma rays emitted at the radioactive disintegrations produced in the radiolabel nucleus. They output a number or an image representative of the activity in the area it is covering. Probes are usually located on the back of the patient and each covers a small area. They may be used to obtain estimates of the whole lung deposition using suitably positioned combination of several detectors [Stahlhofen et al. (1980)]. The images cover the whole lung.

Gamma-cameras utilise a stationary radioactivity detector, which simultaneously collects information from a large area. This device uses a single, large scintillation crystal. It is masked with a honeycomb parallel-hole lead collimator with as many as 15 000 holes: each part of the crystal therefore looks at only a small area of the patient, lying down. An array of phototubes senses the light pulses (scintillations) produced in the crystal by incoming gamma-rays and the relative pulse sizes from

different photomultiplier tubes give the position of the scintillation. From this, the 2D position of the labelled particle in the respiratory tract can be estimated and displayed (counts per pixel) on a cathode-ray tube screen or stored in a computer (planar image, scintigraphy). The digital images can then be used to obtain quantitative information on aerosol deposition within the body. The number of gamma rays reaching the camera is reduced by tissue attenuation and quantitative measurements require correction for this effect.

Tomography is used to image the distribution of retained radiolabelled particles in 3D. Such images can be obtained with two types of tomography: single-photon emission computed tomography (SPECT) and positron emission tomography (PET). In SPECT imaging, the aerosol is also labelled with a gamma-emitting radionuclide particles. After inhalation of the aerosol, the patient lies in supine position on the gamma-camera bed. 64 successive planar acquisitions are performed, the camera rotated a few degrees between each. At the end of the process the camera has completed a full circle around the patient (360°). From those 64 acquisitions, a 3D volume image is reconstructed using a computer program. Quantitative measurements of the aerosol distribution require correction for gamma-ray attenuation through tissue. The 3D attenuation map, that contains the density of the various imaged tissue and provided by a thoracic CT or T1-weighted MR scan (see Section 2.4.1, p. 21 and 23), is included in the reconstruction process [Fleming (1989), Fleming et al. (1996b)]. A transmission scan can also be done: the absorption by the body of a line source is imaged with a rotating γ-camera. This gives low resolution 3D outlines [Chan et al. (1999)].

Most planar and SPECT imaging is performed with the radionuclide ^{99m}Tc (Technetium) which is a pure gamma-emitting nuclide with almost optimal energy (140 keV) and half-life (6 hours). Successful planar imaging (one posterior image and one anterior generally) can be carried out with a delivered activity of ^{99m}Tc to the lungs of approximately 3 MBq and an acquisition time of about 60 seconds. But the inherent disadvantage of these planar images is that they represent only a 2D distribution of radioaerosol. Particles in the central airways and peripheral lung regions can be resolved better in the 3D view given by SPECT imaging [Perring et al. (1994)]. The main drawback of the latter technique is that it requires levels of radioactivity approximately 10 times higher than planar imaging. Imaging ideally requires about 15 minutes to complete all the scans, when using a dual-head tomographic camera (total rotation of each camera around the patient is thus

180°), risking movement of activity via mucociliary clearance. In addition, current radiolabelling of drugs with ^{99m}Tc often coats the particles with the label rather than chemically attaching it to the drug. This means that in this imaging time, the activity may also dissociate from the drug and appear in the blood stream, making the interpretation of the images more difficult. Imaging time of as low as one minute have been used with triple-head camera using 80 MBq [Chan et al. (1999)] (the Becquerel, Bq, is the SI unit for radioactivity).

The use of Positron Emission Tomography (PET) in lung deposition studies is very recent. The positrons emitted by radioactive decay quickly combine with an electron to produce two gamma photons emitted at 180° to each other, which are used for imaging. In this technique, the drug of interest can be labelled directly. Thus, it has the potential to provide kinetic information on the fate of the drug [Lee et al. (1999b)].

2D Assessment

Definition of the area covered by one or more probes with respect to the patient's anatomy is very difficult to estimate, whereas definition of the area covered by the lungs in a planar aerosol deposition image can be obtained with a planar ventilation study with the patient staying in the same position on the gamma camera bed. ^{81m}Kr (Krypton) inert gas is inhaled by the patient while planar imaging is performed. Because of its very short half-life (13 seconds), this gas gives a good 2D definition of the lung margins in normally ventilated subjects. The percentage of the inhaled dose deposited in the lungs can thus be estimated from the attenuation corrected counts in the lung region. This assessment technique of the total aerosol deposition in the lungs is however limited to normally ventilated subjects as cold spots, which are areas of no record of activity, would show a poorly ventilated area and may bias the lung outline shape.

Total pulmonary deposition of radiolabelled aerosol, investigated with planar imaging, can be detailed further by dividing the outlines of the lungs into two "regions of interest" (ROI), one central zone usually drawn to include the major bronchi, while a peripheral zone mainly comprises small airways and alveoli. A penetration index that represents the relative deposition in these two areas can then be calculated (e.g. Newman et al. (1991)). It brings information on the gross distribution in the central airways and at the periphery. It is a measure of the extent to which the aerosol has penetrated along the airways to the most peripheral zones. It is

also called the "central to periphery ratio" or the "central to periphery index".

This planar regional deposition assessment technique has received criticism [Phipps et al. (1989), Perring et al. (1994)] because the central lung region, which is taken to represent the central airways, also contains overlapping small airways and acini. Thus one cannot discriminate among particle deposition in these regions, and deposition fraction in central airways may be overestimated. The same criticism occurred when the amount of aerosol located in apical or basal regions was assessed by suitable choice of regions of interest. Definition of these anatomical areas was also arbitrary. Assessment of lobar or segmental deposition is not possible using this technique as the upper and lower (and middle in the right lung) lobes overlap considerably.

An "asymmetry deposition index" was developed by Baskin et al. (1990) using planar aerosol deposition image and equilibrium xenon ventilation study; the latter was used to define lung lung margins and also air volumes (instead of Krypton above). The first image was divided by the second with a pixel-by-pixel analysis. Thus, the resulted image, labelled deposition-xenon (D/X) scan, represented aerosol deposition normalised for lung volumes, a representation of aerosol deposition if overall lung thickness remained constant. This scan thus provided a more accurate image of regional aerosol distribution than the original aerosol deposition image. The frequency of D/X pixel counts was plotted against the absolute D/X counts (histogram). The asymmetry index was defined as the interquartile range of the histogram, thus quantifying the distribution of the aerosol (statistical method to analyse frequency distribution-dispersion). The higher this index, the more asymmetric the aerosol distribution. The lower the index, the more homogeneous the aerosol deposition. The index however estimates the uniformity of the whole lung and not in regions. Visual examination of the scan is necessary to determine the type of non-uniformity, such as a deposition gradient in a particular direction.

Lastly, if insoluble particles are inhaled it can be assumed that those particles depositing on the ciliated conducting airways will be cleared by mucociliary clearance within 24 hours. It would therefore follow that those particles retained after 24 hours had deposited in the alveolar region. Such measures of 24-hour particle retention have been used by many authors using radiolabelled aerosol and planar imaging [Agnew (1991), Garrard et al. (1987)]. This methodology does provide information on regional deposition and clearance within the lung but is limited by

the assumption that mucociliary clearance is complete within 24 hours. However there has been an increased acceptance that clearance takes longer than 24 hours particularly in those with airway obstruction [Agnew (1991)], thus weakening the value of this measurement.

3D Deposition Assessment

Phipps et al. (1989) were the first to extend the penetration index measurement to 3D. This was a volumetric penetration index using 3D central and peripheral regions. It was compared with the penetration index from traditional planar imaging. This study confirmed the expected superior sensitivity of SPECT in differentiating between the deposition pattern of different inhaled aerosols.

The first attempts of assessment of deposition per generation have been made by Fleming and co-workers. They showed that the use of SPECT and of CT images of 3D outlines of the lung enabled improved quantitative accuracy [Perring et al. (1994)]. Landmarks on the nipples and on the sternum notch were used to align the two-modality images. The information provided on the spatial aerosol distribution required the SPECT data to be transformed into a hemispherical lung. The morphological conceptual shell-generation model (see Section 2.7.1, p. 42) was then overlaid to it and the amount of activity in each shell was calculated. This information was then converted into deposition in terms of activity per generation [Fleming et al. (1995)]. To reduce the dose to the patients, the same process was applied but using T1-weighted MR images of the outlines of the lungs instead of the CT. This ability to transform data on spatial distribution of aerosol in the lung to deposition by airway generation is potentially of value in providing more clinically relevant information. However this process developed in Fleming et al. (1995) and Fleming et al. (1996a) is based on a simple unrealistic morphological model of the lung and involves a number of non-validated assumptions. Also validation of the results of this analysis is not easy since no experimental studies on humans have generated the "true value" of the aerosol deposition in each generation. Simulation work is on going to validate this 3D deposition assessment method [Fleming et al. (1997), Fleming et al. (2000b)].

To date, assessment of lobar or segmental aerosol deposition using 3D atlases (see Section 2.4, p. 19) has not been published (see Section 7.2.4, p. 146).

To our knowledge, inhalation studies using PET have only been carried in London

(Hammersmith hospital), Cleveland and in Hamilton. The image interpretation uses an adaptation of the shell-generation model, and / or drawn regions of interest [Berridge et al. (1999), Lee et al. (1999a), Lee et al. (1999b), Dolovich et al. (2000)].

3.3.3 Summary

Experimental determination of particle deposition in the lung has been performed by many workers over the years. A large portion of these studies has initially been devoted to total deposition but investigations of regional lung deposition have taken off. This is mainly using radionuclide imaging, despite the facts that (1) their interpretation is difficult, and (2) the current methods of analysing the data relative to the lung anatomy, use anatomical models that have limitations and / or have not been validated. Moreover, they do not take into account the anatomical variability observed in the literature. To obtain the distribution of inhaled drugs throughout the respiratory tract, which is clinically important, the use of 3D multi-modality imaging seems the most promising. At present only the spatial variation of deposition within the lung outlines has been described, whereas to assess the clinical effect of the drug it is necessary to know in which anatomical part of the lungs, such as lobe, segment or specific airways, the deposition occurs. Regional differences also need to be identified and quantified. In order to derive such information the development of a model of the 3D morphology and topology of the airways, close to reality is required, in a form suitable to be superimposed on a SPECT or PET study. This will need identification in 3D space of the air volume location.

3.4 Predicting Aerosol Deposition In The Lungs

Theoretical model studies of lung deposition have also been conducted by many workers. The main interest in predicting aerosol deposition is to be able to vary different parameters without *in vivo* experiments. If ventilation is measured well, one can theoretically estimate deposition fraction based on predictions and models. The major aim of aerosol deposition modelling is to be able to predict the way particles are collected in the lungs, in order to facilitate deposition site targeting and also reduce *in vivo* experiments for clinical research.

3.4.1 Prediction Models

Theoretical Models

There are three major elements involved in the theoretical approach to particle deposition. First, a model of airways simulating the real structure must be specified. Secondly, deposition efficiency in each airway due to various mechanisms (see Section 3.2.1) must be derived. Finally, a computational procedure must be developed to account for the transport and deposition of the particles in the airways.

The first theoretical study of particle deposition in the lung airways was made by Findeisen in 1935 [Morrow and Yu (1993)]. Starting with the trachea, he subdivided the airways into 9 sections based upon a functional concept. The last section contained 5.2 x 10^7 alveolar sacs. He then considered each section to be an individual compartment and derived expressions for particle deposition efficiency from particle mechanics in this compartment. Particles which did not deposit in one compartment remained airborne and were transported to the next compartment. The amount of deposition in the ith compartment at inspiration is due to the volume of airborne particles passing that compartment and the volume of airborne particles residing in that compartment. During expiration, the amount of particle deposited in the ith compartment is due to the volume of airborne particles in that compartment and the volume of airborne particles on its way out. The total deposition in the ith compartment over a respiratory cycle with no respiratory pause is therefore the sum of the deposition during inspiration and expiration.

Yu, Taulbee and Diu [Taulbee and Yu (1975), Yu and Diu (1982)] have developed a model of aerosol deposition that takes into account the particle deposition mechanisms and incorporates the anatomical lung model of Weibel in the shape of the trumpet model (see Section 2.7.1, p. 42). They studied the effect of individual variability on aerosol deposition by comparing different deterministic lung models and attributing the predicted range of deposition fractions to differences in linear airway dimensions. The respiratory cycle consisted of constant airflow at inspiration and expiration, with no respiratory pause. The model has the flexibility to adjust different breathing pattern and to predict regional deposition, in terms of tracheo-bronchial and acinar depositions but the analysis of deposition is only applicable to small deposition efficiencies. Therefore Hashish et al. (1988) at Southampton University developed a lung deposition model based on Yu's theory

but allowing deposition efficiencies as high as unity. A respiratory pause in the breathing pattern and the effect of charged particles were new features added and the deposition predictions are given per generation.

Aerosol deposition predictions in each generation are also obtained with Yeh and Schum (1980), Gerrity et al. (1979), Hofmann and Koblinger (1990). These three groups have based their calculations on Findeisen's model (reviewed by Landahl (1950)). The anatomical model used in the study by Yeh and Schum (1980) also contains average airway dimensions for each lobe (see Section 2.7.1, p. 42), thus allowing for lobar deposition to be calculated for various particle diameters and given breathing pattern and air volumes. The anatomical model used in Gerrity et al. (1979) is Weibel's model A with branching angles fixed at 45° for all generations. A year later, they swapped it to Horsfield's asymmetric model of the airways that divides the lung into its five lobes. Hansen et al. (1975) was used to model the acini. Flow was distributed unevenly among the lobes by assigning a 1.10 base-to-apex ventilation gradient to allow for different pressure falls between mouth and alveoli in each lobe [Gerrity et al. (1981)]. The prediction model in Hofmann and Koblinger (1990) differs from the previous ones in that the effect of intra-subject variability on particle deposition in the lung is modelled by using their stochastic lung model (see Section 2.7.2, p. 44). Thus the geometry of the airways along the path of an inhaled particle is selected randomly, whereas deposition probabilities are computed by deterministic formulae.

Other prediction models exist in different research groups for specific applications. For instance the work by Finlay and Stapleton (1995) and Lange and Finlay (2000) is concerned with simulation of transport and deposition of hygroscopic aerosol particles in the human respiratory tract. The anatomical model used is asymmetrical, based on tracheobronchial length and diameter data in Phillips et al. (1994) (see Section 2.7.2, p. 45) and alveolar data from Haefeli-Bleuer and Weibel (1988).

Semi-Empirical Models

The ICRP prediction model, first published by the International Commission on Radiological Protection Task Group on Lung Dynamics (1966), is a semi-empirical model that was developed to calculate irradiation dose from airborne particles. It does not use the dimensions of the airways. Instead, it uses a compartmental model where the different parts of the lungs are considered as a series of filters; the de-

position analysis is based on Findeisen's model, with additional considerations for nasal deposition. The model includes both theoretical predictions and experimental data. It is in the form of convenient equations and computer programs so that total integrated exposure to particles can be calculated when particle solubility, size and concentration are known. It allows for scaling so that deposition and clearance estimates can be made for most people; that is, it will account for age, race, breathing level and the presence or absence of lung disease. It predicts the total and regional, in terms of tracheobronchial and acinar depositions, deposition fraction of particles in persons of different ages and in adults at different activity levels and breathing oronasally.

An improved ICRP model was proposed in 1994 [International Commission on Radiological Protection Task Group (1994)] based on the reviews of Rudolf et al. (1986) and Stahlhofen et al. (1989). The resulting model relies on experimental data of regional deposition for a wide range of particle sizes and breathing conditions. Reference values for particle transport processes as well as rates for absorption into blood were added to the previous irradiation dose calculations. The aerosol deposition is estimated in (1) the nasopharynx, or extrathoracic, region, (2) the tracheobronchial, or BB and bb, region and (3) the pulmonary, or Al, region, as defined in Figure 2-1.

3.4.2 Prediction Models Comparison And Validation

Summarising intercomparison of the predictions made by the algorithms described above is a complex task as particle sizes, anatomical models, expressions used for deposition efficiency, breathing patterns and air volumes are rarely the same. In general, there is agreement in total lung deposition. The larger differences between models occur mainly in regional predictions in the tracheobronchial and acini regions. Calculations of deposition at airway generation level using various lung models also show very different patterns for particles in the impaction range and not so different in the sedimentation range (e.g. Camner et al. (1997)). A vertical gradient appears in lobar depositions per unit volume in both Yeh and Schum (1980) and Gerrity et al. (1981), although it is predicted in opposite direction (increasing from base to apex and from apex to base respectively).

Comparison with experimental data, when available, has been done. Evaluations of particle deposition in the respiratory tract from inhalation experiments and model calculations with monodisperse aerosols have shown significant inter-

subject as well as intra-subject variabilities of total deposition (e.g. review from Stahlhofen et al. (1989) and Yu and Diu (1982)). Palmes and Lippmann and Giacomelli-Maltoni et al. cited in Brain and Valberg (1979) have also pointed out that intersubject variability can decrease the accuracy of predictive models to ± 40%. It was also shown that airway size is the most important factor in the consideration of intersubject variability of total and tracheo-bronchial/acinar regional deposition under normal steady breathing conditions [Yu and Diu (1982)]. However it is to note that not all the potentially influencing geometrical parameters could be studied in their 2D lung representation. Further studies examining the effect on the location of the aerosol deposition depending on the breathing position (e.g. lying down, on the side) that may be clinically valuable to target specific sites in the lungs are not possible, neither are studies on the orientation of the airways in space and variations in branching angles, that both vary between subjects and maybe within a subject, naturally or with pathology.

Recently, aerosol deposition studies using SPECT imaging have been investigated to validate aerosol deposition prediction models. The first comparison appeared in Fleming et al. (1995). Three of such studies are summarised below to show both the potential of these theoretical and experimental comparisons and the problems researchers encountered due to unrealistic anatomical models.

Hofmann et al. (1997) have attempted to validate their predictions per generation by comparison with experimental data from SPECT imaging, using the methodology of Fleming et al. (1995) to convert the measured SPECT spatial distribution of activity to deposition fractions in hemispherical shells and single airway generations (see Sections 3.3.2, p. 57 and 2.7.1, p. 42). Averaged breathing parameters through a nebuliser recorded during the SPECT image acquisition, the size of the particles inhaled (fine and coarse aerosols) and anatomical information from MRI images, namely the dimensions of the two lungs, their distance from each other and the lengths and branching angles of the main bronchi leading to the two lungs, were entered in the prediction model. The FRC of the stochastic lung model was adjusted to match the subject's FRC, estimated by spirometry (Fig. 2-2). The comparison between the SPECT assessment and the stochastic modelling predictions was based on total deposition, deposition per shell and deposition per generation. One subject was involved in this study. Agreement was found in total deposition of the coarse aerosol. Regarding the fine aerosol, the particle size range (0.5-1.93 μm) was to wide to allow reliable deposition calculations [Hofmann and

Koblinger (1990)]. The relative shapes of the deposition patterns per shell and per generation have similarities in both approaches, but there are some notable differences regarding the absolute values. The authors conclude on three points: 1) considering the potential effect of inter-subject variability in lung structure and the systematic differences in the two methodologies, the existence of discrepancies is not surprising, 2) the results presented are promising and warrant the further refinement of the computer model, and 3) SPECT imaging provides valuable experimental information about the distribution of particles which are badly needed for model validation purposes.

Hashish's model predictions were also compared with experimental data from SPECT imaging converted to deposition per generations as above [Hashish et al. (1998)]. Results show reasonable agreement for total lung deposition and for the difference in deposition pattern per generation between the fine and coarse aerosols. However experiment suggests significantly less deposition in the central generations than is predicted by modelling.

It is important to emphasise that in these two predictions vs. SPECT measurements comparison studies, three distinct airway morphologies have been mixed (all fitted to the patient's FRC): the shell-generation model airway morphology, the prediction model airway morphology and the patient's airway morphology. The shell-generation model is based on Weibel's morphology. Therefore it does not assess the deposition in the patient's airways but as if the patient has Weibel's airway structure. In Hofmann et al. (1997), the prediction model is based on a asymmetrical airway structure, different from the patient's morphology and also different from Weibel's. Thus agreement between the predictions and the SPECT measurements cannot be expected. In Hashish et al. (1998), the prediction model is based on Weibel's morphology, like the shell-generation model but not like the patient's morphology. But the deposition measured from the patient's SPECT data is not the deposition that would be obtained in a Weibel's structure. Thus agreement between the predictions and the SPECT measurements in this case also cannot be expected.

Aerosol deposition in tracheo-bronchial and alveolar regions in SPECT data were compared with the deposition predicted using the algorithm developed in Finlay and Stapleton (1995). In the prediction model were entered the measured *in vivo* V_T and respiratory cycle times used during the SPECT studies. Weibel A lung geometry used in this model was scaled uniformly to 50% TLC of each subject,

to give the model lung geometry a volume similar to that expected during tidal breathing (see Fig. 2-2). Deposition in the tracheo-bronchial region, TB_m, and alveolar region, A_m, were represented by the dosages deposited in the generations 0 to 16 and 17 to 23 respectively. Regions of interest covering central and peripheral regions in the SPECT data were drawn and a penetration index PI was calculated (see Section 3.3.2, p. 57). The comparison *in vivo* vs. computed regional deposition was done on d and d_m values. d was the relative difference between PI measured on the SPECT studies performed the same volunteer inhaling two different aerosols through a nebuliser; each study was done on a different day. d_m, for the computed data, was estimated from A_m, TB_m and a factor f taking into account the fact that central SPECT region of interest may also contain some alveolar deposition (details in Finlay et al. (1996)). Three pairs of aerosols were studied involving between 7 and 11 normal subjects. Results showed no statistical difference between computed and experimental methods, comparing d and d_m calculated for each pair for the whole population involved in each study. The paper however discussed that although theoretical intersubject variation is in good agreement with *in vivo* variation when whole populations are compared, a considerably larger number of individuals (about 65) would need to be considered to give more power to the statistical tests of this agreement and to give confidence in any conclusions regarding the similarity between the factors causing the theoretical vs. *in vivo* variation. Their final concluding remark is worth noting: "as an alternative to the use of more subjects, considerably more information about each individual's lung anatomy and physiology could be obtained in future experiments and used to develop models that are in closer agreement with individual d values".

No experimental data exist in humans to validate lobar aerosol deposition predictions.

The ICRP model that includes theoretical predictions and experimental data as well as estimates of both deposition and clearance, is widely known and used, although it has never been tested directly.

3.4.3 Summary

An alternative method to *in vivo* experiments is to predict the sites and doses of aerosol deposition by computer-modelling the behaviour of the inhaled particles in the airways. The anatomy of the respiratory tract is one of the factors influencing the predictions, as it determines the proximity of surfaces, angles of

airflow deflection and, to some extent, the amount of time an aerosol particle remains in the system. The current models described above do not reflect the variability of the structural components of the lung which lead to the variations of particle deposition observed *in vivo*. Moreover, the morphometric information on which the prediction models are based generally lack 3D reality, because of its poor description in the literature. The current anatomical models used are thus limiting the study of the effects on deposition of inter- and intra-variability of airway 3D geometrical parameters. However such information could be exploited for improving treatments. Therefore detailed knowledge of their location in space and size, that have been shown essential for anatomy modelling and aerosol deposition assessment, will also serve aerosol deposition modelling.

The predictions, at present, are available in terms of total deposition in the lungs. Most models also predict deposition in the tracheo-bronchial and acinar regions, and / or the deposition in each airway generation; two models predict lobar deposition. The experimental data available in the literature did not show that one of the models predicted particle deposition better than the others. Except for total pulmonary deposition predictions, the absence of any comparable experimental data, or in sufficient number to take into account inter-subject variability, makes the assessment of the accuracy of these models difficult. It would thus be of great interest to have, for the same subject, a realistic anatomical model that describes that person's relevant airways dimensions and 3D orientations together with experimental 3D aerosol deposition data assessed in relation to the individual's anatomy.

3.5 Conclusion

In inhalation therapy, it is of interest to know where the drug particles are deposited in relation to the subject's anatomy as it would provide a clinically meaningful assessment of the patient's responsiveness to a treatment. Such information can also be used for comparison between subjects as well as between different drug delivery devices, different drugs or for reproducibility studies.

Use of radiolabelled aerosol and 3D multi-modality imaging has been shown the most promising technique to assess experimentally such deposition. At present, only description of the spatial variation of deposition within the lung outlines has been documented. In order to derive further information clinically relevant,

realistic models of pulmonary anatomical features such as lobes, segments and airways are required.

Current models of the distribution of the air volumes in the lungs have mainly been created using manual physical measurements on lung casts. Data collection by this method is tedious and time-consuming. Furthermore models may be more realistic if based on the subject's *in vivo* data, rather than on many *post mortem* studies, as a large anatomical variability has been observed between subjects. The next chapter will thus investigate the feasibility of obtaining the 3D topology and morphology of the airways from medical imaging. The method developed will then be applied to the medical images acquired on a healthy volunteer, in Chapter 5. The objective of Chapter 6 is to develop methods to create realistic models of the lobes, segments and airways in human lungs, in a form suitable for interpretation of radiolabelled aerosol deposition images. The evaluation of the 3D realism of the models that are used at Southampton General Hospital will be attempted. Finally, the use of the volunteer's resulting models will be examined in Chapter 7 to interpret an aerosol deposition SPECT study that was carried out earlier, in relation to his own anatomy. This will create *in vivo* experimental data that may be used to validate alternative methods, including aerosol deposition prediction algorithms.

Chapter 4

Semi-automated tabulation of the topology and morphology of the airways using lung cast CT images

4.1 Introduction

The objective of this chapter was to investigate the use of CT imaging to obtain detailed information on the 3D topology and morphology of the airways. An algorithm to tabulate these data was developed as an alternative to the tedious and difficult manual measurements of airway casts, and also with a view to its use for investigating non-invasively the orientation and dimensions of airways *in vivo*.

In the following, description and discussion of each step of the development of the algorithm, along with its application to a human tracheobronchial tree cast CT images are proposed. In conclusion the use of the algorithm to compute the orientation and size of airways *in vivo* will be discussed.

4.2 Branching Network Images

The following branching network images were used to develop and validate the algorithm:

1. High resolution spiral CT scanning (General Electric Medical Systems, HiSpeed Advantage) was performed on a human lung airway plastic cast

(Fig. 4-1), loaned by the Anatomy Department, Guy's Hospital, London. This was done at the Radiology Department, Southampton General Hospital with the assistance of Mr. Peter Halson. Each scanned slice was a coronal view of the lungs. The parameters used were the following: 0.54 mm slice thickness, 1 mm x 1 mm pixel size (a pixel is a unit element within a slice of the volume), axial acquisition. The resulting image volume contained 273 slices.

2. On the same day, a simple branching network phantom made of Perspex (Fig. 4-2) was also CT scanned. It consisted of a main vertical 20 mm-diameter cylinder from which eleven smaller cylinders branched out at angles ranging from 10 to 130 degrees. Their diameters ranged from 2 to 10 mm and their lengths from 1 to 4 cm. The structure was such that, when the main cylinder was vertical, branching angles were the same as the gravity angles, i.e. all branches were in the plane of the vertical. It was built by Mr. John Boggust, technician at the Department of Medical Physics and Bioengineering at Southampton General Hospital, under the instructions of the author. The resulting image volume contained 174 slices. Each scanned slice contained a transverse view of the main cylinder. The voxel size was 1 mm^3 (a voxel is a unit element of a volume image). The purpose of the phantom was to allow for comparison of the measurements of length, diameter and branching angle (see Section 4.3.4) computed by the algorithm.

3. Testing of the image processing involved in the algorithm was also done using computer-simulated images of objects. These objects contained straight, very curved and looping branches; the images were binary, i.e. the voxels in the background had an intensity of 0, whereas the ones in the objects had an intensity of 1. The images contained a small number of slices to reduce computation (45 slices).

The 3D visualisation of all the images was done on a Sun Work station using the biomedical image display and analysis software ANALYZE^{TM} version 7.5 (Mayo Biomedical Imaging Resource, CNSoftware Inc.).

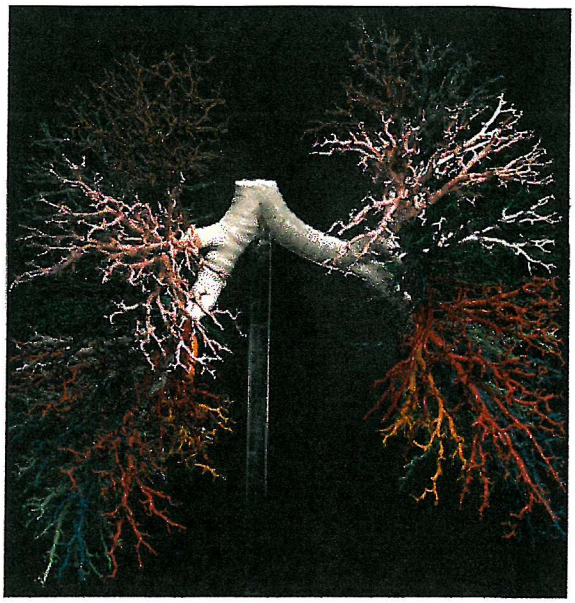

Figure 4-1: Photograph of the airway cast. It shows thousands of airways getting smaller and smaller down to less than a millimetre as one goes towards the periphery.

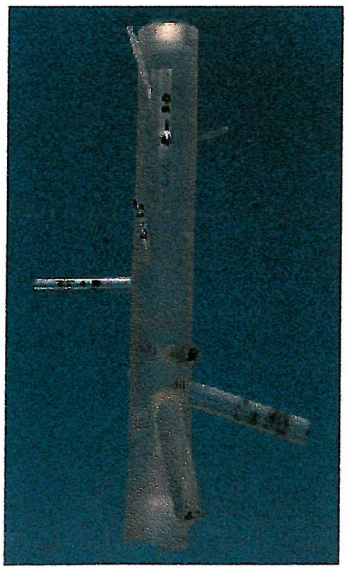

Figure 4-2: Photograph of the Perspex phantom. It consists of a main vertical cylinder from which 11 smaller cylinders branch out. 8 are visible from this view, the 3 others extend out the back.

4.3 Algorithm Step By Step

The subsequent analysis, summarised in the following diagram, was implemented in C.

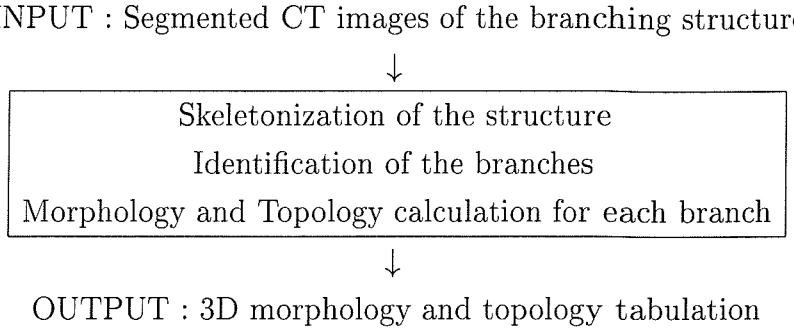

4.3.1 Segmentation

Methods

The first step in the analysis was to segment out the branching structures from the CT images. Generally, small branches had a lower CT value (i.e. a lower intensity on the CT images) than large ones. This is a classic imaging artefact, called partial volume effect, that occurs despite the use of a uniform material. It arises when a voxel lies partly on the object and partly on the background. The intensity in this voxel is therefore an intermediate value that does not correspond to the real X-ray absorption of the object. It has also the effect of blurring the edges of the object to an extent that depends on the relative size of the object and the image resolution (i.e. size of a voxel) and on the relative contrast between the object and the background. Very small branches were poorly imaged. Non-linear noise in the high resolution CT value images was removed using a median filter and an appropriate threshold was chosen to binarise the data (cast and phantom). It had however the disadvantage of excluding the very small branches.

Results

The contrast in the phantom images and in the cast images between the background-voxels and the object-voxels was high, therefore the segmentation of the branching networks was achieved by thresholding.

Figures and tables shown below are related to the cast CT images thresholded at 60 (absolute greylevel). A higher threshold would remove some of the smallest airways, a lower threshold would not allow them to be identified from the noise.

Discussion

The choice of the segmentation method is generally application dependent and is important as it conditions the images for all the future image processing. The images used in this study were CT images of solid plastic volumes and the high contrast between the background and the branching networks allowed a straightforward thresholding method. However the contrast in images of solid plastic objects is higher and the noise lower than they would be in clinical practice. In the case of *in vivo* images, thresholding techniques are of limited use in the segmentation of objects, and more complex automatic segmentation methods should be applied. The quality of those images could in theory be improved by imaging for longer and storing the data in a larger matrix. However, very detailed images will also occupy more memory space. It would also result in a higher ionising radiation dose (X-ray) which would be unacceptable for clinical studies.

4.3.2 Skeletonization

Methods

In order to measure the dimensions of each branch, the tree-like network volume had to be reduced to the middle line of each of its branches. To perform this task, the use of a thinning algorithm, also called skeletonization, was thought to be relevant. Its principle is based on the erosion of the object: object-voxels that touch a background voxel, i.e. the voxels belonging to the border of the object, are removed. The process is applied iteratively, eroding the object, layer by layer. However, several iterations eventually remove completely the object from the image. Therefore, the goal of the skeletonization process is to be able to stop some voxels to be removed; these are the voxels creating the principal lines of the object that reflect its original structure, its skeleton. For instance, all the voxels forming a cylinder will be removed, forming successively smaller cylinders, until only the minimal cylinder is left. That is the central line of the original cylinder. The constraints imposed by the skeletonization on the erosion process are:

- to preserve connectivity, i.e. an object like "o" should not be thinned down into an object like "c". This is essential to avoid splitting, or completely deleting an object or creating or eliminating a hole in an object;
- to preserve the geometry of the object, i.e. an object like "b" should not be converted in an object like "o";

- to prevent line of the object being further eroded.

These lead to some "preserving templates", that describe the configuration in which a voxel p, relative to its neighbours (see Glossary), should be preserved. Practically, the neighbourhood of each voxel of the image is assessed and compared to the templates at each iteration of the erosion process. If it matches one template, it is not removed from the image.

2D thinning algorithms are widely available [Gonzales and Wintz (1987), Lam et al. (1992)]. Their applications in the biomedical field, include analyses of chromosomes, automatic X-ray image analysis and analysis of coronary arteries. 3D thinning algorithms are more complex because connectivity and geometry preserving conditions based on 3D topological properties are difficult to address, as shown in the publications discussing those conditions [Lobregt et al. (1980), Latecki and Ma (1996), Malandain and Bertrand (1992)]. Based on the results shown in the literature, the following two algorithms appeared the most useful for our application. The first one is a facility of the software ANALYZE^{TM}. The second one was developed by Ma and Sonka (1996). It was requested from the author to Dr. Sonka, Department of Electrical Engineering, University of Iowa, who sent the source code.

Both these thinning processes were investigated. First of all the algorithms were applied to binary 2D images and to binary 3D images (a letter 'O', a letter 'A' and a three-way-cross: Fig. 4-3) to check the geometry and connectivity preservation. They were then applied to the phantom and cast images.

Results

The results of the two thinning algorithms are shown in Figures 4-4 and 4-5. Ma and Sonka's thinning algorithm conserved connectivity and geometry, whereas ANALYZE^{TM}'s algorithm did not.

Following thresholding the thinning algorithm of Ma and Sonka detected all the branches of the phantom. Figure 4-6 shows that it did not break the continuity of the network skeleton. The behaviour of the thinning algorithm depended on the ratio of parent-to-daughter diameter. The skeleton of a daughter branch which was small compared with the parent deviated from the path of a large cylinder more than a larger one (Fig. 4-7).

The skeleton picture of the airway cast is shown in Figure 4-8. Good agreement

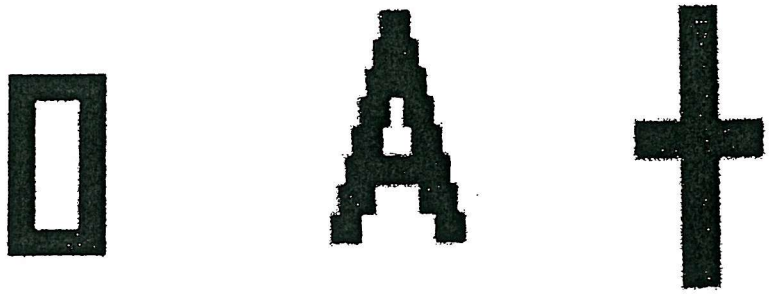

Figure 4-3: Coronal view of computer-simulated 3D objects used to test different thinning algorithms.

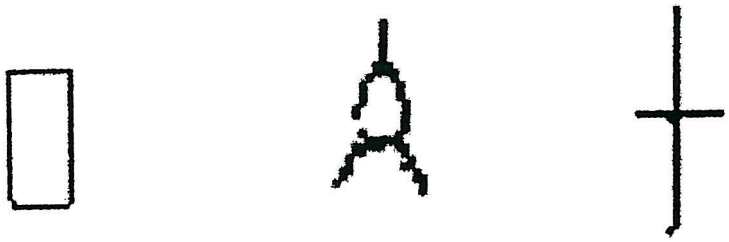

Figure 4-4: Resulting skeleton of the objects shown in Figure 4-3 using ANALYZE^{TM} thinning process.

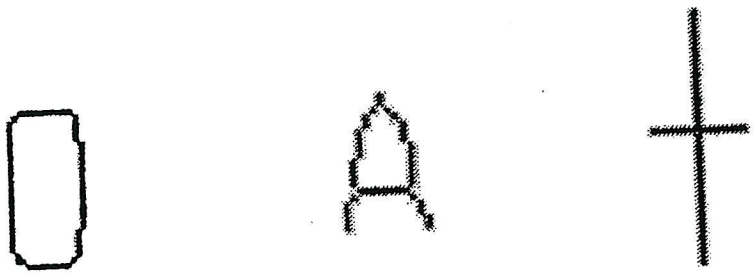

Figure 4-5: Resulting skeleton of the objects shown in Figure 4-3 using Ma and Sonka' thinning algorithm.

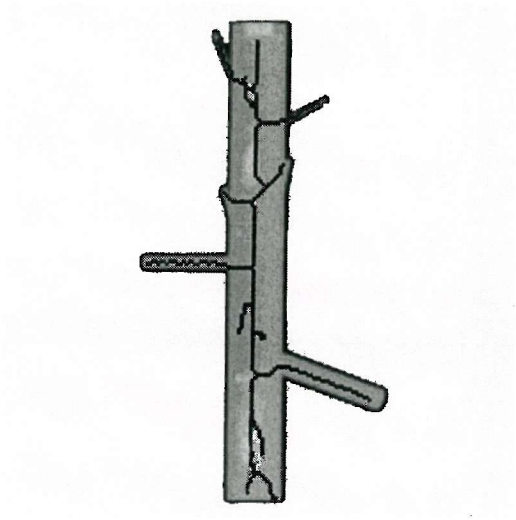

Figure 4-6: Superimposed images of the Perspex phantom and its skeleton (black lines overlaid). The perspective effect explains why some branches seem inside the main vertical cylinder. They are in fact in an oblique plane to the paper.

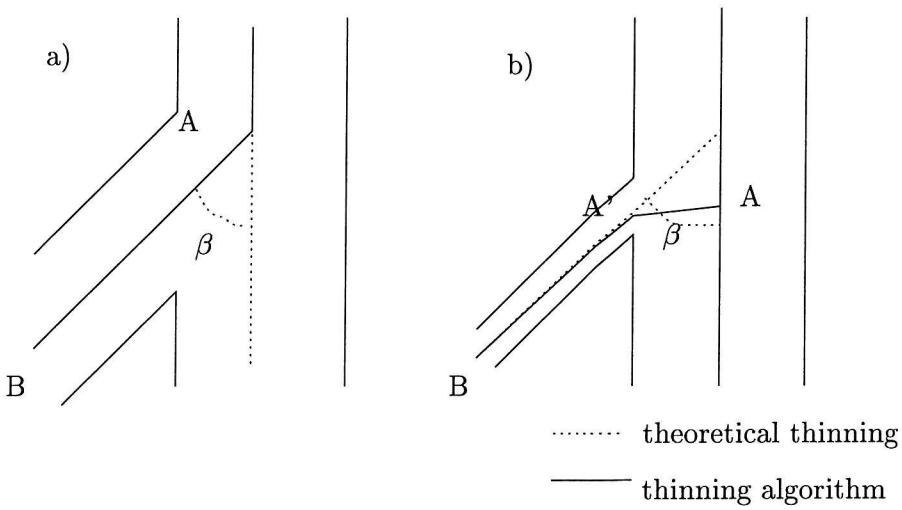

Figure 4-7: Behaviour of the thinning algorithm when ratio parent-to-daughter diameter is (a) about 1, (b) much greater than 1. In the case (b), the position of A should be changed to A' in the angle calculation equation (Eq. 4.4).

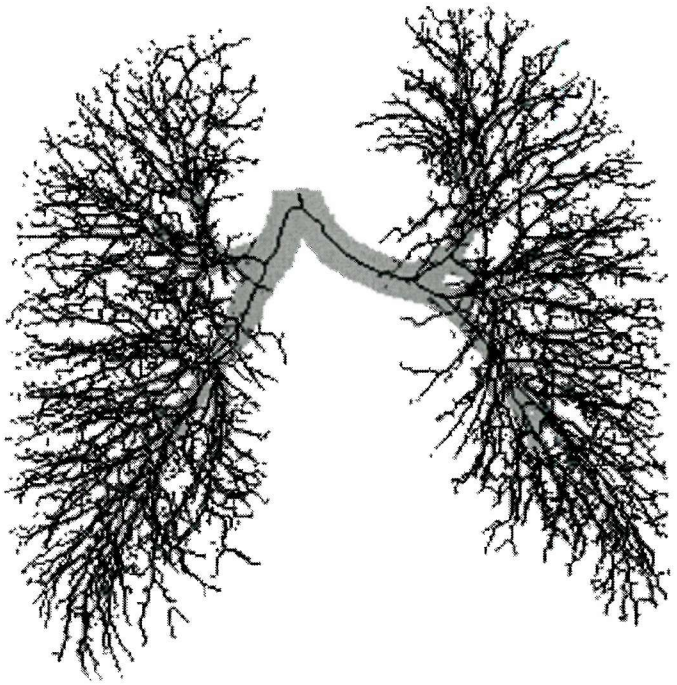

Figure 4-8: Superimposed images of the airway cast and its skeleton (black lines overlaid). The perspective effect explains why some middle branch lines seem to cross other airways.

with the original CT image is apparent.

This thinning process left unwanted spurs (Fig. 4-9a) and so an algorithm was developed for spur removal. Considering N(p) the 26-connected neighbourhood of each object-voxel p (see Glossary), this cleaning process removed the object-voxel q 26-connected to p if q had more than 2 neighbours and if q was not 26-connected to any object-voxels in N(q)-N(p)-N(N_i(p)), where N_i(p) were all the voxels in N(p), except q. This was efficient to remove spurs located along the branches but did not help in the case of a cluster around a splitting point (Fig. 4-9b). For the latter, a manual correction was needed.

Discussion

Ma and Sonka's thinning process provided a skeleton of the original CT images that represents well the main structure of the branching network (Figs. 4-6 and 4-8). Wood et al. (1995) who used a different image processing technique to find the middle lines of a much smaller set of airways, related having difficulties at identifying the location of bifurcations. In their results, some middle lines laid

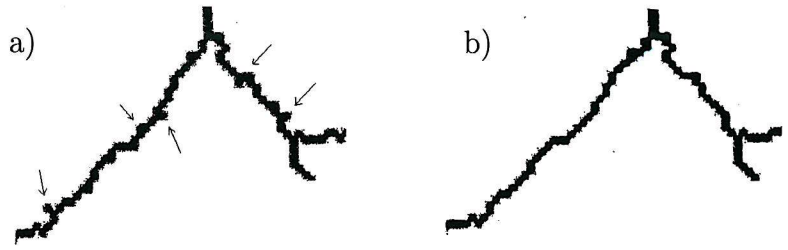

Figure 4-9: (a) The thinning operation created spurs (arrows). (b) The despuring operation removed most of them leaving the branch smooth.

outside their actual branch. The decision of using a skeletonization process was made in order to avoid this problem. Ma and Sonka's skeletonization is successful at finding a one-voxel-wide skeleton line for simple branching networks (Figs. 4-6 and 4-5) and does not create discontinuous branches. However for complex branching networks, it can generate clusters at bifurcation which then require manual correction.

4.3.3 Branch Identification And Terminology

Methods

To be able to measure each branch of the airway tree, they first had to be identified. The constraints were that:

- each airway had to be assigned a unique identification number (ID), from which the airway could be located in the branching network,
- the 3D coordinates of at least one voxel of each branch had to be known, from which the airway could be located in space.

Requirement of the knowledge of the relative location of the airway in the tree implied that the trachea should be identified first, and then its subtrees; in each subtree only bifurcations, or trifurcations would occur [Weibel (1963), Horsfield and Cumming (1967), Menache and Graham (1997)]. This suggested the use of an algorithm similar to a "binary tree-structured algorithm". This algorithm is a classical computer science process and is usually used to track the first and second branches of a parent branch in tree-structured networks bifurcating only. The algorithm presented here used the same principle but each node of the tree could be either a bifurcation or a trifurcation. With each node, information on the 3D

coordinates of the middle and end points of the parent branch and its daughter branch nodes, was stored. The input information given to the algorithm was the 3D skeleton obtained in the previous section and the coordinates of the top of the trachea. The output of the algorithm was a printing of the ID of each branch identified in the airway tree and the 3D coordinates of its middle and end points.

The algorithm followed the lines of the skeleton from the top of the trachea by determining the 26-connectivity of each point moving down the tree. The fact that the thinning algorithm did not create discontinuities in the skeleton was essential for the algorithm to be able to track down all the branches of the tree. A node was created each time a bifurcation or a trifurcation was found (connectivity of the current branch voxel ≥ 2), starting from the trachea (the top of the tree). The points along the path were deleted after processing to prevent backtracking. These were stored separately to find the middle point of the branch. The end point of a branch was when no more points were found (terminal branch) or when a node was found. This search process was inherently recursive to methodically descend all the airways of the branching network and form the tree structure of nodes. The path to each branch was also printed with a recursive routine, the direction of the first daughter branch found at a node being defined as 1, the second as 2 and eventual third as 3. It started with the trachea being defined as 1. The resulting sequence of digits formed the ID of the branch. The coordinates of the middle and end points of the branch was also printout at the same time. For each branch, a new line was written.

The output branch ID followed a convention close to the Lovelace binary convention (see Section 2.5.2, p. 30). Similarly, the relative position of an airway in the branching network is contained in the airway ID. For instance, the generation to which an airway belongs is the number of digits in its ID. It differs because of the introduction of a third daughter branch (Fig. 4-10). Also, unlike the Lovelace convention, the last ID digit (1, 2 or 3) did not refer to the relative size of the daughter airways.

The identification algorithm was first tested on computer-simulated images and on the phantom images. Because they were small branching networks, the number of branches and the parent-daughter relationships was checked visually with the original. In the cast, because of the large number of airways, this could not be done. Instead, the number of airways per generation included in the tree formation process was calculated and compared with the number of airways per generation

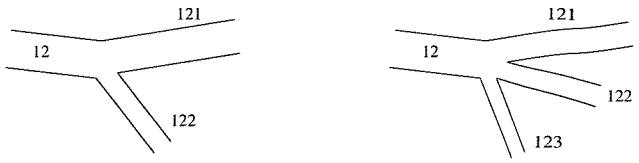

Figure 4-10: Airway identification scheme. Each airway is given a unique identification number (ID) formed by adding a digit to its parent ID. A 1 is added for the first daughter found by the algorithm, a 2 for the second. A 3 is added for the third daughter found in case of a trifurcation. The trachea ID is 1.

in an always bifurcating tree. Moreover, because of clusters at some bifurcation sites (thinning process not enough efficient, see previous section), problems in the identification of the true path down the airway daughters skeleton were suspected. Indeed, if a bifurcation is surrounded by more voxels (cluster) than the two leading to the respective first and second daughter airways, confusion would occur: if a cluster-voxel were found first, rather than the true voxel belonging to the first airway daughter, then the cluster voxel would be identified as belonging to the first airway daughter. If a second cluster voxel were found next, it would be identified as belonging to the second airway daughter. If the third voxel found finally belonged to the first daughter airway, it would be identified to belong to the third airway. Since the algorithm did not allow for more than three airway daughters, the algorithm thus would not look for other daughter branches and therefore would never go down the subtree of the "true" second daughter airway. In order to trace these errors, the voxels defined as object-points by thinning, but not by the tree formation process, were also saved in a file called the "residual file". On the basis of this file, visual examination of the bifurcation neighbourhood where such error occurred was then done, covering the number of slices necessary to understand the respective direction of the parent and daughter airways. The airway tree volume prior segmentation was also used to find errors. Manual removal of what were thought to be the cluster-voxels was then done. In addition, an error flag was included in the branch definition in the algorithm. This flag was set when less than two voxels were found along the branch, as this was more likely to be due to a cluster-related error than to be a genuine airway length in the major part of the airway tree.

Results

The algorithm was first applied to a computer-simulated image containing a branch leading to a looping branch (rather than to a bifurcation into two daughter branches). It detected a bifurcation at the starting point of the looping branch, therefore it created a node and two subtrees (one left, one right). It followed the left subtree, deleting its voxels one by one to prevent back-tracking, from the left to the right. After having found the end of the loop, the algorithm went back to the node to descend the right subtree, i.e. to follow the loop skeleton from the right to the left this time, but no voxel was found (since they had been deleted). The output of the program showed the existence of the two airway daughters: the bifurcation had been identified correctly. The residual file was empty: all the voxels had been identified. The error flag in the second daughter was also set as no voxel had been found belonging to it. From the non looping computer-simulated structures and phantom skeleton images, the identification process was straightforward, the residual files were empty, no error flag was set.

The tree reconstruction had more difficulties dealing with the cast skeleton images, because of clusters at some bifurcation sites, as expected. This residual file is shown in Figure 4-11. The identification process set the error flag of several branches that also appeared in the residual file (Fig. 4-11). In the first nine generations manual correction of 150 branches was necessary (29%, mainly between generation 6 to 9). Figure 4-12 shows the new residual data file after manual correction of the clusters. A total of 3114 branches describing the airway network were then identified, with no error flag before generation 10. The number of airways per generation is compared with a theoretical "always bifurcating" tree in Table 4.1. The two main reasons for the discrepancy after generation 9 are firstly that the airways were trimmed or not caught in the casting procedure, and secondly that the ones smaller than a millimetre were indistinguishable from the image noise.

Discussion

The tree reconstruction algorithm developed here identifies each branch of a tree-like network from its skeleton and gives the full information on its location in the 3D space. The work on the simulated images showed that it is not limited by the degree of curvature of the branches, except where the branch becomes a closed loop.

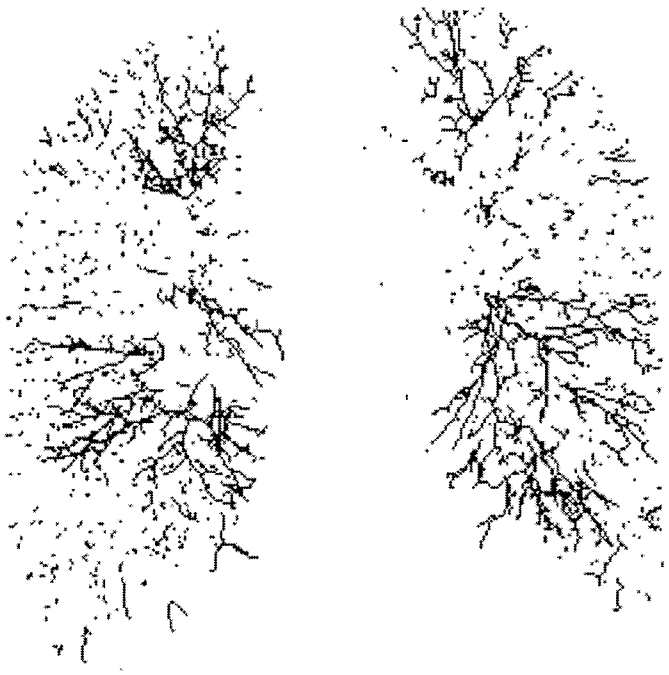

Figure 4-11: Residual data file.

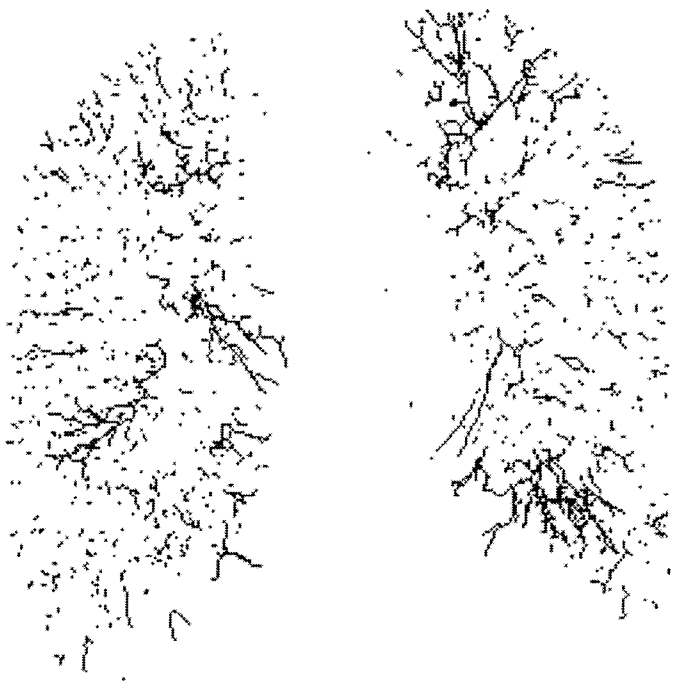

Figure 4-12: Residual data file after correction up to generation 9.

Table 4.1: Number of airways per generation number

Generation number	Computed number of airways	Number of branches (always bifurcating tree)
1	1	1
2	2	2
3	4	4
4	8	8
5	16	16
6	33[a]	32
7	66	64
8	128[b]	128
9	249[c]	256
10	345	512
11	430	1 024
12	420	2 048
13	337	4 096
14	266	8 192
15	216	16 384
16	159	32 768
17	119	65 536
18	105	131 072
19	77	262 144
20 and more	133	10^6

[a] one trifurcation

[b] two airways terminate at generation 7

[c] one trifurcation, four airways terminate at generation 8

Different systems of identification of the airways have been used in literature [Weibel (1976), Mortensen et al. (1983)]. We used the Lovelace identification scheme for its adaptability to the tree-structured algorithm.

The number of airways present in the casts used in previous work was estimated to be between 30 000 and 60 000 [Menache and Graham (1997)], but the number of single airways actually measured varied from one author to an other. The number of airways found by the computed method presented here was limited by the resolution of the CT scanners (1 mm) and the casting procedure. This limitation becomes very apparent from generation 10 and onwards (Tab. 4.1, separation line). Therefore the calculation of the dimensions of the airways (see next section) was limited to the airways in the first nine generations.

4.3.4 Morphology And Topology Calculation

Methods

The spatial location of the middle and end points of each branch from the previous section was the basis for the calculation of further descriptive parameters. Having in mind the comparison with other published calculations of equivalent parameters and various statistical analysis of these data, a global definition of all the information relative to a given branch was sought for. An effective way for the computer to achieve such calculations was to organise the data in a two dimensional array: each line of the array related to one airway and each column contained all the information relative to that airway. The line number of an airway was referred to as the "record number" of this airway. The information such as the branch ID, the 3D coordinates of its middle and those of its end points, was stored by successive reading of the output of the identification process. The relationship that exists between the parent ID and the daughter airways, allowed the following parameters to be calculated:

- generation number, defined as the number of digits in the name.
- record number of the parent segment (set to -1 for trachea).
- number of daughters.
- 3D coordinates of the first, middle and last points of the segment (A, M and B).

The following parameters were also calculated:

- morphometric information: length, direction vector, diameter, branching angle and gravity angle.
- the lobe to which the airway belonged.

The length of an airway starting at a point A and ending at a point B was defined as the Cartesian distance AB between the point A and the point B. Let the coordinates of A be (x_A, y_A, z_A) and the coordinates of B be (x_B, y_B, z_B) in the direct and orthogonal reference (O,**i**,**j**,**k**):

$$AB = \sqrt{(x_B - x_A)^2 + (y_B - y_A)^2 + (z_B - z_A)^2}. \tag{4.1}$$

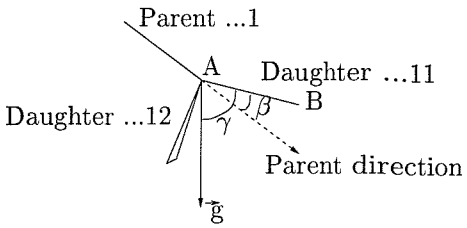

Figure 4-13: Definition of the branching angle β and the gravity angle γ.

The direction vector Δ was defined as the scalar product between **AB** and the unit vector **u**, normalised to the length AB:

$$\Delta = \frac{\mathbf{AB} \cdot \mathbf{u}}{AB}. \tag{4.2}$$

Its gravity angle (90° for a horizontal segment) was then defined as the inverse cosine of the scalar product between the gravity direction **g** and the direction **AB** (Fig. 4-13):

$$AB \cos\gamma = \mathbf{AB} \cdot \mathbf{g}. \tag{4.3}$$

The branching angle (angle formed between the parent direction and the studied segment direction) was derived from the scalar product between the parent direction **D** and **AB** (Fig. 4-13):

$$AB \cos\beta = \mathbf{D} \cdot \mathbf{AB}. \tag{4.4}$$

To calculate the diameter, first the object points that were 6-connected to a background point in the CT images were detected as edge points. For each segment **AB** and its middle point M, the points P_i were the edge points belonging to the plane Π centred in M and perpendicular to **AB**:

$$P_i \in \Pi : ax_{P_i} + by_{P_i} + cz_{P_i} = d \quad \text{where} \quad \begin{cases} a = x_B - x_A, \\ b = y_B - y_A, \\ c = z_B - z_A, \\ d = ax_M + by_M + cz_M. \end{cases} \tag{4.5}$$

The diameter $\bar{d}$ was calculated as:

$$\bar{d} = \frac{2 \cdot \sum_{i=1}^{n} MP_i}{n}, \tag{4.6}$$

where n is the number of points P_i, and as long as n ($\pm$ 10%) was greater than the number of points that a circle of diameter $\bar{d}$ would have ($\pi\bar{d}$), $\bar{d}$ was re-calculated iteratively with only the points P_i such as $MP_i < \bar{d}$.

The user had the possibility to enter in the program the ID of the five lobar airways. All the airways descendant from a given lobar airway were assigned its corresponding lobe number, based on the comparison of the first digits of their ID. Number 1 corresponded to the right upper lobe, 2 to the right middle, 3 to the right lower, 4 to the left upper, 5 to the left lower; 6 referred to the trachea and the two primary bronchi.

The effect of curvature was studied on simulated images. The result of the computation of the morphological parameters was compared with the mean of three successive manual measurements of the phantom branches applying paired t-tests. The lengths and branching angles were computed as described above but with the location of the starting point of the branches revised as in Figure 4-7. The manual measurement of the length of the branches was done by aligning a thin rod parallel to the branch. One end of the rod touched the main 20mm-cylinder. The end of the branch was marked on the rod with a pencil. The length of the branch was then measured on the rod with a ruler to a precision of 1 mm. The manual measurement of the angle of a bifurcation was done by fitting cardboard triangles in the bifurcation until the best fit was found. The angle of the triangle was measured with a protractor to a precision of 1°. The diameter of the phantom branches was measured with a Vernier gauge to a precision of 0.01 mm. The computed diameters of the few easily accessible airways in the cast were similarly compared with their manual measurements. In this case, each branch could not be measured with the Vernier gauge because of the presence of many surrounding airways. The diameters were thus obtained using a string rolled around the airway at the location estimated the middle. For each airway, the length πd of the string was then measured with a ruler to the precision of 1 mm, from which the diameter d was calculated. The statistical variation of the differences between all the manual and computed measurements was analysed. The mean values of the computed diameters, lengths, branching angles and gravity angles in the cast were compared with those found in the literature, where available.

Results

The length computation in the simulated image of very curved branches was underestimated. If the bend was located before or after the middle point of the branch, the diameter computation was overestimated. This was due to an inappropriate direction of the normal vector to the plane in which the diameter was calculated. This direction in the algorithm is defined along the vector **AB**, whereas, in the case of an asymmetrical curve between A and B, it should be defined as the tangent to the skeleton line in M. An alternative algorithm could be used to measure length and diameter in this instance, by including the coordinates of all the voxels belonging to the skeleton of the curved airways (i.e. modification of the output obtained in Section 4.3.3). Only the coordinates of the first, middle and end voxels of the skeleton of straight airways need to be saved to compute their morphology.

The standard errors of the mean of successive manual measurements of length and angle of the phantom branches were less than 1.5 mm and 1.5° respectively. The mean of the difference between the computed and mean manual measurements of the phantom branches for lengths and angles were found equal to 1.1 mm and 2.96° respectively; the standard error of the mean was 1.2 mm and 4.46°. No difference was shown in the mean differences between the mean manual and computed measurements of the lengths and angles (d.f.=12, t=0.92 and t=0.66 respectively, $p>0.1$). The 95% confidence interval on the difference in the length measurements with the two techniques was [-1.52 mm, 3.7 mm]. It was [-6.8°, 12.7°] for the angle measurements.

Figure 4-14 is the Bland-Altman graph (difference between the two methods against the average [Bland (1997)]) for the diameter calculations in the phantom. It shows an over-estimation of the small diameters. This is certainly due to the partial volume effect (blurring effect, see Section 4.3.1, p. 70) and to the fact that the number of points taken into account in the diameter calculation (Eq. 4.6) is very small (one or two points). No difference was found in the three manual measurements with the Vernier gauge. The mean of the difference in the computed and manual measurements is 0.27 mm when all the cylinders are included, the standard error is 0.13 mm. The t-value calculated on the mean of the difference between the two methods laid outside the 95% limits of agreement (mean ± 2 Standard Deviations, Fig. 4-14b) when the 2-mm diameter cylinders were included in the statistics (d.f.=15, t=2.1, $p<0.05$), i.e. showing a bias. When excluding the 2mm-cylinders, it lies inside the 95% limits of agreement showing no

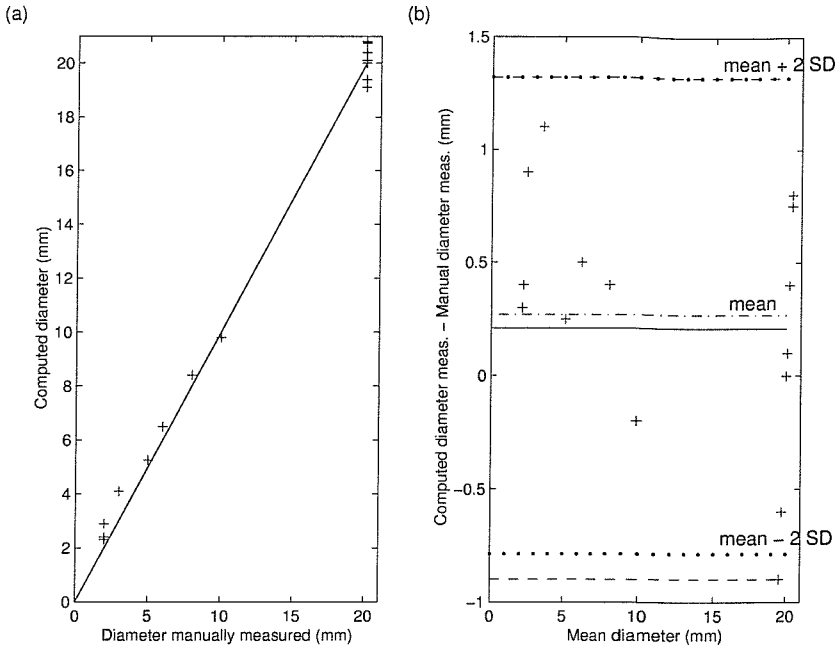

Figure 4-14: (a) The computed diameter of each branch of the phantom was plotted versus its manual measurement. No difference was found in the three successive manual measurements done with a Vernier gauge. The solid line is the identity line. (b) Bland-Altman graph for the phantom branch diameters. The dotted and dash-dotted lines show the statistic results on all the branches. The dashed and solid lines show the statistic results if the small diameters (2 mm) are excluded.

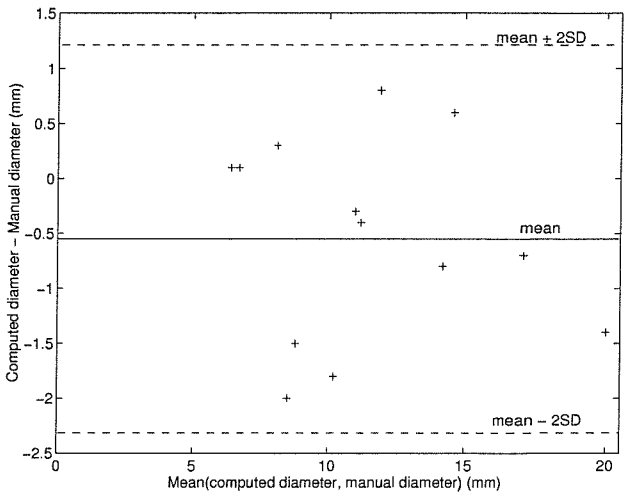

Figure 4-15: Bland-Altman graph of 13 airway diameters of the cast. The standard error of the mean of diameter calculations from three successive measurements of the circumference of each airway using a string was less than 0.7 mm.

Table 4.2: Airway diameters and lengths ratios, and mean branching angle.

	Computed data	Published data
Length/diameter	2.69^{a}	$[2.8, 3.25]^{W1}$
Smaller to larger conjugate daughters diameters	0.79^{a}	0.86^{W2}
	$[0.2, 1.0]^{a}$	$[0.5, 1.0]^{W1}$
Ratio of conjugate daughters lengths	0.58^{a}	0.62^{W2}
Ratio of daughter diameter to parent diameter	0.77^{b}	0.79^{W3}
Mean branching angle	43° ^{b}	41° ^{H}

^{a}mean or range for all airways in generations 6 to 8 of 1 mm < diameters < 4.6mm

^{b}meas. of all angles in generations 2 to 9

^{W1}Weibel (1963), range for all airways in generations 6 to 8 of 1 mm < diameters < 4.6mm

^{W2}Weibel (1963), mean for all airways in generations 6 to 8 of 1 mm < diameters < 4.6mm

^{W3}Weibel (1963), mean for all airways in generations 1 to 10

^{H}Horsfield and Cumming (1967), mean of 232 angles of which 200 were subsegmental airways

significant difference between the computed and the manual dimensions (d.f.=12, t=1.3, p>0.1). The mean of the difference in the measurements was 0.21 mm and the standard error of the mean was 0.16 mm, i.e. the confidence interval was [-0.14 mm, 0.56 mm].

The few airways accessible for manual measurements of their diameter in the cast were located in the first four generations. Thirteen airways were measured. The standard error of the mean of three successive manual measurements was less than 0.7 mm. The mean of the difference between the computed and mean manual measurements of the diameter was found equal to -0.54 mm; the standard error of the mean was 0.26 mm. T-test did not show a significant difference between manual and computed measurements (d.f.=12, t=2.08, p>0.05). The 95% confidence interval of the difference was [-1.09 mm, 0.02 mm]. Figure 4-15 shows the Bland-Altman graph of the diameters.

Table 4.2 allows some comparison with the literature. The relationship between (i) conjugate daughter diameters and lengths, (ii) daughter and parent diameters were calculated using the computed data on airways of similar generations that were used in Weibel's 1963 publication. These agree reasonably well with Weibel's data. The computed ratio of the daughter diameter and parent diameter, calculated for the conductive airways, averages 0.77. This shows that the correction in the

angle calculation made for the phantom branches was not necessary in the case of the airways. The value concurs with Weibel's relationship between diameter and generation number in his theory of dichotomy [Weibel (1963)] explained in Section 2.5.2 (p. 31). It is also within the range found by Horsfield and Cumming (1967) from the measurement of all branch diameters from a cast down to 0.7 mm (0.74 - 0.82).

In Figure 4-16, the computed diameters are averaged for each generation and plotted against the generation number for comparison with Weibel's experimental equation, which has also been explained by various theories (see Section 2.5.2, p. 31). The cast data points follow well the shape of Weibel's curve. The fact that the curve lies above most of the data points suggests that the computed diameter of the trachea was overestimated. This is quite likely as only a very small part of the trachea was included in the cast (Fig. 4-1). The computed diameter was thus calculated in a plane very near the carina which is a large bifurcation.

The mean branching angle of all the branches studied was found equal to 43°. This is near the ideal branching angle of 37° 28' forecast by the theory for dichotomy. This is near the mean branching angle and in the range of the mean branching angles (2° - 121°) found by Horsfield and Cumming (1967). Mean gravity and branching angles per generation up to generation 9 are given in Table 4.3 for the five lobes. It was found that minor daughters branch out at a greater angle from the parent than the major ones (Fig. 4-17).

Discussion

The results on the simulated images show that the calculation method is not applicable in the case of a significantly curved branch. This did not affect our measurements on the airways since they are not significantly curved, as shown in the airways skeleton (Fig. 4-8).

The manual and computed measurements of angles, lengths and diameters, excluding the 2mm-diameters, in the phantom, compared well. The difference in the angular measurements could be as large as 13° (95% confidence interval). Differences as large as 3.7 mm could be obtained in measuring airway length ranging from 15 to 45 mm (mean=25 mm). Differences as large as 0.6 mm could be obtained in airway diameters ranging from 4 to 20 mm (mean=13 mm). The range of variation between manual and computed measurements of some cast airways of

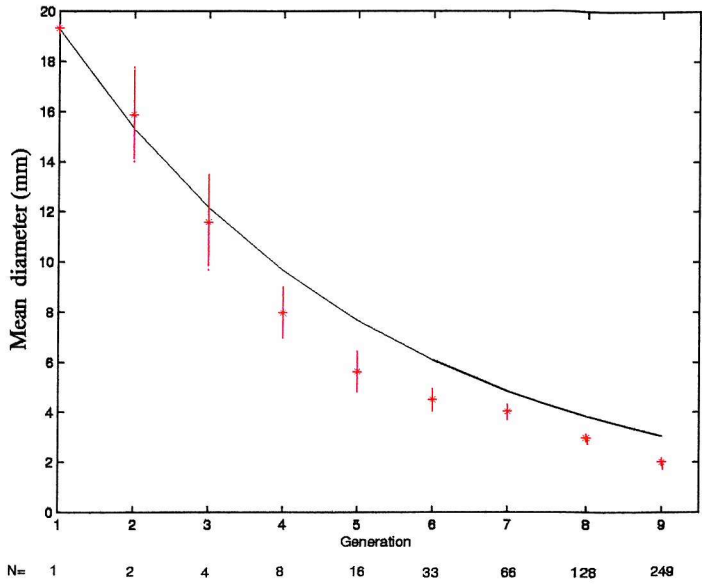

Figure 4-16: Mean diameters $d(j)$ computed from the CT images of the cast for each generation j are plotted against the generation number. The error bars represent ± 2 se. N is the number of airways included in the average calculation. The equation $d(j) = 2^{-1/3}d(j-1)$ versus the generation number is also shown (line).

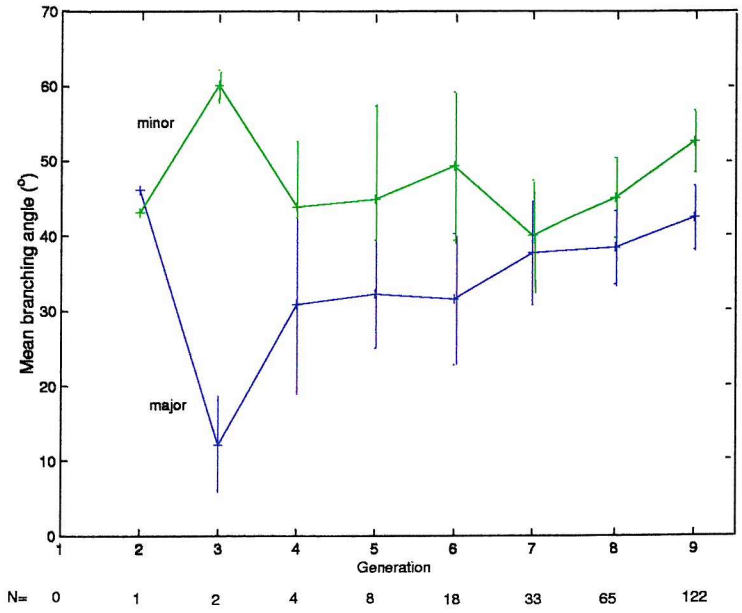

Figure 4-17: Branching angle averaged per generation for the minor (green line) and major (blue line) branches. The error bars represent ± 2 se. N is the number of airways included in the average calculation.

Table 4.3: Mean gravity angles γ and branching angles β per generation. (a) Right Upper lobe, (b) Right Middle lobe, (c) Right Lower lobe, (d) Left Upper lobe, (e) Left Lower lobe.

(a)

Generation	$\gamma(°)$	$\beta(°)$	Number of airways
1	54	+	1^+
2	47	43	1
3	101	54	1
4	107	46	2
5	106	35	4
6	106	38	8
7	94	38	16
8	97	41	32
9	94	49	64

+Trachea

(b)

Generation	$\gamma(°)$	$\beta(°)$	Number of airways
1	54	+	1^+
2	47	43	1
3	31	16	1
4	65	40	1
5	75	29	2
6	89	49	5
7	82	45	10
8	83	46	16
9	79	48	33

+Trachea

(c)

Generation	$\gamma(°)$	$\beta(°)$	Number of airways
1	54	+	1^+
2	47	43	1
3	31	16	1
4	42	38	1
5	36	62	1
6	34	40	2
7	45	43	4
8	56	35	8
9	68	36	16

+Trachea

(d)

Generation	$\gamma(°)$	$\beta(°)$	Number of airways
1	54	+	1^+
2	60	43	1
3	114	59	1
4	103	38	2
5	111	36	4
6	115	34	8
7	114	36	16
8	105	44	32
9	102	47	55

+Trachea

(e)

Generation	$\gamma(°)$	$\beta(°)$	Number of airways
1	54	+	1^+
2	60	43	1
3	57	13	1
4	72	37	2
5	72	39	4
6	77	38	8
7	77	37	16
8	76	42	32
9	81	48	65

+Trachea

diameters > 4 mm, appears larger than in the phantom (1 mm). This may come from the fact that manual measurements were difficult and therefore less precise than the ones on the phantom. These variations between computed and manual measurements appear reasonable: comparison of measurements of the same area of the lungs made by the morphometrists involved in the Lovelace cast investigations showed agreement within about $\pm 15°$ in measuring angles and within about 5% in measuring diameters and lengths [Raabe et al. (1976)]. Unfortunately a larger sample of similar manual measurements of the cast airway angles, lengths and diameters were not obtainable here without breaking the branches apart.

The phantom study showed that small diameters were overestimated, due to the resolution of the imaging technique used. It was thus important to check if the computed diameter of airways in the cast in generations unaccessible for manual measurement, were overestimated smaller diameters or if they were in agreement with previous findings. As reviewed in the previous chapter, to offer minimal resistance to gas flow and to create also a minimal volume for economy of space, the average diameters per generation follow the theoretical curve plotted in Figure 4-16. The good fit of our data with the theoretical points (r^2=0.98) shows that we were not overestimating small diameters in those first nine generations. Moreover the pattern of the points demonstrates that at each bifurcation the airway diameter decreased, which agrees with Weibel and Horsfield's general observations. This also generally held for the airway length (see Figure 5-3).

Further validation of the computed data was possible by comparing them with the relative ratios available in the literature regarding diameter, length and also average value of branching angles. A good agreement was found (Tab. 4.2). The variation of the mean branching angle of the major and minor branches with the generation number (Fig. 4-17) agrees with previous observations of Phalen et al. (1978) and Schlesinger and McFadden (1981).

In the literature branching angles and angles of inclination to gravity, have not been measured as systematically as the diameter and length values, which were measured for more or less each airway of the lung by several authors. The branching and gravity angles in Table 4.3 are thus especially valuable as they extend the data base of human lung topology.

4.4 Conclusion

The algorithm described in this chapter calculates both the location in 3D space and the morphometry of the airways from the CT images of a lung cast. Its output is the tabulation of the direction, length, diameter, branching and gravity angles of each studied airway. The limitations of the algorithm were investigated using CT images of a simple Perspex branching network (phantom) and simulated images of significantly curved and looping branches. The morphology and topology of the phantom were validated with manual measurements. A high curvature of the branches was a limiting factor. Applied to the CT images of the lung cast the algorithm produced airway dimensions in the first nine generations which compare well with previous values quoted in literature. Despite some manual intervention from the operator necessary for the thinning process, the advantage of this computational method is clear when compared with the way the human lung morphometry has been found in the literature. These were based on the dimensions of a few human lung casts measured manually, an extremely time-consuming and tedious process.

The use of CT imaging to obtain the orientation and size of the airways was shown to be useful. However, the CT resolution influenced the accuracy of the morphometry computation. It directly relates to the number of airways that can be investigated as branches smaller than the resolution are not visible. In application to *in vivo* examinations, the latter is proportionally linked to the X-ray dose delivered to the subject. As CT imaging is currently the only technique to visualise the airways in 3D (see Section 2.5.3), a compromise between the imaging time and X-ray dose and image quality and resolution has to be found.

Regarding assessment of aerosol deposition in relation to a subject's anatomy, *in vivo* airway data and radiolabelled aerosol study are ideally required from the same subject. In the next chapter the algorithm developed here will be applied to an *in vivo* CT study.

Chapter 5

Study of the 3D geometry of the central conducting airways in humans using CT images

5.1 Introduction

The purpose of this chapter was the application of the algorithm developed in the previous chapter to an *in vivo* set of CT images. These data were analysed to obtain geometrical information of interest for anatomical and aerosol deposition modelling.

The methods to obtain the *in vivo* CT image and analyse the topology and morphology are first described. A large number of data are then presented, combining the information from both the volunteer and the cast studied earlier. These detail the angular variations and patterns in the lobes, generations and at bifurcations. Finally, the data are analysed and discussed in terms of their use for 3D modelling of the conducting airway network and their relevance for predicting aerosol deposition.

5.2 Methods

A 12 cm-long CT scan containing part of the trachea was performed on a healthy 27-year old male volunteer in supine position at the end of inspiration of a tidal volume breathing cycle. This investigation was lead by the author. It had been the object of an ethics submission at the Local Research Ethics Committee, which

gave its full approval (see Appendix A). It was performed with the understanding and informed consent of the volunteer. During the 40-second scan, the subject held his breath to prevent major motion image artifacts. The images were 3 mm-thick adjacent slices, 0.703 mm x 0.703 mm pixel size. Very low X-ray power settings (120 kV, 120 mA) were used to minimise the radiation dose to the subject. This imaging protocol was produced by P.M. Halson, head of Radiological Physics at Southampton General Hospital. It involved a much smaller radiation dose than a clinical thoracic CT scan (2 mSv vs. typically 6 to 8 mSv). The radiation dose was equivalent to moving to Cornwall, which has higher natural background radiation than Southampton, for about four months of the year.

All the conducting airways in the first six generations were manually delineated out with the assistance of Dr I. Brown, consultant in Cardiothoracic Radiology at Southampton General Hospital. Higher generations were not complete as branches smaller than the CT resolution were indistinguishable or outside the limits of the scan. The data were then re-formatted into 0.703 mm cubic voxels and used as an input in the algorithm developed in Chapter 4. The skeletonization process required manual correction (clusters, see p. 79) at six bifurcations for all the airways to be identified (section 4.3.3). Morphology and topology measurements were based on the recording of the 3D coordinates of the starting point A, mid-point and ending point B of each airway (section 4.3.4). The length and diameter of each airway were obtained using Equations 4.1 and 4.6 respectively. The gravity angle defined, as in Equation 4.3, the angle formed between $\mathbf{AB}$ and the gravity direction when subject is standing up. The 3D orientation in space of the airways was further specified by defining a "coronal" angle and a "sagittal" angle. They were defined relative to the three axes of unit vectors $\mathbf{n}_\theta$, $\mathbf{n}_\psi$ and $\mathbf{n}_\gamma$ described in Figure 5-1. The coronal angle θ defined the angle formed between $\mathbf{AB}$ and $\mathbf{n}_\theta$, gravity direction when subject is lying on right side. It was calculated from the following equation:

$$AB\cos\theta = \mathbf{AB}\cdot\mathbf{n}_\theta. \tag{5.1}$$

The sagittal angle ψ defined the angle formed between $\mathbf{AB}$ and $\mathbf{n}_\psi$, gravity direction when subject is lying down on back. It was calculated from the following equation:

$$AB\cos\psi = \mathbf{AB}\cdot\mathbf{n}_\psi. \tag{5.2}$$

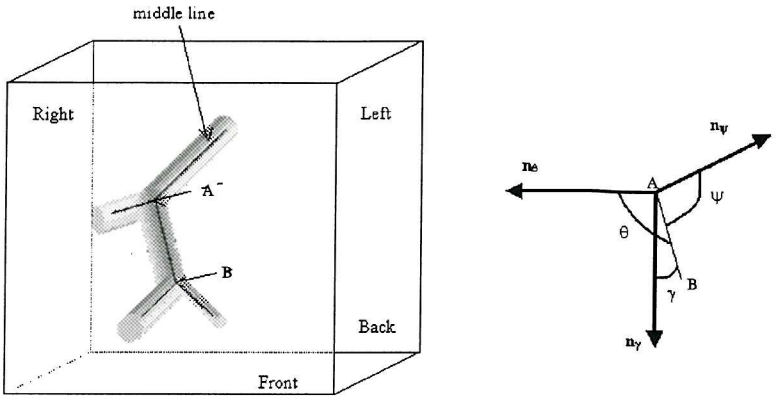

Figure 5-1: The orientation in space of an airway starting at a point A and ending at a point B is fully described by the three angles θ,ψ, γ.

The gravity angle was calculated from the following equation:

$$AB\cos\gamma = \mathbf{AB}\cdot\mathbf{n}_{\gamma}. \tag{5.3}$$

Lastly, the change in the orientation of the airways after bifurcation was investigated. Each set of two airways with the same parent i was used to define a plane $\mathcal{P}_{j,i}$, called the bifurcation plane, where j is the generation to which the two airways belong. The latter was characterised by its normal vector $\mathbf{n}_{\mathcal{P}_{j,i}}$. The rotation angle $R_{j,i}$ between two consecutive bifurcation planes of normal vectors $\mathbf{n}_{\mathcal{P}_{j,i}}$ and $\mathbf{n}_{\mathcal{P}_{j+1,i}}$, referred to as the bifurcation plane rotation angle, was then calculated, for generation j$\geq$5, using the following equation:

$$n_{\mathcal{P}_{j,i}}\ n_{\mathcal{P}_{j+1,i}}\ \cos R_{j,i} = \mathbf{n}_{\mathcal{P}_{j,i}}\cdot\mathbf{n}_{\mathcal{P}_{j+1,i}}. \tag{5.4}$$

The mean bifurcation plane rotation angle in a given generation j was thus noted R_j.

The lengths and diameters of the airways are presented in the next section, averaged for each whole data set and for each generation to be compared with previous published data. The angular parameters are presented averaged per lobe and per generation to allow lobar patterns to be analysed. Analyse of variance significance test ANOVA [Bland (1997)], which are appropriate to examine the difference between two or more group means of one single variable, are also included when further investigation per generation or lobe was relevant. As in the statistical

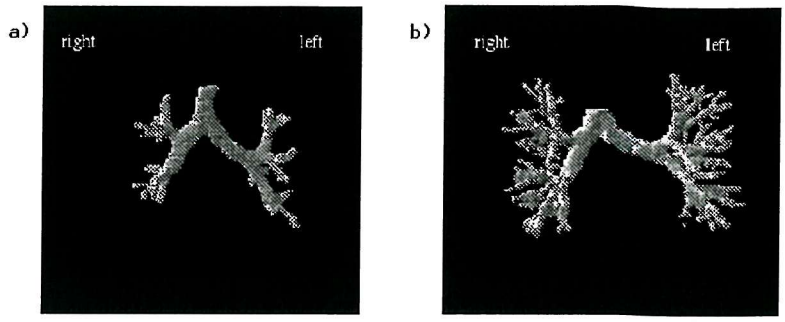

Figure 5-2: Front view of the two sets of conducting airways studied. (a) All the airways in the first six generations (volunteer). (b) All the airways in the first nine generations (cast).

study by Koblinger and Hofmann (1985), the relative standard deviation for each graph is given to allow for future use of the data by airway tree geometry modellers.

5.3 Results

Figure 5-2 shows the two sets of airways that were studied (6 airway generations in the volunteer, 9 airway generations in the cast). The airways in the volunteer data branched dichotomously, therefore 63 airways were studied. The number of airways per generation in the cast, that showed trifurcation, is given in Table 4.1.

Table 5.1 summarises the averaged relationships between daughter diameters and lengths and daughter and parent diameters for the volunteer (see Table 4.2 for the cast). These may be compared with equivalent Weibel data. Figure 5-3 shows the change in diameter and length as a function of the generation number. To allow comparison with Weibel's theory (section 2.5.2, p. 31 and Eq. 2.2, where the trachea is in generation 0), the data were fitted to a curve of the form $a.2^{b(j-1)}$ where j is the generation number and a and b are constants. This curve is a straight line using a logarithmic scale and the coefficient b is related to its slope. In Weibel's theory, this coefficient for the diameters is -0.33; no estimate of this coefficient for the lengths was found in the literature. The trachea length was not included in the length curve fitting as only a part of this airway was imaged, in both the cast and the volunteer. The cast data were obtained in the previous chapter; they are re-plotted here in the same format as the volunteer's for the ease of their comparison. The diameters are shown consistently bigger in the cast than

in the volunteer. This may be due to the casting process during which the lung was inflated. More variation appears in the length patterns than the diameter patterns and the relative standard deviation (S.D.) for the mean lengths per generation are consistently greater than the mean diameters per generation.

Table 5.1: Airway diameter and length ratios for the volunteer

	Volunteer measurements (6 generations)	Weibel (1963)
Length/diameter^{+}	3.09	range: 2.8-3.25
Conjugate daughters diameters^{++}	0.82; range: 0.3-1.0	0.86;* range: 0.5-1.0*
Conjugate daughters lengths^{+++}	0.58	0.62*
Daughter diameter/parent diameter	0.83	0.79**

$^{+}$ For 1mm < diameters < 4.6mm

$^{++}$ Smaller/larger

$^{+++}$ Shorter/longer

* generations 6 to 8

** generations 1 to 10

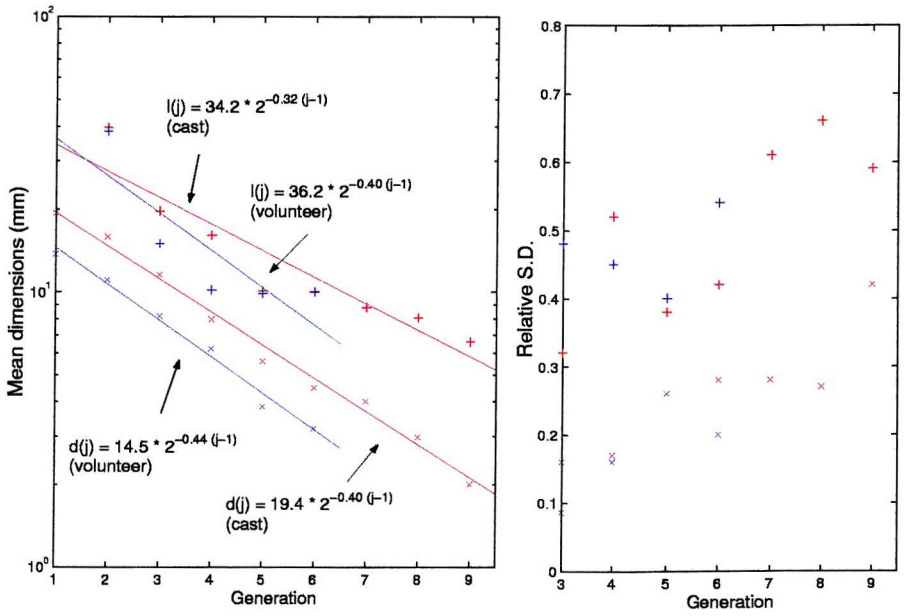

Figure 5-3: Mean diameter and length per generation and relative S.D. *Legend*: + length, × diameter. The solid lines are the curves fitting the data. Red relates to the cast data, blue relates to the volunteer's data.

Table 5.2: 3D orientation of the airways: mean angles

Generations	Angle	Volunteer measurements (6 generations)			Cast measurements (9 generations)		
		mean	se	range	mean	se	range
All	gravity, γ	84°	5°	19°-167°	89°	2°	0°-170°
	coronal, θ	84°	5°	0°-151°	90°	2°	0°-180°
	sagittal, ψ	86°	5°	4°-169°	100°	2°	0°-180°
	branching, β	39°	2°	12°-78°	43°	1°	2°-121°
2 to 4	gravity, γ	77°	12°	23°-166°	75°	10°	28°-143°
	coronal, θ	86°	10°	30°-151°	96°	12°	32°-158°
	sagittal, ψ	83°	9°	4°-135°	109°	6°	68°-150°

The mean gravity, coronal and sagittal angles are presented in Table 5.2. They are close to 90° for all the airways in both the volunteer's and the cast. The airways in the very central airways (generations 2 to 4) have a smaller angular range. Very different lobar patterns are shown for each angle in Figures 5-4, 5-6 and 5-8. The angular distribution within a given generation was also studied in generation 9 of the cast, which contained the largest number of airways (Fig. 5-5, 5-7, 5-9). ANOVA tests considering each lobe as a group showed a significant difference at 0.05 level in the gravity angle (F=3.81, d.f.(explained)=4 and d.f.(residuals)=244, p=0.005) as well as the coronal angle (F=9.76, d.f.(explained)=4 and d.f.(residuals)=244, $p<10^{-3}$); in the sagittal angle, no significant difference was shown at 0.05 level (F=2.17, d.f.(explained)=4 and d.f.(residuals)=244, p=0.07).

The mean branching angle for each generation and each lobe does not show different lobar patterns and the asymptotic values are around 40° for both the cast and the volunteer's data sets (Fig. 5-10). The mean branching angle averaged for all airways is given in Table 5.2. The distribution of the branching angles in generation 9 of the cast (Fig. 5-11) is narrow around its mean (mean=48°, SD=24.4°, N=249). The null hypothesis of no difference between lobes in generation 9 was confirmed by an ANOVA test (0.05 level), considering each lobe as a group (F=0.84, d.f.(explained)=4 and d.f.(residuals)=244, p=0.5).

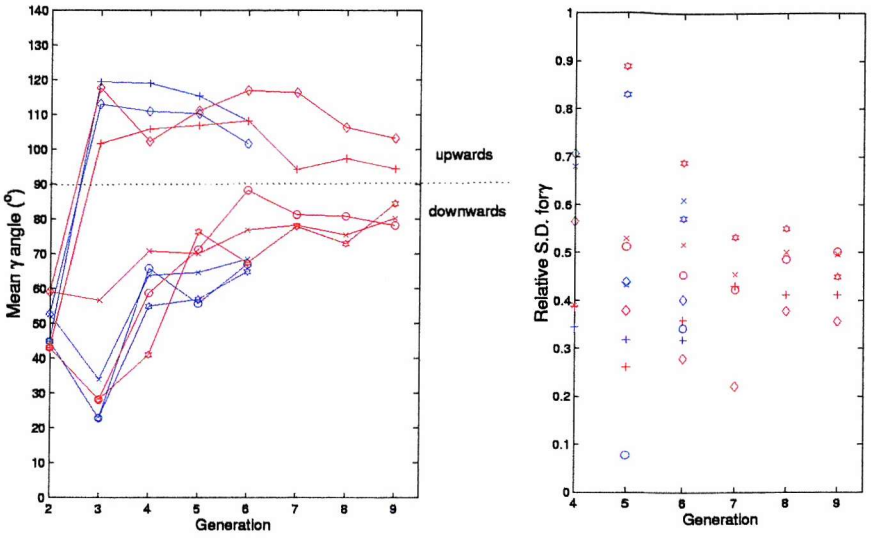

Figure 5-4: Mean gravity angle per generation for each lobe and relative S.D. *Legend*: + RU lobe, ∘ RM lobe, * RL lobe, ◇ LU lobe, × LL lobe. The solid lines are the curves fitting the data. Red relates to the cast data, blue relates to the volunteer's data.

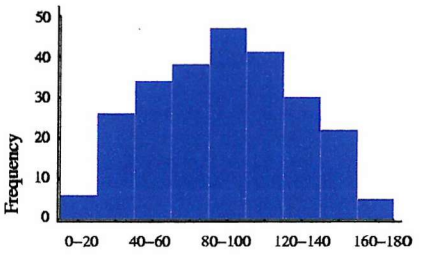

Figure 5-5: Frequency distribution of the gravity angles measured for all the cast airways belonging to generation 9. The width of each class is 20°.

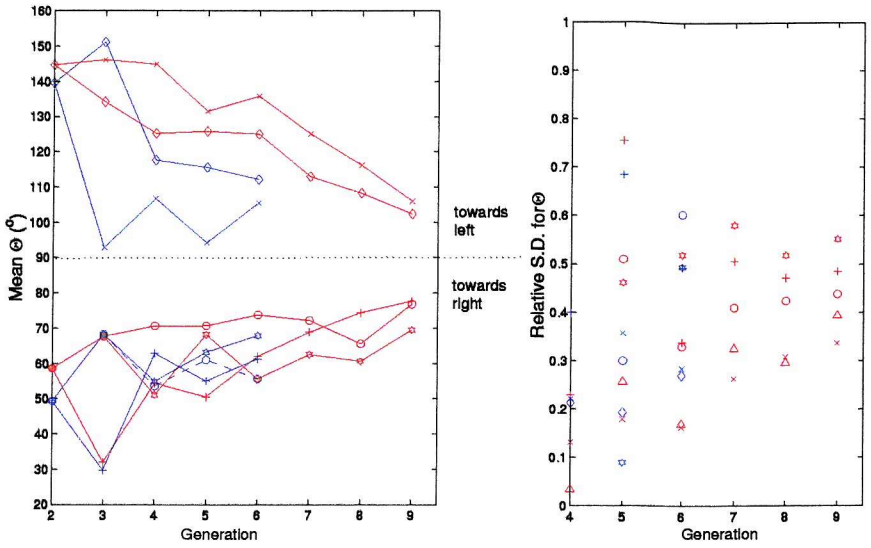

Figure 5-6: Mean coronal angle per generation for each lobe and relative S.D. *Legend*: + RU lobe, ∘ RM lobe, * RL lobe, ◇ LU lobe, × LL lobe. The solid lines are the curves fitting the data. Red relates to the cast data, blue relates to the volunteer's data.

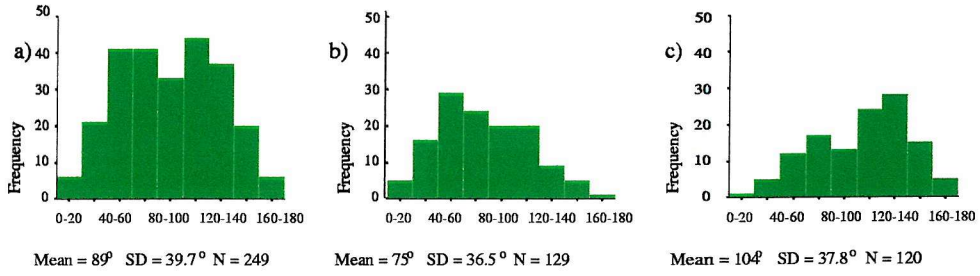

Figure 5-7: a) Frequency distribution of the coronal angles measured for all the cast airways belonging to generation 9. The width of each class is 20°. b) Calculation limited to the airways in the right lung. c) Calculation limited to the airways in the left lung.

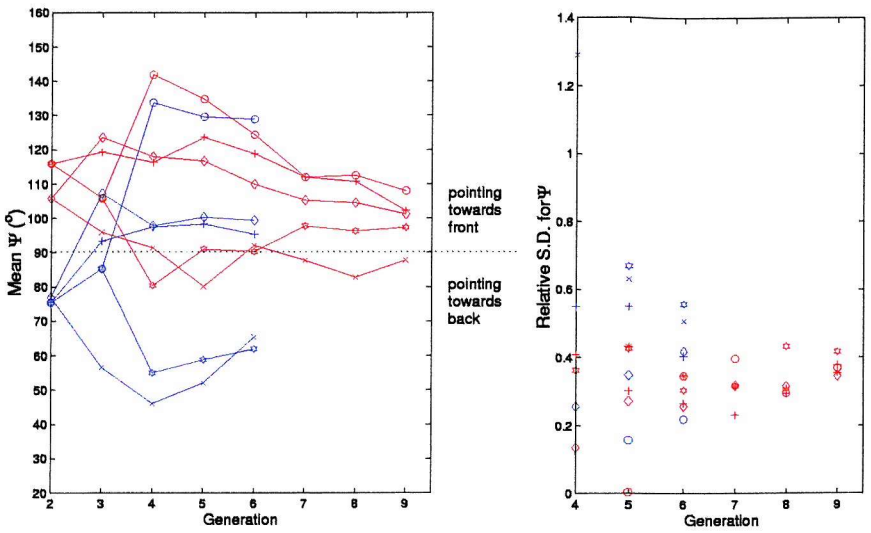

Figure 5-8: Mean sagittal angle per generation for each lobe and relative S.D. *Legend*: + RU lobe, ∘ RM lobe, * RL lobe, ◇ LU lobe, × LL lobe. The solid lines are the curves fitting the data. Red relates to the cast data, blue relates to the volunteer's data.

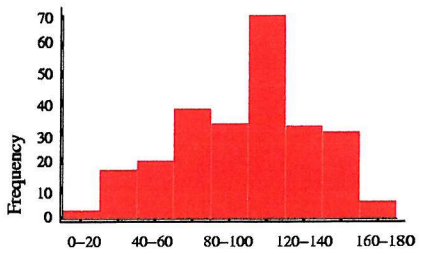

Figure 5-9: Frequency distribution of the sagittal angles measured for all the cast airways belonging to generation 9. The width of each class is 20°.

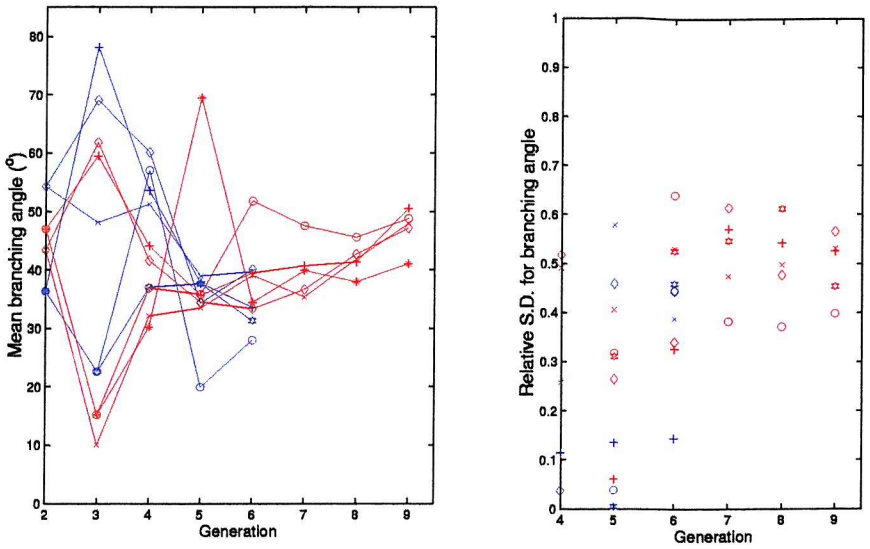

Figure 5-10: Mean branching angle per generation for each lobe and relative S.D. *Legend*: + RU lobe, ∘ RM lobe, * RL lobe, ⋄ LU lobe, × LL lobe. The solid lines are the curves fitting the data. Red relates to the cast data, blue relates to the volunteer's data.

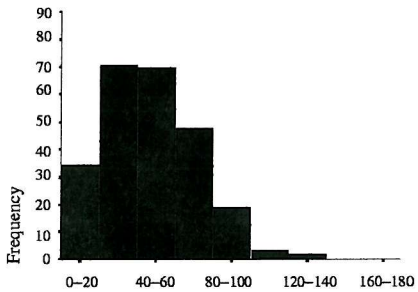

Figure 5-11: Frequency distribution of the branching angles measured for all the cast airways belonging to generation 9. The width of each class is 20°.

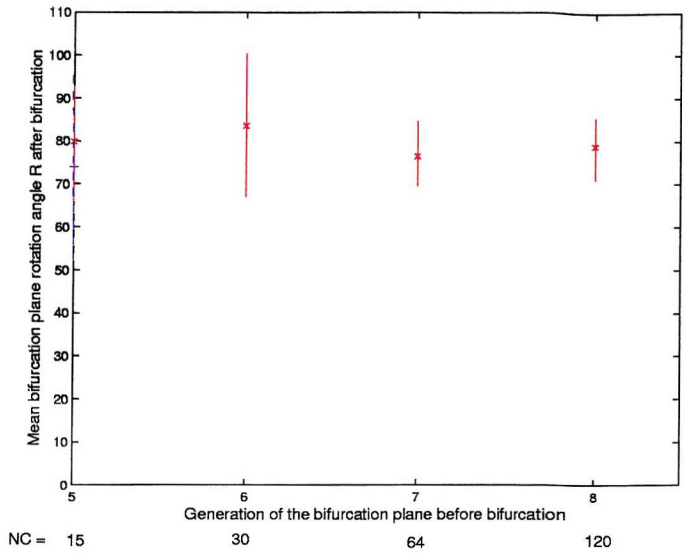

Figure 5-12: Mean and 95% confidence interval of the bifurcation plane rotation angle per generation. *Legend*: A solid line is used for the cast data, a dashed line (generation 5) for the volunteer's data. NC is the number of cases in each cast generation.

The mean value of the bifurcation plane rotation angle in generation 5 to 8 in the cast is 79° (SD=41°, N=229). Figure 5-12 shows this angle averaged per generation from generation 5. Considering each generation as a group, ANOVA test showed no significant difference between each generation at 0.05 level (F=0.20, d.f.=3 (explained) and d.f.=255 (residual), p=0.89).

5.4 Analysis And Discussion

This study adds new data on the morphometry and topology of the airways in the literature. Diameter and length measurements that have often been studied will thus be briefly analysed first. The angular data are new and will thus be analysed in greater detail.

The various relationships between length and diameter for both the volunteer and the cast compare well with Weibel's data [Weibel (1963)] that were obtained from manual measurements on a cast (Tab. 5.1). Regarding the distribution of the mean diameter per generation, the coefficient b in the curve fitting each set of data in Figure 5-3 agrees reasonably well (coefficient=-0.40 for the cast data, coefficient=-0.44 for the volunteer data), with Weibel's (-0.33) that was derived

from the average diameter of the first ten generations measured manually on a cast. A similar relationship holds for the mean length per generation (coefficient=-0.32 for the cast data, coefficient=-0.40 for the volunteer data), an observation also made by West et al. (1986). Close inspection of the ratio length to diameter per generation shows that it increases with the generation number, suggesting a non-proportional variation of the length and diameter (Fig. 5-3). This supports the Lovelace data analysis by Phillips and Kaye (1995) where the lengths were found increasing with diameters but not as fast as a simple proportionality would imply in findings by others (see Section 2.5.2, p. 31). The volunteer and cast data showed variability between the two subjects, although statistical tests to quantify intersubject variability require more data. Unfortunately, history on the way the cast was formed, during which expansion of the diameter and length of the airways could have occurred, is not available.

Angular data in the literature are very sparse. This can be explained by two facts. Firstly, manual measurements of three dimensional angles in casts are very difficult. Secondly, only branching and gravity angles were previously needed in studies on fluid dynamics or particle deposition in the lungs, using rather simple anatomical models. Regarding aerosol deposition, it was established in the literature review (see Chapter 3) that a more realistic description of the three dimensional orientation of the airways is necessary. An interest in lobar and segmental structures, rather than the average structure of the whole lung, was also confirmed. Moreover, the only set of gravity and branching angles available in the literature is from a 60-year old male silicone rubber cast. This was published in Raabe et al. (1976) and averaged per generation and per lobe in Yeh and Schum (1980). In this paper, gravity angle data were transformed to lie within a range from 0° to 90° (section 2.5.2, p. 33), therefore masking the true distribution of the airways along the vertical axis in the standing position. To our knowledge, the orientation of the airways with respect to the coronal and sagittal directions has not been studied before; nevertheless, regarding aerosol deposition these three angles together are essential to model in 3D space the correct position and location of the airways. This is a requirement for assessing radiolabelled aerosol studies in terms of deposition per airway. Moreover, it is directly relevant to studies of the effect of various breathing positions on the distribution of the inhaled aerosol in the lungs.

The airways in the very central generations have a large influence on the overall

shape of the lung, which is primarily inferior to the position of the tracheal bifurcation. Table 5.2 shows that the gravity angle in the generation 2 to 4 is less than 90° and is less than the overall mean gravity angle in generation 2 to 6 in the volunteer, 2 to 9 in the cast. In all generations, the mean gravity angles in the upper lobes for both the volunteer and the cast are greater than 90°, thus clearly upwards (Fig. 5-4). The middle lobe seems to follow a pattern similar to the lower lobes, which is downwards. Extrapolation of gravity angle variation with generation suggests that in high generation numbers ($j > 13$) the mean gravity angle would be 90° for all lobes (Fig. 5-4). If the fact that a branch is going uphill or downhill is neglected, the data are in line with the Lovelace measurements [Yeh and Schum (1980)]. Study of all the gravity angles in generation 9 of the cast (Fig. 5-5) shows them symmetrically and widely distributed around a peak at 80°-100° (mean=89°, SD=39.3°). The distribution within the lobes is respectively positively and negatively skewed in the left upper and left lower lobes.

Figure 5-6 shows that the airways in the right and left lobes on average point respectively to the right ($\theta < 90°$) and to the left ($\theta > 90°$). This basic difference in the structure of the right and left lungs is also shown in the histogram of the coronal angles measured in the cast generation 9 (Fig. 5-7a). This distribution presents two clusters, located between 40° and 80° and between 100° and 140°. This right-left structure is also confirmed by the negatively skewed distribution in the right lung and positively skewed distribution in the left lung (respectively Fig. 5-7b and 5-7c). However, as the generation number increases, extrapolation of the lobar patterns in Figure 5-6 suggests that in each lobe they will slowly tend to be distributed around 90° ($j > 14 - 16$).

Figure 5-8 shows that, unlike the gravity and coronal angle lobar patterns, the sagittal angle for the volunteer's data and the cast data is very different in the first main bronchi (generation 2, i.e. trachea daughters): as shown in Figure 5-13, the volunteer's trachea splits towards the back ($< \psi >$=75° and 77° in respectively right and left main bronchus) whereas the cast trachea splits towards the front ($< \psi >$=116° and 106° in respectively right and left main bronchus). This underlines the intersubject variability that has been seen in several studies (e.g. Raabe et al. (1976), Soong et al. (1979), Koblinger and Hofmann (1985)). In these top views, it can also be noted that $\mathbf{n}_\psi$ is perpendicular to the image border. This concurs with the normal to the subject's back because he lies on the horizontal hard bed of the CT scanner, but since the cast does not include the tissue around the airways, a

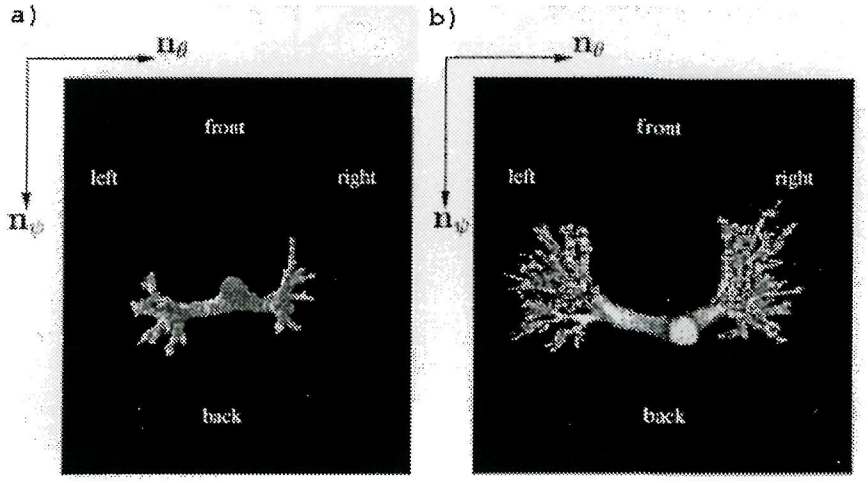

Figure 5-13: Top view of the two sets of conducting airways studied. It is clear that the trachea bifurcation into the right and left main bronchi points towards the back in the volunteer (a) and towards the front in the cast (b).

disorientation of the cast on the CT bed is possible. We thus estimate a 10° error on the cast absolute angular values. Potential angular shrinkage during the casting procedure may also be included. The distribution of the sagittal angles in the cast generation 9 shows that they are mainly distributed around 100° (mean=98°, SD=37.1°) thus, slightly more airways going towards the front of the chest than the back, extreme values around 0° or 180° being rare (Fig. 5-9). At this generation, lobar patterns cannot be distinguished (ANOVA test and Fig. 5-8).

The standard deviation for each of the three angles also varied with generation number and with lobe but the pattern of variation is similar. There was greater variability in angles in the lower generations which reduced with generation number, coinciding with all angles converging to 90° and the number of airways increasing.

In view of these results, assumptions on the orientation of the airways in the whole lung, such as a downwards tendency [Koblinger and Hofmann (1985), Hofmann and Koblinger (1990)], a radial distribution [Fleming et al. (1995)] or fixed angular values [Martonen et al. (1995)] do not seem valid in the central conducting airways. Angular patterns in the generations studied vary considerably from one lobe to another; only in high generations, extrapolation suggests a distribution centred at 90° for all lobes. Our data thus support the theory that the spatial structure of

the airways is strongly defined by the central airways.

In the literature branching angles have been studied from a fluid dynamics point of view and theory predicts a branching angle of 37°. Experiments agreed on this value as in the study by Horsfield and Cumming (1967) which used 232 angles from 116 parent airways. Hundred of these were randomly chosen in a population of airways of diameter greater or equal to 0.7mm. Sixteen of these were randomly chosen in the central airways down to broncho-pulmonary segmental bronchi. Considering the number of airways studied, the mean branching angle of 39° in the volunteer and 43° in the cast also agree with the theory (Tab. 5.2). We also showed that the branching angle is not dependent on the lobe to which the airways belong (Fig. 5-10). The 3D orientation of the airways before and after a bifurcation is of principal interest for modelling the airway tree closely to reality. The rotation angle between two consecutive bifurcation planes is assumed to be 90° in both Martonen's and Kitaoka's models, although the latter allows it to vary depending on the shape of the region to supply with air flow. In the other airway tree models, it does not appear. Recent research in arterial branching geometry suggests that non-planarity between two consecutive bifurcation planes is an important factor influencing flow dynamics. Implications such as swirling type of flow that would improve clearance of material from bends may not be restricted to vascular systems but extended to general piping systems [Caro et al. (1996)]. Most recently, Caro et al. (2000) have studied the air flow in a physical glass model consisting of a "trachea" followed by two generations of planar branches with orthogonal sequential bifurcation planes. They observed a swirling flow resembling this for non-planar bifurcations. The rotation angle of the bifurcation plane may thus be of high interest for modelling aerosol deposition behaviour at the bifurcations. It has been actually measured for the first time in this study (79°, Fig. 5-12) and confirms visual observations of casts that suggest this angle is close to a right angle. The ANOVA test did not show significant variation in the generations investigated. Data in higher generations would be valuable to confirm a constant mean value over the whole airway tree.

Future use of the data obtained on coronal, sagittal and gravity angles include identifying unrealistic parameters in the present models and, in turn, correcting them. By knowing the true distribution of the airways in 3D space, the realism of the current anatomical airway tree models can be assessed. The results on branching angles and rotation angle of bifurcation plane validate previous observations

as well as provide experimental data to confirm various theories. They also open the way to new research on flow, aerosol deposition and biological significance of such a non-planar airway tree system.

Finally, the algorithm used in this study considers the airways as straight tubes, which was shown a reasonable assumption, except for the first left main bronchus being slightly curved. All the calculations rely heavily on the accurate measurement of the 3D coordinates of the starting and end point of each airway. The facts that (1) the algorithm was successfully validated in Chapter 4 against manual measurements in a phantom and human airway cast, and (2) that analysis of the diameters, lengths, gravity and branching angles in the volunteer and the cast agrees with the previous theories and observations by others, are strong arguments supporting very reasonable results. Although CT imaging limits the number of airways that can be analysed with the algorithm, the latter is of value to provide estimates of the anatomical variability between subjects from more casts.

5.5 Conclusion

The work presented in this chapter and the previous one contributes to the knowledge of lung morphometry by providing a large set of data, especially on branching angle values and 3D topology, on which there is little information in the literature. Their analysis agrees with the previous theories and most observations, where available. Moreover it shows that the central airways geometry are generally very dependent on their location within the pulmonary anatomical features, such as lobes and contours, often preventing a "global view and description" of these airways. Non-planar geometry at bifurcations was shown. These new data will help in studying 3D flow and aerosol deposition patterns in the airways and how non-planar geometry influences them. They will also be useful for improving the 3D realism of the conducting airway structure modelling. The value of the algorithm developed earlier was confirmed as it provides detailed description of the geometric parameters of both *in vivo* and cast airway structure. Analysis of CT images of more casts using this algorithm could quickly provide intersubject data sets as well.

In the next chapter, the development of a realistic 3D image volume modelling of the central airways, lobar and segmental structures will be investigated, based on the orientation and dimensions computed above for both the volunteer and cast.

Chapter 6

3D modelling of anatomical features using medical imaging

6.1 Introduction

Clinicians are interested in delivering therapeutic aerosols to specific sites in the lungs because in order to treat different diseases, one aims for the aerosol to deposit in different parts of the lungs (drug delivery targeting). Radionuclide aerosol deposition images, such as SPECT or planar, allow visualisation of the aerosol distribution in the lungs. They are usually assessed by calculating a penetration index based on the ratio of peripheral to central activity (see Sections 3.3.2 and 3.3.2) but this quantification is rudimentary. Clearly, the quantitative analysis of these studies would be more meaningful for drug delivery targeting and for the understanding of aerosol deposition and its effect on health if it were related to lung anatomical features such as lobe, segment, airway generation or even individual airway.

Recently, the use of the conceptual shell-generation model analysis [Fleming et al. (1995)] allows spatial information to be obtained on the pulmonary aerosol deposition distribution per airway generation, based on the Weibel model (see Section 2.7.1, p. 42). Also, the use of 3D anatomical atlases give the aerosol deposition distribution per lobe and per segment, based on the location and shape of these features in the lungs of one or more cadavers (see Section 2.4.2, p. 24). However, the former model is a simplification of the real anatomy of the airways, whilst the latter shows only a standard or average partitioning of the lungs. Thus anatomical variations that exist between subjects can potentially lead to inaccuracy when deriving information on the distribution of aerosol with respect to anatomy. Im-

provements in these assessment techniques require the development of methods that generate anatomical models that reflect the size, shape and location of the subject's own anatomical features.

In vivo imaging techniques can yield some anatomical information. In particular CT has been proven useful to visualise the airways but, without further knowledge of bronchial anatomy, it cannot indicate the generation to which a given airway belongs, nor its relative position in the airway tree. CT and MR can both be used to visualise the lobar fissures from which the lobes are clearly defined. However the true morphology of the segments cannot be obtained from any imaging techniques.

The aim of this chapter was to investigate the use of the anatomical data obtained in the previous chapters, to create realistic 3D models of some of the pulmonary anatomical features, namely the airways and the segments, with minimal intervention of the operator. Validation of the conceptual shell-generation model analysis was also attempted. The methods developed to create and validate such models are first described and tested on the volunteer's and cast data. The resulting models are then presented and compared with the "true" corresponding anatomical features where available. Finally, the realism and use of the models are examined.

6.2 Methods

6.2.1 Modelling The Airways Using CT Images

This model should be a 3D image volume of the airway tree. From it, one should be able to identify each airway. Information about the relative position of a given branch in the airway tree, for instance its generation number, should also be easily obtainable.

The method was built on the algorithm developed in Chapter 4. This algorithm tabulated, among others, the diameter and direction of each airway of the branching network from its skeleton. To obtain this information, it used the 3D images of the airway tree. It also assigned each airway a unique record number and tabulated the generation and the lobe to which that airway belonged. Briefly, the algorithm developed in this section is a reconstruction of the skeleton, in terms of meaningful parameters.

The image process developed in this section was as follows. Let M_i be a voxel

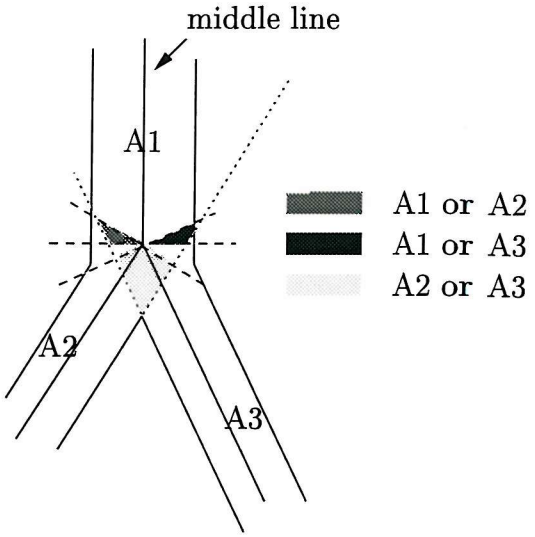

Figure 6-1: Several values are possible for pixels located at bifurcation site. A flag identifies them.

along the middle line (skeleton) of the airway i. At each M_i, the voxels inside the circle centred in M_i, of diameter d_i and oriented in the plane perpendicular to the airway direction were defined as part of the airway i and were assigned the branch i record number. This way, the same voxel value related to a unique airway.

The program was tree-structured. It went down the skeleton tree, filling in the airway voxels with the appropriate branch record number. To define the frontier line between airways at airway bifurcation sites, the following rule was applied: if a voxel p belonged to an airway A1, then its value was set to A1. If it could also belong to another airway A2, then a flag on the voxel was set, showing this duality (Fig. 6-1). The closest object-voxel without flag was then searched and its value given to p. In the case of several non-flagged voxels of different value at the same distance to the flagged one, the initial value of p was kept. Finally, the subtraction of the created volume image from the binarised original cast CT images identified the voxels that were missed in the airway voxel assignment. This occurred as some "wrinkles" on the airway wall make the diameter along the airways vary slightly. Those voxels were given the value of the most numerous same voxels in the 6-voxel-neighbourhood. Once all the voxels of the image were processed, their value was either 0, i.e. background voxels, or the record number of the airway they belonged to.

The same process was followed to model the airway generations. In this case, the voxels in each airway i were assigned its generation number.

The methods to create a model of the airways and of the airway generations were tested using the volunteer's and cast airway tree CT images, from which the topology and morphology were tabulated in Chapters 4 and 5. The 3D realism of the resulting models was assessed by comparison with the original CT images.

6.2.2 Modelling The Segments Using CT And MR Images

The method developed in this section endeavoured to simulate the process by which the partition of the lungs into segments occurred in the lung formation. The morphogenesis of the lobes and segments is thus reviewed first.

Basis of the method

The development of the pulmonary lobes and segments that will lead to their adult shape starts *in utero*. At about 4 weeks of fetal development, the respiratory system begins as an outgrowth (laryngotracheal bud) of the endoderm of the foregut, precursor of some digestive organs, just posterior to the pharynx (Fig. 6-2). As this bud grows, it elongates and differentiates into the future epithelial lining of the larynx and other structures as well. The middle portion of the bud gives rise to the epithelial lining of the trachea. The distal portion divides into two long buds which grow into the epithelial lining of the bronchi and lungs. As the lung buds develop, they branch out into the secondary bronchi, leading to the five independent lobes. They continuously rebranch to give rise to all the bronchial tubes. The segmental bronchi B^i and daughter airways (Fig. 6-3) supply individual segments Si of the lungs as the closed terminal portion of the tubes dilate and become the alveoli of their segments.

Figure 6-4 shows the segments on the cast used in the thesis as an example of the adult lung partition. Each (secondary) lobar bronchus LBi leads to one of the five lobes. Here, the air volume is isolated from the rest of the lung by the fissures. The RU lobe contains the brown, grey and pink airways that have grown from LB1 and belong to the segments S1, S2 and S3 respectively. The RM lobe contains the dark blue and red airways that have grown from LB2 and belong to the segments S4 and S5 respectively. The RL lobe contains the dark green, yellow, orange, light blue, light green and white airways that have grown from LB3 and belong to the segments S6, S7, S8, S9 and S10 (light green and white airways).

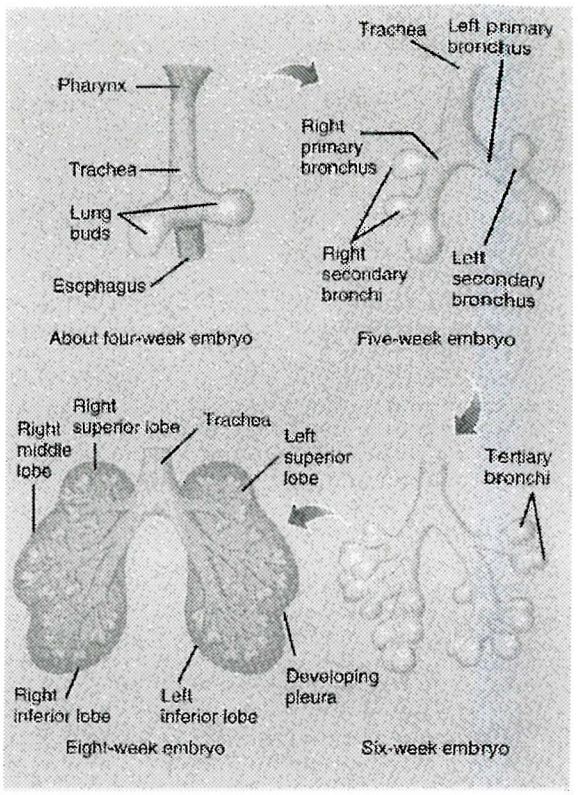

Figure 6-2: Development of the bronchial tubes and partition of the lungs. (Copyright ©1996 by Biological Sciences Textbooks, Inc. and S. Reynolds Gabrowski. Reprinted by permission of John Wiley & Sons., Inc., from Tortora and Reynolds-Grabowski (1996)).

The LU lobe contains the brown, grey, pink, dark blue, white and red airways that have grown from LB4 and belong to the segments S1, S2, S3, S4 (dark blue and white airways) and S5 respectively. The LL lobe contains the dark green, yellow, orange, light blue and light green airways that have grown from LB5 and belong to the segments S6, S7, S8, S9 and S10 respectively.

Method

From the above description, it was felt that the structure of the very central airways is important in the final aspect of the segmental partition. Therefore the method to model the segments should include these airways. Moreover, the steps of the lobe and segment formation and the description of the acini in a 6-year old child by Boyden (1971) heavily gave the impression that, within the lung space available to them, the airways were always filling more and more space, each region fighting for its own space, first at a lobar level, then at a segmental level. The

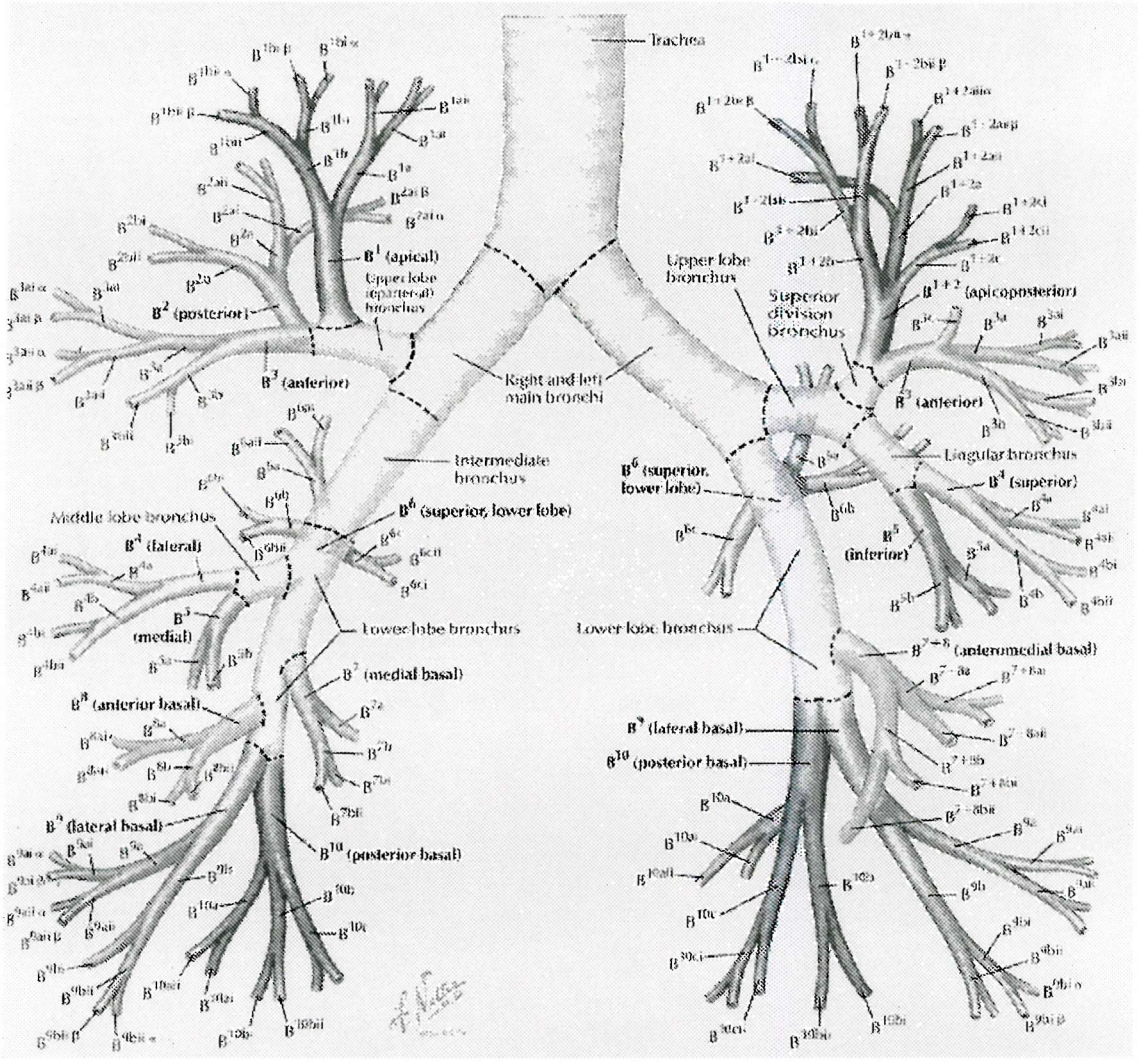

Figure 6-3: Nomenclature of the bronchi. Segmental bronchi (B^i) are numbered from 1 to 10 in each lung, leading to independent pulmonary segments. In left lung, B^1 and B^2 are combined as are B^7 and B^8. Subsegmental and further bronchi are indicated by addition of lower case letters, Greek letters and Roman numerals. Variations of the standard bronchial pattern shown here are common, especially in peripheral airways. (Copyright ©1989 by Novartis. Reprinted with permission from Netter (1991), Plate 191. All rights reserved).

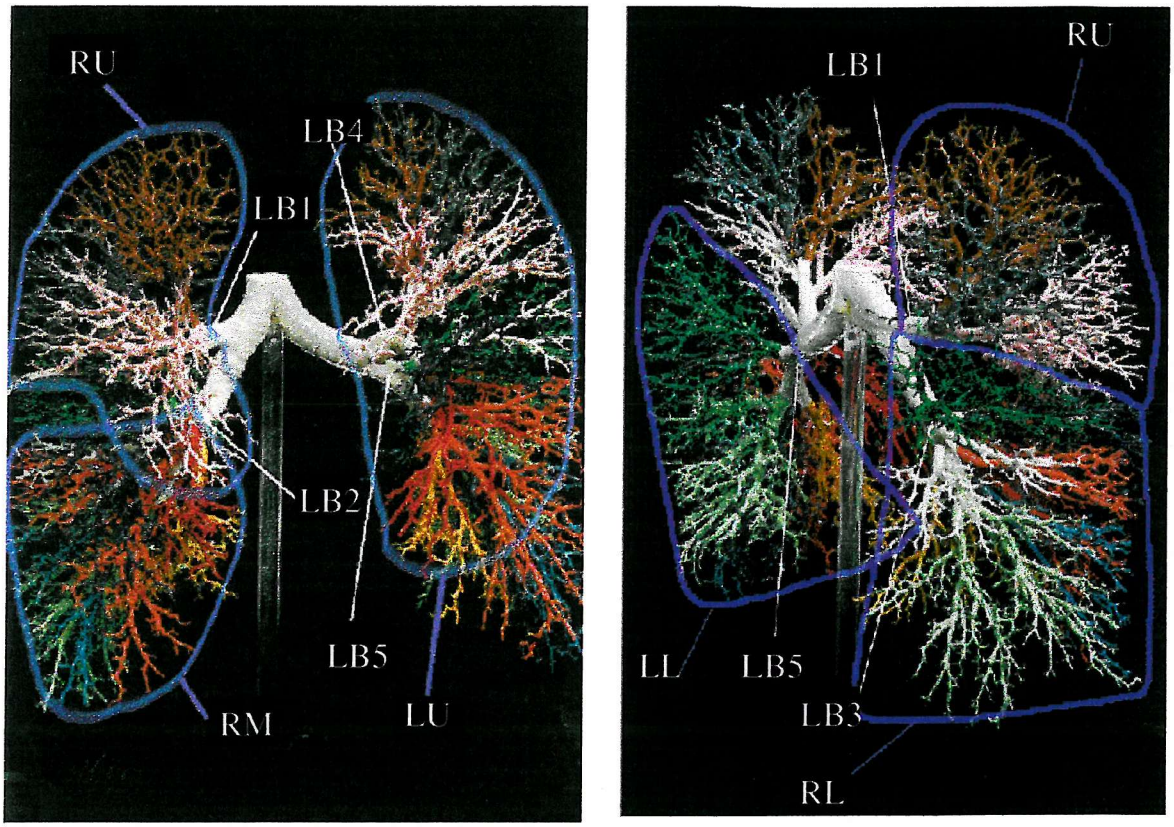

Figure 6-4: Photographs of the cast. Each (secondary) lobar bronchus LBi leads to the RU, RM, RL, LU and LL lobes of which the air volume is isolated from the rest of the lung. The blue pencil lines illustrate the location of the fissures. For each lung, the segments are colour-coded: brown for S1, grey for S2, pink for S3, dark blue for S4, red for S5, dark green for S6, yellow for S7, orange for S8, light blue for S9 and light green for S10. (see text for the small white airways)

simulation of this growing process should thus include this feeling of aggregation. The validation of the resulting models should be done with the "true" shape of each segment, but this cannot be obtained *in vivo* with the current imaging techniques (see Section 6.1). Therefore it was decided to first investigate the modelling of the lobes, which can be validated using their "true" shape, location and size. The method was then extended to create a segmental model.

Let the lung space be defined by its outlines (see Section 6.2.3). Using the airway model developed above, the lobe to which the airway belongs was known (see Section 6.2.1). This allowed the airway model to be reconstructed in terms of lobes: the value of all the voxels of the airways belonging to the lobe i (i=1 to 5) was set to i. The voxels assigned to 1 were called the "seeds of the RU lobe", those assigned to 2, the "seeds of the RM lobe" and so on. A seeded region growing process was then applied to create the lobes. This procedure was as follows. From each set of seed points regions were grown by appending to each seed point those neighbouring voxels that were inside the lung boundaries but not assigned a lobe value i yet. Each voxel appended to a region was given the value of the corresponding seed. The voxels belonging to the trachea and primary bronchi were not considered as voxels needing to be assigned a lobe and were therefore unchanged at the end of the process. The growing of a region stopped when no more voxels satisfied the criteria of inclusion in that region.

The procedure was iterative: at each iteration the neighbourhood of all the seed voxels is first assessed before changing the value of the neighbouring voxels. This allowed for the frontier between regions to be defined with the same rule as in Section 6.2.1, using flags.

To partition the lungs into segments, the method required the operator to identify the voxel value of the segmental bronchi B^i corresponding to each of the 10 segments of each lung in the airway model developed above (see Section 6.2.1). From these record numbers, all the airways belonging to the same segment could also be identified, due to the relationship between the record number and the branch ID and the fact that the ID first digits of the descendant of a given segmental bronchus are the segmental bronchus ID (see Section 4.3.3 and Fig. 4-10). The value of all the voxels of the airways belonging to the segment i (i=1 to 10 in each lung) was then set to i. The same seeded region growing method as for creating the lobes was used to create the segments in each lung. For each segment, the boundaries of the lobe to which it belonged were used rather than the lung bound-

aries. Again, the voxels belonging to the trachea, primary and lobar bronchi were unchanged at the end of the process, and the procedure was iterative. Flags were used to define the frontier between segments.

This process, aggregating voxels to form the lobes and segments, was felt to describe best the way the lungs have gained their final partition. The initial selection of the seeds belonging to a region was chosen to consist of all the complete generations of bronchi present in the airway model because no precise data was available in the literature on the relative rate of bifurcation of the airways in each lobe or segment.

This method to create lobes and segments was tested using the volunteer's and cast airway models (see Section 6.2.1) and lung outlines (see Section 6.2.3). Assessment of the 3D realism of the resulting volunteer's lobar model was done using the lobes obtained from the segmentation of the lobar fissures on the previous CT images. Comparison of the lobar and segmental models of both the volunteer and the cast was done with the lobar and segmental description available in the literature and a 3D segmental atlas. Preliminary estimation of the effect of the number of complete airway generations taken into account in the growing process on the realism of the resulting segmental model was done using the first six and the first nine airway generations of the cast.

6.2.3 Lung Outlines

Volunteer's images

The lung outlines were defined from an MR study that was carried out in 1995, with the same subject on whom the above volunteer's CT scan was performed. This study was part of a project on aerosol deposition reproducibility, involving twelve subjects in which a SPECT scan was also performed (see Section 7.2.1). However, because the volunteer had not changed either weight, size or diet (non smoker) and did not have any record of respiratory or chest problem or serious infection, it was considered reasonable to assume that his airways and lung size had not changed in the period (four years) between the MR and CT examinations.

The MR scanning procedure, in which the author was not involved, was the following. It was performed to cover the whole length of the lungs, the subject lying down horizontally and breathing at tidal volume. Landmarks were placed on each nipple, on the sternal notch and xiphoid. The lung volume was imaged using a

T1-weighted MR protocol, 8 mm-thick contiguous slices and the voxel size was 1.4 mm x 1.4 mm x 8 mm.

Registration of the MR images to match the size and orientation of the airway models, i.e. multi-modality image registration, usually relies on the matching of the landmarks. A minimum of three is required to correct for 3D rotations of one image with respect to the other one. In our study, however, because the CT images did not cover the whole lung, only the nipple markers could be matched. The MR outlines of the lungs were segmented out manually using the medical imaging package ANALYZE^{TM}. The MR volume was then re-sampled (interpolation) to match the CT voxel size (ANALYZE^{TM} package facility) and correction for mis-orientation was done manually, using the imaging package threeD (Fig. 6-5), by aligning the trachea and the trachea bifurcation in the two modality images. This was used rather than the lung edges since the CT lung volume was constantly slightly greater than the MR one, due to the different breathing pattern used during imaging. Because of the cartilage around them, the trachea and the first major airways, are not greatly affected by breathing at this level of resolution.

Cast images

Neither shape nor size information on the space volume occupied by the lungs from which the cast was formed, was available. Thus the lung outlines had to be created.

To perform this task the CT images of the cast, segmented out from the background as explained in Section 4.3.1, were used. The value of the voxels in this volume image was either 1 (object voxel) or 0 (background voxel). The gap between two object voxels was filled in to form a first shape. To prevent the two lungs from merging, a maximum distance between two voxels was required (4 cm). The fact that a few conducting airways were missing and the absence of the acini and surrounding tissue were compensated for by dilating this volume. This process used a so-called "mask" (also referred to as template), which is a small aggregation of voxels. Their value, called coefficient, was, in this case, 1. The procedure was as follows. The centre of the mask was moved around the image. If the centre of the mask was superimposed on an object-voxel, every voxel that was contained within the mask area was assigned the corresponding mask coefficient. The result was that the edge of the first shape formed was dilated. A spherical mask was used in this process to get smooth edges. The thickness of the rim added was 14

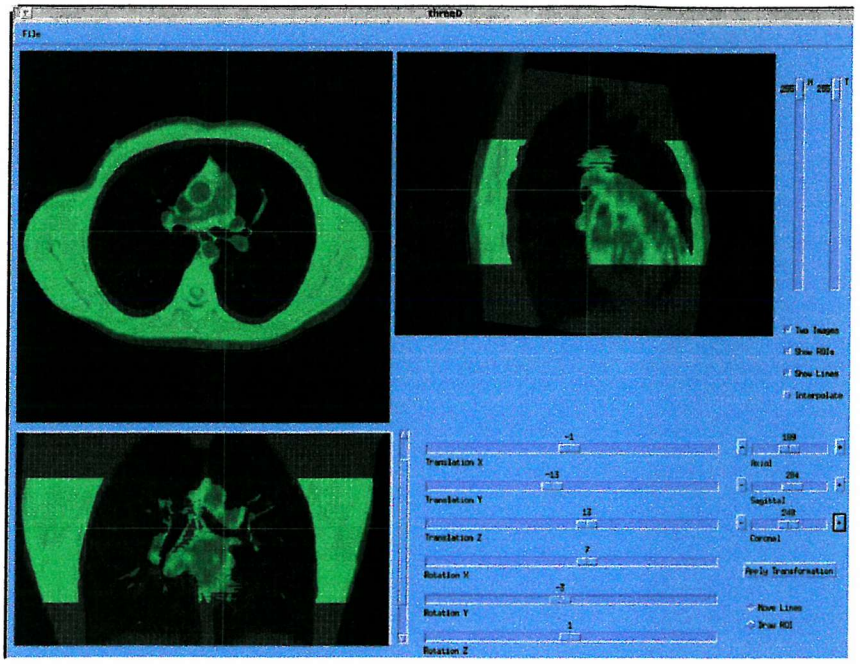

Figure 6-5: threeD allows simultaneous visualisation of transverse, coronal and sagittal views of the studied volume and a template image (green). The planes through which the views are cut are selected by the user using a scrolling bar for each direction. The registration is achieved by adjusting the studied volume to the template. The available operations are translations of the studied volume along the x, y and z axis as well as rotations with respect to the centre of the volume. The imaging package threeD was developed in-house at Southampton General Hospital by PM Halson.

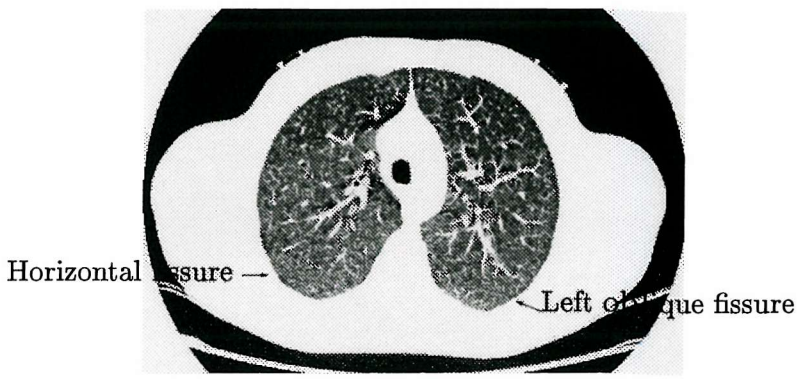

Figure 6-6: Visualisation of the fissures on a CT slice. One can also identify the trachea, the cross-section of the V-shaped nipple markers (and the strip of tape holding them). The bed and the inner shape of the scanner are also clear.

mm. This value was chosen on the ground of the mean longitudinal path length in the acini reported by Haefeli-Bleuer and Weibel (1988), that is 9 mm, and the approximate lengths of the last conducting airways (5 mm) (very small airways not imaged). The trachea and the first main bronchi were not dilated since they do not have alveoli around them. The final dilated volume was zoomed down in size such that it fitted within a 256 x 256 x 256 matrix.

6.2.4 Lobe Outlines

The true lobe outlines were sought in order to allow discussion on the realism of the shape and size of the lobes modelled in Section 6.2.2.

The volunteer's CT study showed the fissures rather well (e.g. Fig. 6-6) because the slices were thin and adjacent (see Section 2.4.1). Each lobe was thus segmented out manually. This was done with the assistance of Dr. IW Brown, consultant in Radiothoracic Cardiology at Southampton General Hospital. In the case of the lower lobes, the CT scan field of view did not cover the whole length of the fissures. They were thus extrapolated to the lung edges (less than 2 cm).

On the cast, the fissures can be easily located as the airways are distinctively gathered in each lobe, leaving clear wide gaps.

6.2.5 Air Volume Matrix

Rather than a 3D model of the airways such as developed in Section 6.2.1, Fleming developed a two-dimensional matrix to describe the distribution of the air volumes in each generation with respect to the distance to the periphery of the lungs. The "conceptual shell-generation model air volume matrix" using Weibel's anatomical data is presented in Fleming et al. (1995) normalised to a 1376 ml air volume right lung. In order to assess the 3D realism of this conceptual distribution of the airway generation per shell, the two-dimensional shell-generation air volume matrix corresponding to the volunteer's airway data was calculated. This consisted in dividing the lung into "shells" and for each shell, counting the volume in each airway generation. Each matrix component $M_{j,s}$ contained the air volume that was both in the generation j and in the shell s:

$$M_{j,s}(\text{ml}) = N_{j,s} \cdot \text{ Voxel Size } (\text{mm}^3) \ \cdot 10^{-3}, \tag{6.1}$$

where $N_{j,s}$ was the number of voxels in the generation j and in the shell s.

The air volume in each of the first six generations, restricted to the right lung, was obtained from the 3D model per airway generation developed in Section 6.2.1 and the right lung outlines obtained from the MR study (see Section 6.2.3) were used as well.

Each shell was defined as follows. A hemisphere centred in the hilum H (Fig. 6-7), of radius R was subdivided into ten smaller concentric hemispheres i also centred in H. The radius r_i was i tenths of R. The ratio $\frac{a}{R}$ was calculated for each voxel Q of the hemisphere i, where a was the distance between H and Q. In the lung volume the line containing H and in the same direction as (QH) was defined. The distance c between H and the point L_s located at the intersection of this line with the lung surface was calculated. The voxel P such that the ratio $\frac{HP}{c}$ was equal to $\frac{a}{R}$ was said to belong to the ith shell. The effect of a small change in the location of the hilum position on the air volume matrix content was also investigated.

To allow comparison, the conceptual matrix was scaled to the total air volume in the volunteer's right lung. The latter was estimated using the density data per shell obtained in Fleming et al. (1995) from a CT study covering the whole lung of a healthy subject. The air volume was calculated in each shell and then summed for all shells.

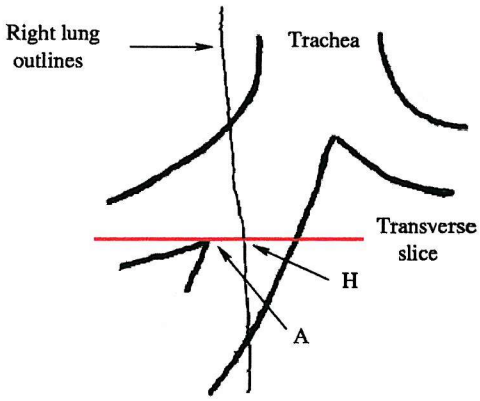

Figure 6-7: Definition of the hilum position H. The hilum area was identified in the middle coronal slice that covers the volume of the upper lobe bronchi, at the intersection of the right upper lobe bronchus and right main bronchus. The transverse slice containing the inferior point A of this intersection was also identified. The hilum position H was defined at the intersection of the coronal and transverse slices and of the lung tissue border.

6.3 Results

6.3.1 3D Models Of The Airways Using The Volunteer's And Cast Images

Figure 6-8 shows the resulting 3D models of the airways and airway generations using the volunteer's and the cast skeleton and CT images. The model per airway uses a different voxel value (intensity) for each airway, giving therefore 507 shades for the cast and 63 for the volunteer. The models per generation contain nine shades for the cast and six for the volunteer. These models imitate the shape of the original CT images.

6.3.2 3D Models Of The Lobes Using The Volunteer's And Cast Images

Figure 6-9 shows the lobes modelled using the volunteer's images. The respective shape of each lobe is very similar to the "true" ones segmented out in the CT images (Fig. 6-10). This agreement also holds for their respective sizes (Tab. 6.1).

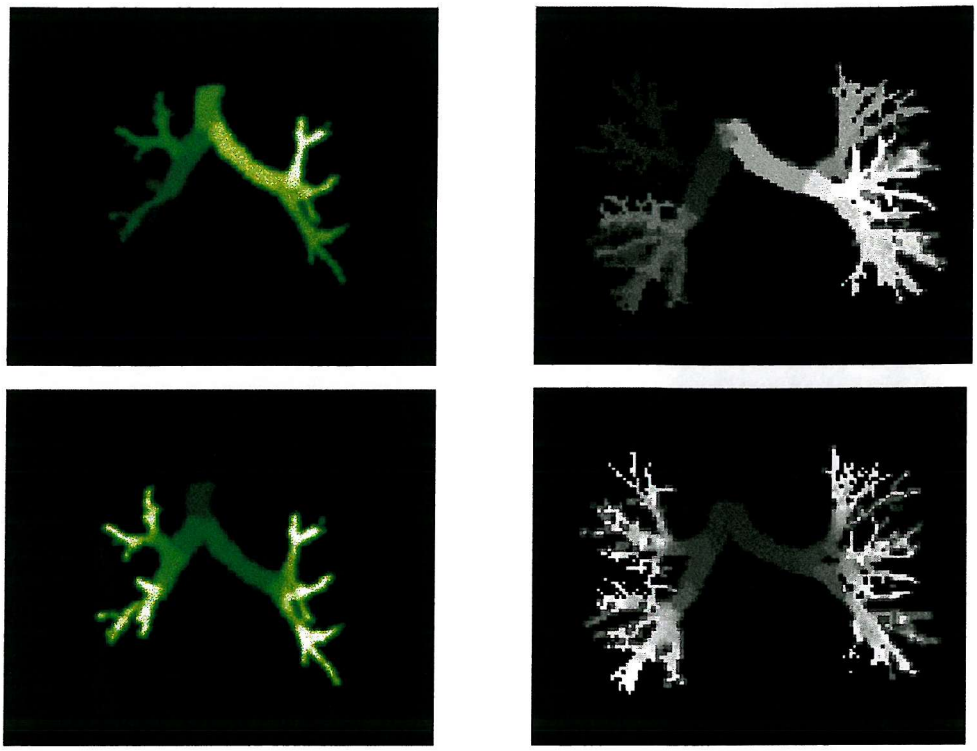

Figure 6-8: Airway models reconstructed from the CT images. (Left column) Reconstructions from the volunteer's CT images. (Right column) Reconstructions from the cast CT images. (Top row) Maximum intensity projection volume render of the 3D computed model of the airways. Each shade represents an airway. Note: The airways represented by dark shades are difficult to visualise. (Bottom row) Maximum intensity volume render of the 3D computed model showing the generations. Each colour represents an airway generation.

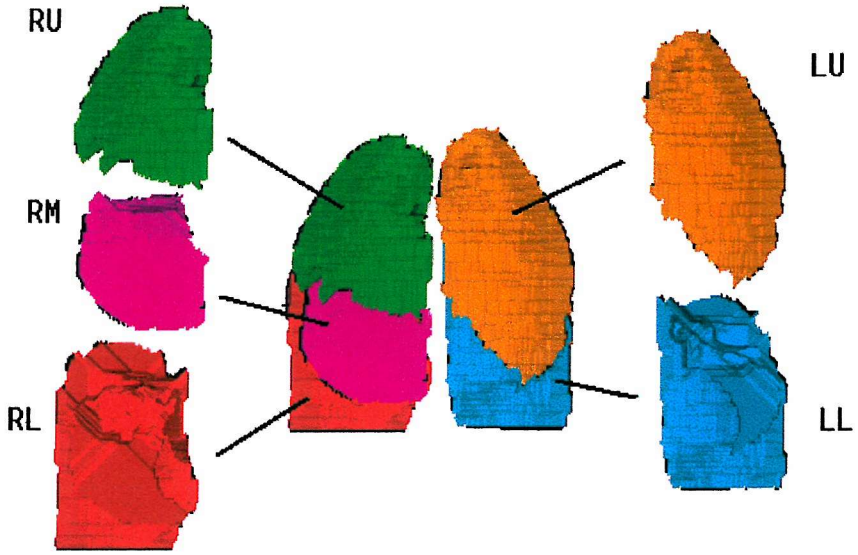

Figure 6-9: Modelled lobes using the volunteer's images. The lung outlines were segmented out from the volunteer's MR study. The growing process was applied to the lobar airways and daughters, up to generation 6. This figure can be compared with the size and shape of the lobes that were segmented out manually from the CT images (Fig. 6-10).

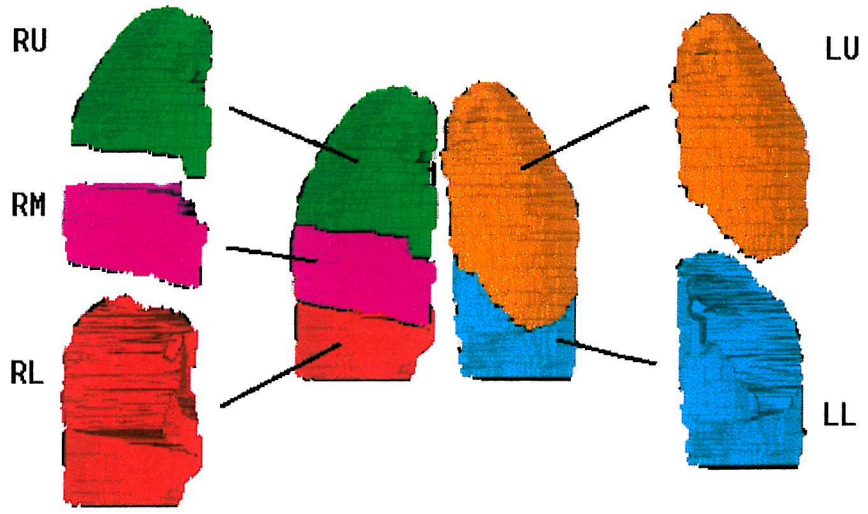

Figure 6-10: Manual segmentation of the lobes by identifying the location of the fissures in the volunteer's CT images. The lung outlines were segmented out from the volunteer's MR study.

Table 6.1: Relative lobar sizes in % of total lung volume.

Lobe	Model from volunteer	Model from cast	CT fissures (volunteer)	Horsfield et al.$^{+}$ (cast)	Yeh and Schum^{++} (cast)
RU	18.0	19.6	17.5	21	17.8
RM	7.2	11.1	7.5	9	7.1
RL	26.7	22.3	26.8	25	28.4
LU	26.7	24	26.7	20	17.6
LL	21.4	23	21.4	25	29.2
Right:Left	1.1	1.1	1.1	1.2	1.1

$^{+}$(1971), estimated from airway volume of all branches of diameter $\geq$ 0.7 mm (7 300+ airways)
$^{++}$(1980), estimated from number of 3 mm-diameter branches in the Lovelace data

Figure 6-11 shows the lung outlines and the lobes modelled using the cast images. The dilation process that was used for obtaining the total lung space preserved some of the general features of the cast such as the concavity surrounding the area where the heart would lie and the general rounded costal surface. The location of the lobar fissures in the model (Fig. 6-11) is very similar to what can be estimated from the gaps separating the lobes in the cast (Fig. 6-4), except for the oblique fissure that is angled slightly downwards in the solid cast (see Section 6.3.3). The LU lobe airways in the model and in the solid cast make a pronounced bend around the heart concavity, whereas in anatomical books they lie next to the heart (e.g. Fogelman and Maisey (1988)).

The relative sizes of the different lobes for the volunteer and what has been found in the literature from cast studies show variations (Tab. 6.1), chiefly in the left lungs. The LU lobe in the volunteer is bigger than the LL lobe (ratio LU:LL of 3:2); the opposite is seen in the observations of Horsfield et al. (1971) and Yeh and Schum (1980) (ratio LU:LL close to 2:3).

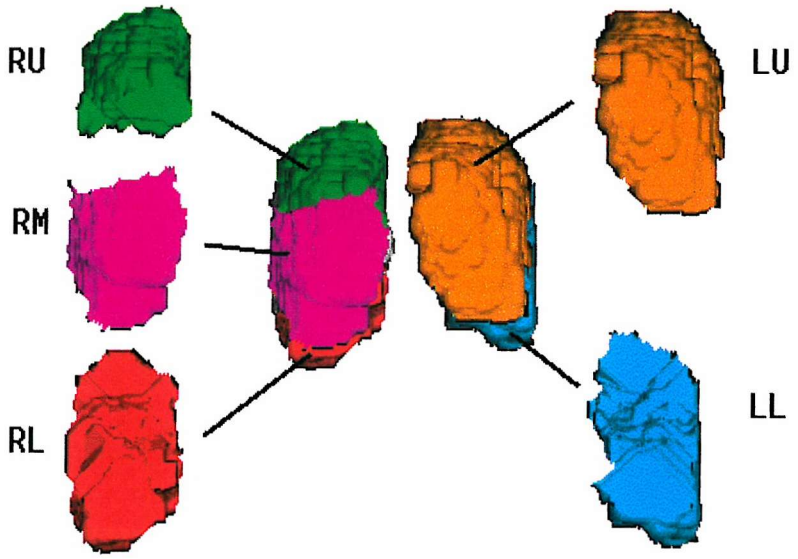

Figure 6-11: Modelled lobes using the cast images. The lung outlines were created using the cast CT images and a dilation process. The growing process was applied to the lobar airways and daughters, up to generation 9. This figure can be compared with manual drawing of the lobes on the cast photographs (Fig. 6-4).

Table 6.2: Relative size of the segments in % of total lung volume.

Lobe	B^i +	Si++	colour++	Volunteer (6 gen.)	Cast (6 gen.)	Cast (9 gen.)	In-house atlas*
RU	B^1	S1	brown	5.2	5.8	6.8	0.5
	B^2	S2	grey	3.9	6.3	6.3	3.8
	B^3	S3	pink	8.8	7.2	6.3	5.8
RM	B^4	S4	dark blue	2.2	3.2	6.5	1.2
	B^5	S5	red	5.0	7.5	4.2	4.1
RL	B^6	S6	dark green	11.6	9.0	6.0	5.7
	B^7	S7	yellow	15.1[a]	13.2[a]	1.5	4.4
	B^8	S8	orange	[a]	[a]	2.2	11.7
	B^9	S9	light blue	[a]	[a]	12.6[b]	2.0
	B^{10}	S10	light green	[a]	[a]	[b]	11.4
LU	B^1	S1	brown	2.2	4.9	3.2	1.5
	B^2	S2	grey	4.2	2.0	4.1	1.0
	B^3	S3	pink	8.0	5.4	6.6	5.1
	B^4	S4	dark blue	9.8	11.3	7.4	4.4
	B^5	S5	red	2.5	0.9	3.1	4.1
LL	B^6	S6	dark green	5.0	7.2	7.9	6.8
	B^7	S7	yellow	11.5[c]	6.6[c]	8.8[c]	11.6[c]
	B^8	S8	orange	[c]	[c]	[c]	[c]
	B^9	S9	light blue	2.9	5.9	4.8	3.6
	B^{10}	S10	light green	2.1	3.3	1.5	10.7
connections				0.1	0.2	0.2	0.7

+ see nomenclature of the segmental bronchi B^i in Figure 6-3

++ each segmental bronchus B^i supplies air to the segment Si, colour-coded as in Figure 6-4

* see details in Figure 2-3

[a] $B^{7+8+9+10}$, [b] B^{9+10}, [c] B^{7+8}

6.3.3 3D Models Of The Segments Using The Volunteer's And Cast Images

Figure 6-12 shows the segments modelled using the volunteer's airway model and outlines images. Table 6.2 shows their relative sizes. The segments S7 and S8 are combined because the bifurcation into the left B^7 and B^8 bronchi could not be seen. Similarly, partition between the segments S7, S8, S9 and S10 was not possible in the right lower lobes as the airways branching off the right lower lobar bronchus, namely B^7, B^8, B^9 and B^{10}, were not identifiable. The resulting segmental model agrees on some points with the contours that radiologists would manually draw, as described in Thompson et al. (1999), in a lung following the "typical" bronchial

pattern (Fig. 6-3). In particular, the truncated cone-like shape of S1 in the right lung and the relative position of S4 and S5 (side by side in the right lung, both touching the lung surface at their anteroinferior edges; stacked one on top of another in the left lung) in the model agree with Thompson et al. On the other hand, following these guidelines, the combined shape of S1 and S2 in the left lung should be similar to the combined shape of S1 and S2 in the right lung. This is not observed in the volunteer's model, nor in the solid cast. The large differences in sizes and shapes of the volunteer's segmental model with the Southampton in-house atlas model (see Section 2.4, p. 24 and Fig. 2-3) show intersubject variability.

All the segmental bronchi were identified in the nine generations of the cast images, except for the left and right bifurcations into B^9 and B^{10} that occur in the solid cast at generation 10. The shape of the cast segments using either 6 or 9 generations is illustrated in Figure 6-13; their relative sizes are given in Table 6.2. More segments are present in the model using nine generations. Observation of the shape of S1, S2, S3, S6, S9 and S10 in the right and left lungs shows only slight variations between the two models. Compared with the solid cast, where all the airways of a given segment have been painted the same colour (Fig. 6-4), they agree rather well. The differences in the size of S4 and S5 in the right lung and also in the left lung are striking. Their partition in the solid cast is also different, although closer to the model using nine generations. In the right lung, some of the airways of the S3 segment, in generations greater than nine, make a sudden and significant curve downwards and towards the left lung. S5 touches the lung surface and the cardiac cavity. It is located underneath the pointing lower part of S3. S4 touches S5, S6, S8 and S3. It lies underneath a horizontal part of the surface of the latter. In the left lung, some airways of S3 also makes a sudden drop and curve around the heart. S4 lies underneath this oblique and downwards part of the surface of S3. Close examination of the airways also shows that two airways from the right lateroinferior part of S3 have been trimmed in the cast, thus not taken into account in the region growing process (note *a* in Tab. 4.1).

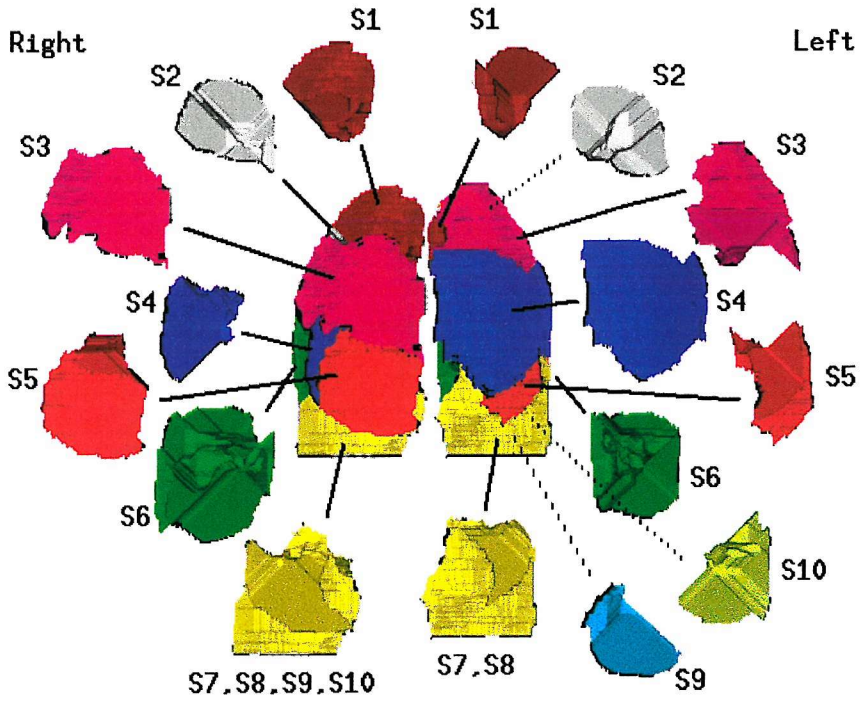

Figure 6-12: Modelled segments using the volunteer's images. The growing process was applied to the segmental bronchi and was limited by the lobe contours.

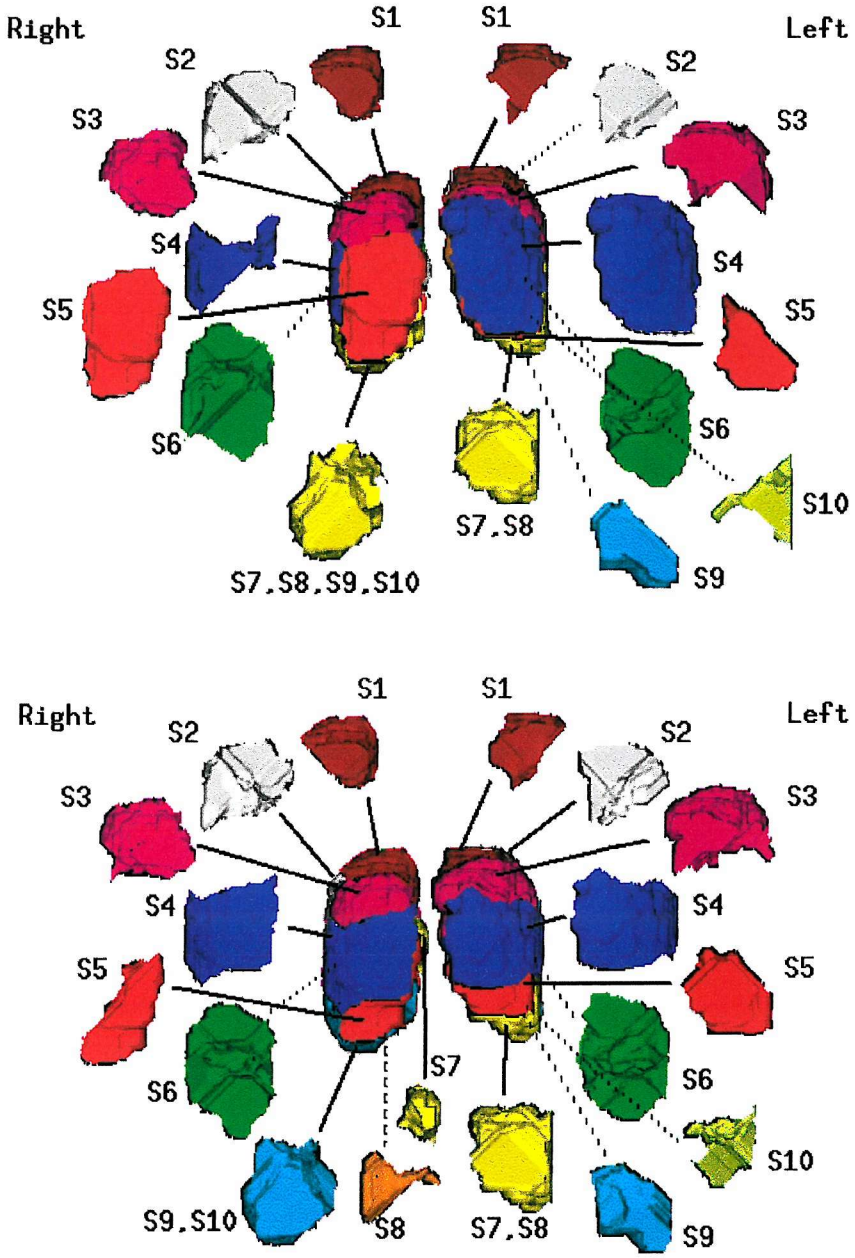

Figure 6-13: Modelled segments using the cast images. The growing process was applied to the segmental bronchi and was limited by the lobe contours. (Top) using the airways in the first 6 generations. (Bottom) using the airways in the first 9 generations. Their size and shape can be compared with the segments in the cast photographs formed by the airways of corresponding colour (Fig. 6-4).

Table 6.3: Air volume (ml) per generation and per shell in the volunteer's Right Lung.

Generation	Shell number										Total
number	1	2	3	4	5	6	7	8	9	10	
1	0	0	0	0	0	0	0	0	0	0	0
2	0.14	0.05	*	*	*	*	*	*	*	*	0.23
3	0.62	0.98	0.36	*	0	0	0	0	0	0	1.96
4	0	0.19	0.49	0.06	0	0	0	0	0	0	0.74
5	0	0.15	0.87	0.39	0	0	0	0	0	0	1.42
6	0	0	0.32	0.75	0.32	*	0	0	0	0	1.40

* < 0.05 ml

6.3.4 Air Volume Matrix

A slice in the image volume from which the air volume matrix was formed is shown in Figure 6-14. The air volume matrix, displayed in Table 6.3, contains the air volume in the volunteer's right lung in generation 1 to 6 per shell. The fact that generation 2 airways spread over several shells is due to the distance around the hilum to the edge of the lung that can be very short, but still separated in ten shells. A different location of the hilum position H (shift of two slices in transverse and coronal directions) slightly affected the number of voxels of generation 2 and 3 in each shell but not the general spread of the generations.

The space volume in the volunteer's right lung was 2120 ml. Using the density data per shell derived from another subject (Table 1 in Fleming et al. (1995)), the portion of air in this volume was estimated to 1448 ml. The resulting scaling factor applied to the conceptual shell-generation model matrix for comparison given in Fleming et al. (1995), normalised to an air volume of 1376 ml to be comparable with the volunteer's was thus 1.053. Figure 6-15 shows a difference in the spread of the generations over the shells as well as a general shift of the data. The conceptual matrix overestimated the air volume in generation 2 within the lung by a factor 10. Over the next four generations, the air volume in the conceptual shell-generation model was 30% less than in Table 6.3. In both matrices, the air volume in generation 4, relative to the other generations, is somewhat smaller.

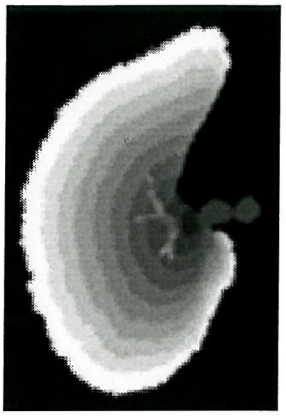

Figure 6-14: Formation of the air volume matrix. The volunteer's lung outlines were divided into shells on which the airway generation model (Fig. 6-8) was overlaid. This transverse slice was cut through the resulting image volume at the level of the hilum location. It shows the division into 10 shells and the relative position of the main bronchi and the further generations in the right lung.

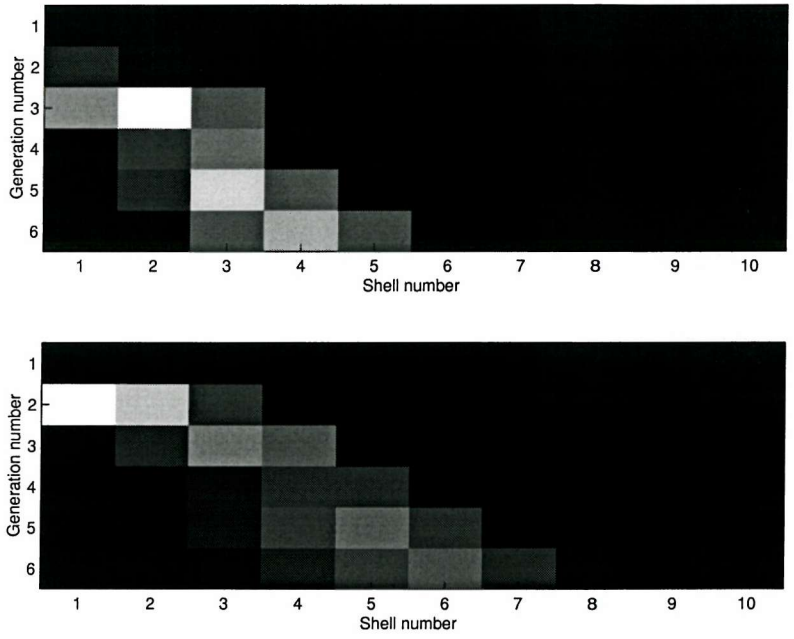

Figure 6-15: Representations on a gray scale of the air volume matrix contents in the first six generations. (Top) Volunteer's matrix (Tab. 6.3). (Bottom) Matrix of the conceptual shell-generation model [Fleming et al. (1995)] scaled to the volunteer's lung size (scaling factor = 1.053). The grey intensity is proportional to the air volume that each component contains, normalised to the maximum value (1.14 ml).

6.4 Discussion

The aim of this chapter was to realistically model anatomical features of the lungs in 3D, that would help aerosol deposition studies performed on a subject to be interpreted in relation to the same person's anatomy. The modelling methods developed in this chapter and some of their applications are now discussed.

6.4.1 On The Modelling Methods

The method developed to model the airways and airway generations builds on the algorithm described in Chapter 4. It does not require further intervention from the operator, other than selecting the image files. Figure 6-8 clearly shows the realistic character of the models: they replicate the original CT images, and code them by airway or airway generation. Such an automated description is new. The number of airways included in the resulting models is limited by the X-ray dose and the CT resolution, not by the modelling method itself.

The method developed to model the lobes and segments is based on a region growing process that uses the 3D airway anatomy and the 3D lung boundaries. Its validation must be done by comparison with the shape, size and location of the true corresponding features. The latter, for the lobes, can only be obtained by segmenting the fissures from CT images, which allow for the true lobes to be defined. Such comparison was successfully done with the lobar model using the volunteer's images (Fig. 6-9 and 6-10 and Table 6.1). This was done as a first assessment of the realism of the modelling method before trying modelling the segments. The computed lobar model was encouraging. Unfortunately, the segments, because they do not have any solid/material frontier, such as pleural tissue, to partition them and that can be segmented out, can only be defined following *ex vivo* examinations. In practice, radiologists or pulmonologists would manually estimate the location of the segmental borders on *in vivo* images based on the bronchial anatomy (identification of the segmental bronchi B^i) and on the knowledge of the segment empirical shape (see Section 2.4.1). Thus the actual drawing of a frontier line between two segments cannot be accurately drawn. The comparison of the location and shape of the segments modelled using the volunteer's images with the radiologist guidelines (e.g. Thompson et al. (1999)) shows both agreements and disagreements. Nevertheless these guidelines warn several times about the considerable anatomical variation that exists between individuals. Comparison of the volunteer's lobar structure with other observations and models (Tab. 6.1) also

highlights it. So do the differences between the volunteer's segmental model and the 3D atlas (Tab. 6.2), without however validating it.

The use of the cast airway data allowed further investigation of the method, although the lung outlines are artificial (but sensible in their overall size and shape), by comparing the lobar and segmental models with the features visible on the solid cast. Again, the location of the computed lobar fissures seems very reasonable (Fig. 6-11). The level of detail and accuracy generated by the method was shown to be related to the number of generations taken into account in the region growing process. Using six generations restricted the partition of the right lower lobe into two segments instead of five because not all the segmental bronchi could be identified in so few generations. The segments in the other lobes were found to be generally closer to their appearance on the solid cast when using nine generations (Fig. 6-13). Still, it was shown that this was not sufficient to create exactly their true shapes and sizes as sudden orientation changes in higher airway generations may also occur. On the basis of this result, no confidence can be truly placed on the volunteer's segmental model. Lobes, that are bigger structures were well modelled using only the first six generations of the volunteer's data. This is however to be taken with caution as the observation concerns only one set of *in vivo* data. Similar observations on further data sets would be more conclusive.

The region growing process can be understood as a "fight for space", and is therefore similar to the way the air space in the lung was originally developed [Boyden (1971)]. The more airways that are used in the procedure, the more confidence can be placed on the resulting lung partition. From the above study, it is felt that the method is a promising approach to realistic modelling of segments and is worth further investigation, in particular on the importance of geometrical factors such as the bifurcation plane rotation angles following segmental bronchi. The method requires the identification of the segmental bronchi as a radiologist would do before, painstakingly, manually estimating and drawing, in each slice of the lung volume, the segmental contours. On the latter operation, the computed method is much quicker. It took 17 minutes to model the volunteer's segments from 6 generations, needing 150 iterations to assign a segment number to all the voxels within the lung outlines contained in a 512x512x340 volume image on a Sun Sparc Ultra 5 (330 MHz CPU, 2 MB cache). The reproducibility of the results is also an argument in favour of the computed method as it is unlikely that different radiologists draw exactly the same contours on the same lung images. Actually, it

would be quite informative to see how the volunteer's computed segmental model compares with what a dozen of radiologists would independently draw from the same data.

It has been seen in the previous chapters that it would be of great interest to have image data on the whole airway tree. In particular, the modelling of the airway tree per airway or airway generation, would provide a full representation of the air volumes in the lungs and could be used to study intersubject variability (see also Section 6.4.2). It would also bring a great confidence in the shape of the segments reconstructed using the above growing region process on the segmental bronchi and all their daughter airways.

Attempts to fill in the lung space with conical or hemispherical volumes growing at the extremities of the modelled airways could be done, where voxels in volumes would be a mixture of air and tissue, whereas voxels outside would represent only tissue. However, this is unlikely to be successful as their orientation in the space and non uniform values of air density could not be justified with the few previous experimental or theoretical work published in the literature. Alternatively, the very recent work done by Kitaoka et al. (1999) and Suki et al. (1999) appears promising as they propose a 3D model of the airway tree down to terminal bronchioles, based on fluid dynamic properties (see Section 2.7.1, p. 43). The 3D model was originally intended for studying the structure-function relationship in the lung, especially for gas issues (lung mechanics and gas exchange in normal and constricted airways, ventilation distribution). Assessment of the 3D realism of the distribution of the complete airway tree that Kitaoka's algorithm creates is first required. The method developed in this chapter to model the lobes is suggested as a means for such assessment: the lobar shapes modelled using the volunteer's lung outlines and the 3D anatomy of his central airways described in Section 5.3 could be compared with the ones segmented out manually by the clinician. Another suggestion is the use of the tabulated morphological and topological data set of Kitaoka's model, once verified as above, for aerosol deposition modelling.

Improvements of ^{3}He-MR imaging technology are also of great promise as it has been shown that it is possible to visualise the airways down to the acini in the rat [Johnson et al. (1998)]. It has the potential to eventually provide similar data *in vivo* in humans. The time required to image the whole human lung, because of its size, is however different and currently too long to allow clear imaging of

small airways without Brownian motion of Helium gas blurring artifacts (Tastevin-Sauret communication).

Finally, concerning the modelling the segments, the same method developed in this chapter could be investigated on the base of the identification of the pulmonary arteries rather than on the base of some knowledge of the airway tree. This is due to the fact that the pulmonary arteries are also organised in the lungs in a tree-like structure, which follows very closely the airway tree (e.g. Fig. 6-16). One way of imaging these blood vessels would be with conventional MR (H^+-MR), using a "time-of-flight" protocol, which is a well-known technique for blood vessels imaging [Rinck (1993)]. Consecutive transverse slicing of the thorax would be needed for this application. This procedure is technically possible, although unusual in "time-of-flight" protocols, which are mainly used to assess the behaviour of a vessel over time. Typically, the same transverse slice is scanned at various times of the cardiac cycle and variations in size of the main blood suppliers (principally ascending and descending aorta) are analysed over time. The advantages of this change in the lobe and segment modelling would be the following. MR is firstly a radiation-free technique, unlike CT protocols. Secondly, blood vessels appear bright on dark background in time-of-flight images, unlike in T1-weighted MR images where they appear black with bright walls. The images can be gated for heart and breathing movements. This would not require any breath-hold during the examination, which can be difficult for subjects with diseased lungs. Segmentation of the pulmonary vessels would thus appear, at first sight, easier than the segmentation of the airways that are not visible with conventional MR or difficult to automatically segment out from their background in CT scans. A primarily pilot study would be of value to assess the level of difficulty in differentiating the pulmonary arteries from the neighbouring blood supplies. An example of the visualisation of the pulmonary arteries is given in Figure 6-17.

6.4.2 On The Use Of The 3D Anatomical Models

The 3D anatomical models currently available for the interpretation of 3D aerosol deposition data in relation to anatomical features are the conceptual shell-generation model and segmental atlases. The former model derives the aerosol deposition per generation using a "theoretical" air volume distribution in the subject's lung images. The latter contain the "standard" or "average" position and shape of the lobes and segments in the lungs. The outlines are fitted to the subject's own lung,

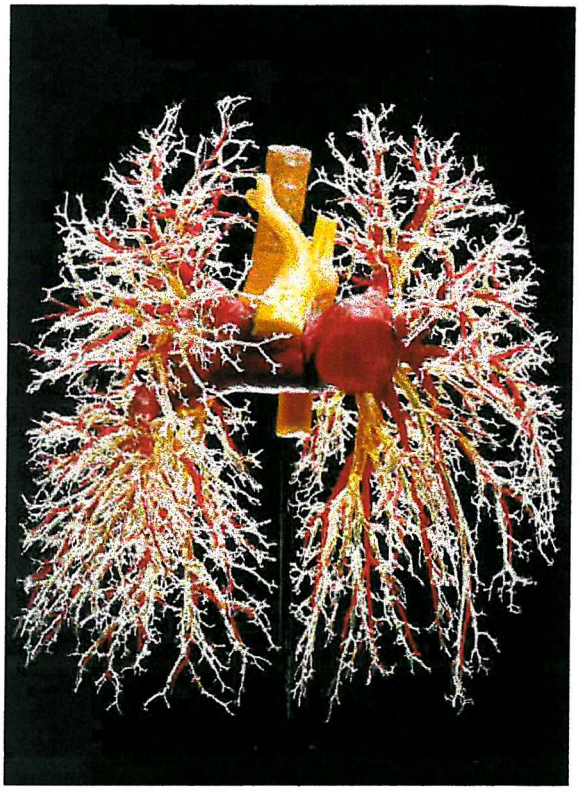

Figure 6-16: Photograph of a human cast showing the airway tree (light yellow) and pulmonary arterial tree (red). The pulmonary tree follows remarkably well the airway tree. The yellow structure is the aortic arch. Note: the pulmonary artery entering the heart is abnormally dilated (congenital heart disease).

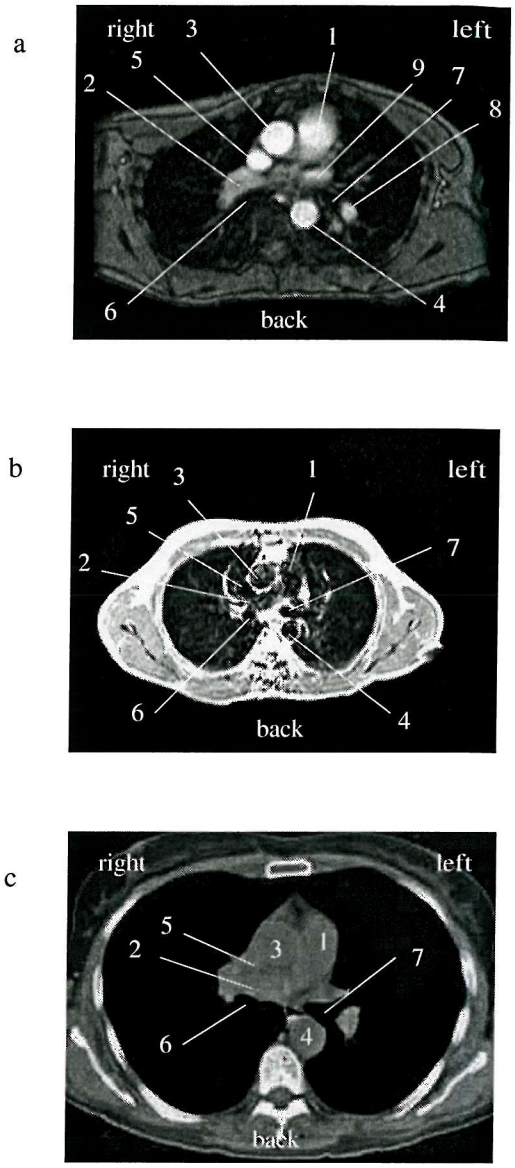

Figure 6-17: (a) Transverse time-of-flight MR image. The blood vessels are visible, whereas the airways are black. At this particular time of the cardiac cycle the ascending and descending aorta appear brighter. (b) Transverse T1-weighted MR image. The airways and blood vessels appear black. (c) Transverse CT image. The grey scale has been set such that the pulmonary arteries, ascending and descending aorta are visible, although cannot be differentiated. Note: these images have not been performed on the same patient, same position in the thorax or slice thickness. *Legend*: 1 pulmonary trunk, 2 right pulmonary artery, 3 ascending aorta, 4 descending aorta, 5 superior vena cava, 6 right bronchus, 7 left main bronchus, 8 left basal pulmonary artery, 9 superior pulmonary vein.

using for instance a radial transformation (see Section 7.2.4). Thus, both methods assume the subject to be a "theoretical" or an "averaged" subject. The first method does not take into account variations that occur in the size and location of the airways between individuals, which it is well-known. The latter was also illustrated in the results of Chapter 5, although only on the basis of two data sets and a few previous published data. The second method assumes that the relative lobar and segmental sizes are the same in any lung. If this were the case, such differences between previous models (e.g. Tab. 6.1, columns 5 and 6) and also between the volunteer's lobar and segmental models and the previous models and atlas (Tab. 6.1 and 6.2) would not be observed.

When interpreting a radionuclide aerosol deposition study, the current anatomical models thus cannot be expected to relate the aerosol deposition in relation to the subject's own anatomical features. The difference between the assessed deposition and what is truly deposited in the individual's generation or lobe or segment will depend on how closely the individual fits the anatomical model. Unfortunately this is a difficult estimate to make: intersubject variability has been very often observed but not well characterised. The current models are useful to get an average pattern or intersubject variability information relative to the drawn region (region of interest) over a targeted population, not to the individual's anatomy itself. Similarly, the models created from the volunteer's anatomical images do not seem suitable to assess deposition in other subjects' airways. Regarding diseased lungs, the individual anatomy is unlikely to match a standard or average shape or size of a feature, thus underlining the need of creating anatomical models from each individual.

The modelling methods presented in this chapter were developed having in mind the assessment of the distribution of aerosol deposition in relation to lung anatomical features. By overlaying them on 3D radionuclide aerosol deposition studies, one can interrogate the aerosol data in each airway, in each airway generation and in each shell as well as in each lobe and each segment. It is evident that the resulting models represent a unique individual as these have been built to be a 3D mimic of the subject's anatomical features (the volunteer's segmental model could not be validated). As suggested above, it is these volunteer's anatomical maps that should be used to interpret the volunteer's own aerosol deposition profile. By overlaying the volunteer's anatomy models onto the volunteer's own activity map, a detailed determination of aerosol deposition may be made (see Chapter 7).

The identification of the location of the air volume in each generation of the volunteer's airway tree was an opportunity to investigate the realism of the conceptual shell-generation air volume matrix [Fleming et al. (1995)]. The repartition of the volunteer's airway generation in relation to his lung outlines was expressed using a so-called air volume matrix. This 2D representation is a way to visualise the air distribution information with respect to the depth of the 3D lung volume, partitioned into "shells" (Tab. 6.3). Since the latter can be considered as a "true" representation of the air volume, it provided valuable data to assess, for the first time using *in vivo* data, the extent to which the conceptual shell-generation model air volume matrix [Fleming et al. (1995)] is realistic.

Scaling of the conceptual model was necessary to compare the air distribution relative to the same air volume. In practice, the volunteer's total air volume would be evaluated from measurements of air density per shell in the subject's own CT or transmission scan [Fleming et al. (1996a), Lee et al. (1999a)]. In this study, the CT scan did not cover the whole lung, thus density information in all the shells is not available. Use of the empirical value of 0.7 air in the lung would have given a scaling factor of 1.078, thus very close to the scaling factor calculated using the shell air density values from an other subject [Fleming et al. (1995)]. Although air volume in the first six generations represents a very tiny fraction of the total air volume (less than 1%), there is sufficient information to show the shift in the spread of the generations across the shells (Fig. 6-15). This is a consequence of the conceptual assumption of a larger portion (two thirds) of the main bronchi inside the lungs. Their contribution to the matrix is actually very small since only the extremity of the main bronchi actually enters the lungs. Correction of this error in the case of the volunteer's images would bring the spread of the conceptual matrix relatively well in line with the true description. This is pleasing since the conceptual model is based on Weibel model A, itself drawn from the diameter and length relationship with generation number described in Equation 2.2 (p. 31) and with which the volunteer's data were shown earlier to comply relatively well (Fig. 5-3). On the other hand, in higher generations, the conceptual shell-generation matrix may not agree anymore with the *in vivo* matrix as it assumed a radial distribution of the airways from the hilum. Such assumption prevents the recursion of the airway back from an outer to an inner location in the lung, which undoubtedly occurs in the true 3D bronchial anatomy as soon as generation 8 or 9 (e.g. Fig. 6-4, Fig. 6-16, Fig. 5-7) and in the acinar anatomy. The present comparison of the two matrices is thus limited by the small number

of airway generations (six) included in the volunteer's air volume matrix. (The cast data contains a few more generations (nine) but it is not strictly correct to calculate a shell-generation matrix from it as the lung outlines are artificial, rather than the original ones and may bring bias in the comparison). Again, this shows that imaging the airway tree further down would be useful as it would allow a more complete comparison. Knowledge of the distribution of the acini would also be valuable as they represent the major portion of the pulmonary air volume (see Section 2.6.2, p. 39). In future comparisons, intersubject variability should somehow be taken in account and the clinical significance of the differences shown when interpreting radionuclide images may be the subject of further study.

Finally, the fact that the models developed in this chapter using both the cast and volunteer's CT data, in terms of airway and airway generation (Fig. 6-8), are digitised (voxel-data) and mimic the human anatomy in terms of size, orientation and shape, is of value for flow simulations studies in the airways. In particular, studies of flow profiles and properties are increasingly done via Computational Fluid Dynamics (CFD) packages. These use computer-models in which the behaviour of air or liquid can be simulated and visualised; medical applications of CFD include the influence of the shape and size of airways and bifurcations on the flow characteristics. The airways are generally modelled by cylinders, straight or bent; bifurcations are generally modelled by the interconnection of three cylinders, in a planar or non-planar geometry. Because of the lack of information on the 3D position of the airways in the literature, these models are not realistic. It is therefore suggested to use the above models to study the flow profiles in several generations. Results could also be compared with results obtained from *in vitro* experiments in glass models (e.g. Chang and Menon (1993)). Differences in the flow, due to the non-planarity of the bifurcation (Fig. 5-13) are expected (see Section 5.4, p. 108). Moreover, the smoothness of the bifurcations that is seen in reality is ignored in 3D modelling. This may have an influence in the results of flow simulations, when investigating, for instance, particle deposition at a bifurcation ridge. An interesting study would be to use the models based on the volunteer's data to study air flow in the tracheal bifurcation that has long been the object of various theoretical studies (e.g. Owen (1969)). Investigation of aerosol deposition for instance at the carinal ridge is also suggested: validation of the CFD simulations could include the experimental data published in the literature (e.g. Martonen (1983)).

6.5 Conclusion

The methods used to create realistic 3D models of three anatomical pulmonary features have been put in place using medical imaging and tested on these of the volunteer and the cast. The modelling of the airways reconstructs the volume image of the airway tree using the diameter and orientation of each airway tabulated in Chapter 4 and colour-code each airway with a unique colour, or with its generation or lobe number; it is automated. The resulting models are clearly 3D realistic. The modelling of the segments is based on the above airway model and an automated region growing process which requires the volume image of the lung outlines. Identification of the segmental bronchi by the operator is also necessary. Validation of the resulting segmental model cannot be done with the imaging techniques currently available; the realism of the volunteer's lobar model obtained with the same method and assessed by comparison with the fissure segmentation from his own CT images, is encouraging. The more airway generations are taken into account in the modelling method, the more confidence can be placed in the realism of the model, this especially for the segmental shapes. In the future ^{3}He-MR imaging will provide more data on the airway tree. Investigation of the same method, based on images of the pulmonary arterial tree, using x-ray dose free MR imaging, appears worthwhile.

The existence of anatomical intersubject variability was, again, shown. The fact that the models in this chapter are a representation of one particular subject is therefore an asset for assessing aerosol deposition in relation to the subject's anatomy. In the next chapter the use of volunteer's airway and lobar models overlaid on an aerosol SPECT study carried out on the same subject, is thus considered to directly assess the deposition per airway, per generation or per lobe. For air flow and particle deposition studies using CFD, as well as for aerosol deposition modelling, the 3D realism of the volunteer's and cast models is also shown to be of value. A very limited assessment of the realism in the conceptual shell-generation air volume matrix was carried out.

Chapter 7

Assessment of an *in vivo* aerosol deposition study

7.1 Introduction

The subject for whom the anatomical models in the previous chapter have been developed, had also undergone two aerosol deposition SPECT examinations as part of a previous study at Southampton General Hospital [Conway (1996)]. In that study, the aerosol deposition was assessed in each of the ten shells, centred on the hilum, that can be drawn to partition the lungs. Using these same SPECT data, the aim of this chapter was to create pilot data on aerosol deposition with respect to the subject's anatomy.

The methods leading to the assessment of the aerosol deposition in the models defined in the previous chapter, containing the volunteer's lobes and airways, are described. The confidence in these results is first examined. The value of interpreting aerosol data in relation to the subject's own activity and the use of such interpretation to compare and/or validate deposition distribution obtained using alternative methods, are then discussed. Re-assessment of the SPECT aerosol deposition in the lungs partitioned into ten shells is also proposed for estimating the influence of the user-defined location of the hilum on the deposition results.

7.2 Methods

7.2.1 SPECT Study

Two SPECT studies, A and B, had been carried out in 1995, on different days, with the same volunteer on whom a CT scan (see Chapter 5) and an MR scan (see Chapter 6) were performed. In the four years between the SPECT and the CT study, the volunteer had not changed either weight, size or diet (non smoker) and had not had any record of respiratory or chest problem or serious infection, that may have altered his airways and lung size.

The scanning procedure, in which the author was not involved, was the following. The volunteer inhaled HSA (human serum albumin powder in saline) labelled with ^{99m}Tc from a nebuliser device (Optimist, Medic-Aid Ltd, U.K.), in an upright position, following a controlled tidal breathing pattern. The mean inspiratory volume was 928.2 ml and the inspiratory flow was 22.6 l/min. The particle-size distribution from the nebuliser was measured using an *in vitro* laser diffraction method (Malvern Instruments HLS 2600 Particle and Droplet Sizer, Malvern Instruments, U.K.). The mass median diameter was found to be 1.8 μm (fine particles) and the geometric standard deviation 1.5. Immediately after inhalation, the SPECT scan was performed with the subject lying down horizontally. The study took about 15 minutes. Landmarks filled with ^{99m}Tc and placed on the volunteer's sternum, xiphoid and on the right nipple were included in the image. The map to correct for tissue attenuation was created by manual segmentation of the bone, tissue and air spaces in the MR scan described above (see section 6.2.3). Scatter was corrected for but blurring of the images, also called partial volume effect, due to SPECT poor resolution, was not. The final image volume contained 48 slices and the voxel size was 4.7 mm x 4.7 mm x 4.7 mm. It did not contain the mouth and stomach regions which may have contained some activity.

The examination was part of an aerosol deposition reproducibility study supervised by Dr. John Fleming at Southampton General Hospital. Assessing the SPECT images using the shell model and including eleven other subjects, it showed that the aerosol deposition with the device used was reproducible [Conway (1996)].

7.2.2 Anatomy

The volunteer's lobar model, the lobes identified from the manual segmentation of the fissures in the volunteer's CT images and the volunteer's airway model

expressed in terms of generations, were used. They are shown in Figures 6-9, 6-10 and 6-8, respectively. These models were shown in Chapter 6 to realistically present the volunteer's corresponding anatomical features.

7.2.3 Multi-Modality Image Registration

The SPECT images were re-sized and re-oriented to match the voxel size and orientation of the anatomical images. This registration was done in two stages. First, the SPECT images were registered with the original MR scan. This transformation was based on the least-squares fitting of paired 3D coordinates [Arun et al. (1987)]. It was implemented by Mr. Peter Halson in a stand-alone program which required the 3D coordinates of the sternum, xiphoid and right nipple markers on each image modality. The output was the transformation matrix to apply to the SPECT image volume. Secondly, the transformed SPECT volumes were re-sampled to match the CT voxel size. On these images, the same translations and rotations that were applied to the MR images earlier (see Section 6.2.3) were performed to align the SPECT and CT images using the imaging package threeD (Fig. 6-5).

7.2.4 Aerosol Deposition Assessment

Measurements

The number of counts in the SPECT studies A and B located within the anatomical contours and the total activity in the whole image were measured. The activity assessment in the anatomical features of interest was done by overlaying the anatomical and activity maps and then interrogating the SPECT data A and B in the region of interest. The aerosol deposition was expressed as a percentage of the total activity within the lung contours $\left(\frac{\text{counts in ROI x 100}}{\text{total lung counts}}\right)$. The activity per unit volume in the region of interest was calculated by dividing the latter by the percentage of total lung space volume that the region of interest represented.

Comparison With A Lobar Atlas

Comparison of the aerosol deposition distribution in relation to the anatomy using the subject's own anatomy or using a more global model was sought for. This was in order to estimate the importance of a realistic anatomical model in SPECT interpretation. Such comparison was done on the basis of the lobar deposition.

The 3D segmental atlas developed in-house (Fig. 2-3 and Tab. 6.2) was fitted to the volunteer's lung by radially transforming the atlas lobes and outlines. In this process, the distance from the point M to each point A of the subject's lung was calculated as a fraction of the total distance from M to the edge of the lung in the direction (MA). M was defined in the coronal slice containing the hilum H of the right/left lung, as the mid-point of the horizontal segment $[HE]$ joining H to the edge of the right/left lung. The lobe value of the voxel A' located in the 3D atlas volume at this same fraction from the atlas point M' and in the direction (MA) was given to A, M' being defined in a similar way as M. At the end of this fitting, if a point A had not been assigned to a lobe, the lobe assigned to most of the 6-connected neighbour voxels was given to A. The latter process was required for only 0.5% of the points A. When overlaying on the SPECT images, the aerosol deposition was calculated as above. For each lobe, the ROI covered the volume of all its corresponding segments.

Positioning Of The Hilum For Shell Analysis

The aerosol deposition in the SPECT studies had previously been assessed by partitioning the lungs into ten shells. The activity in each shell was then calculated as in Section 7.2.4, the ROI covering the volume of a shell. Each shell was centred on the hilum that had been manually defined by the operator (who was not the author) (see Fig. 6-7).

In order to estimate the influence of the location of the hilum on the deposition results, the aerosol deposition in each shell was re-assessed in this study; the position of the hilum was assigned by the author. The partitioning of the lung volume into ten shells was done in the previous chapter, in Section 6.2.5. Figure 6-14 shows a transverse view of the "anatomical map" that was thus overlaid on the activity map. Calculation of the deposition per shell was done as above, the ROI covering the volume of a shell. The conversion of the deposition per shell to deposition per generation using the shell-generation air volume matrix was not done as the latter has not been validated.

7.3 Results

7.3.1 Lobar Deposition

The number of counts within the anatomical lung contours was underestimated by respectively 23.1% and 22.1% in the SPECT studies A and B since only respectively 76.9% and 77.9% of the counts were located inside these contours. Such a blurring of the image is common in nuclear medicine images (see Discussion below). It is worth noting that simulation work undertaken by Dr. Fleming showed that the number of counts, in each lobe, is underestimated by approximately 20% (unpublished results). Thus, by normalising the lobar activity to the total activity deposited within the anatomical lung contours, the influence of this effect is greatly reduced. The activities per unit volume in both right and left lower lobes are higher than in the other lobes for each SPECT study. Tables 7.1 and 7.2 present these results, assessed in each modelled lobe. They concur remarkably well with Table 7.3 showing the assessment of aerosol deposition in the lobes defined manually from the volunteer's CT images (Fig. 6-10).

In-house atlas lobar deposition also shows similar patterns in the activity per unit volume although the difference between each lobe is less marked (Tab. 7.1 and 7.2).

7.3.2 Deposition Per Airway Generation

The aerosol deposition in the first six airway generations is presented in Table 7.4 for both SPECT studies. It is a very tiny fraction of the total activity within the lung outlines. The concentration in the very central airways shows a lower than average aerosol deposition, which seems reasonable since the inhaled particles were very fine. Also, the ratio surface area-to-volume in the airways increases with the generation number so to a certain extent, the further down the lungs, there may be more deposition on the airway walls. However, none of these hypotheses can be confirmed as the counts within the airways may be significantly affected by the limited resolution of SPECT imaging in their ability to accurately reflect the activity in individual airways.

7.3.3 Deposition Per Shell

In the right lung, the percentage of total activity in each shell was calculated for each SPECT study. No difference in these results was shown compared with the

Table 7.1: Assessment of lobar aerosol deposition in the SPECT study A.

Lobe	Modelled* lobes		Fitted in-house lobar atlas**	
	% total activity	$\frac{\%\text{ total activity}}{\%\text{ lungs anatomy}}$	% total activity	$\frac{\%\text{ total activity}}{\%\text{ lungs anatomy}}$
RU	17.46	0.97	13.12	0.97
RM	5.53	0.77	4.82	0.85
RL	28.28	1.06	33.06	1.02
LU	24.75	0.93	16.05	0.92
LL	23.82	1.11	32.50	1.06

* Figure 6-9

** In-house segmental model (Fig. 2-3a), in terms of lobes

Table 7.2: Assessment of lobar aerosol deposition in the SPECT study B.

Lobe	Modelled* lobes		Fitted in-house lobar atlas**	
	% total activity	$\frac{\%\text{ total activity}}{\%\text{ lungs anatomy}}$	% total activity	$\frac{\%\text{ total activity}}{\%\text{ lungs anatomy}}$
RU	17.87	1.00	13.31	0.99
RM	6.52	0.82	5.65	0.99
RL	28.10	1.06	33.19	1.03
LU	22.50	0.85	14.48	0.83
LL	24.71	1.16	32.76	1.07

* Figure 6-9

** In-house segmental model (Fig. 2-3a), in terms of lobes

Table 7.3: Assessment of aerosol deposition in the lobes defined manually from the volunteer's CT images (Fig. 6-10).

Lobe	% total activity		$\frac{\%\text{ total activity}}{\%\text{ lungs anatomy}}$	
	study A	study B	study A	study B
RU	17.00	17.40	0.97	1.00
RM	6.14	7.11	0.82	0.95
RL	28.13	27.99	1.05	1.05
LU	24.74	22.62	0.93	0.85
LL	23.83	24.60	1.11	1.15

Table 7.4: Aerosol deposition in the first six generations.

Generation	% total activity		% total activity / % lungs anatomy	
	study A	study B	study A	study B
1	*	*	0.32	0.69
2	0.10	0.15	0.52	0.82
3	0.06	0.11	0.75	1.29
4	0.05	0.07	0.92	1.16
5	0.05	0.07	0.90	1.09
6	0.10	0.12	1.10	1.28

* Only part of the trachea

1995 study, where the location of the hilum was determined by a different operator (t-tests on the mean of the difference, 9 degrees of freedom, t=0.81 for studies A and B, p>0.05). The activity per unit volume in each shell was also calculated. The partial volume effect in each shell was corrected using the iterative correction method developed in Fleming et al. (2000b) using simulated images (Fig. 7-1).

7.4 Discussion

Quantification of SPECT images by direct interrogation of the SPECT activity map with respect to the anatomical boundary (anatomy map) is difficult because of the poor resolution of the images: for SPECT imaging of the lungs it is of the order of 15 mm. Such resolution results in the partial volume effect in which some of the counts due to activity at a particular point in the body are spread out over several voxels on the image (blurring effect). Simulation showed that this affects the interpretation of the volunteer's SPECT images in terms of deposition per lobe to a similar extent in each lobe. In calculating deposition per shell, cross-talk between shells is important particularly in the peripheral shells and can be corrected (Fig. 7-1, solid lines). Clearly, because of the size of the airways compared to the SPECT resolution, the validity of the deposition in each airway without taking the partial volume effect into account (Tab. 7.4) is very limited. Simulation may be a way to correct these results. Further image processing using different reconstruction techniques, such as Maximum Likelihood Expectation Maximisation, MLEM (e.g. Beekman (1995)) may also overcome this problem. A higher resolution on the visualisation of the aerosol deposition would also be desirable, and this can be achieved with positron emission tomography, PET [Webb (1988)].

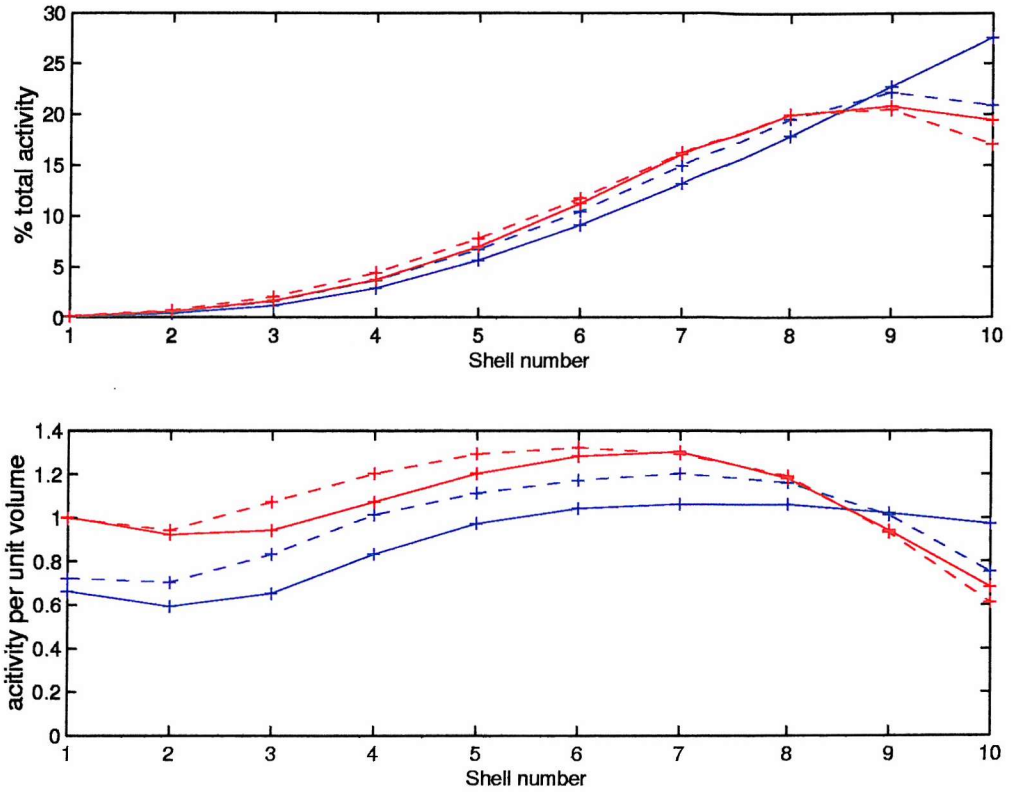

Figure 7-1: Aerosol deposition per shell in the volunteer's right lung. (Top) Percentage of total activity within the lung outlines in each shell, calculated as $\left(\frac{\text{shell counts x 100}}{\text{total right lung counts}}\right)$. (Bottom) Activity per unit volume, calculated as $\left(\frac{\text{\% total activity}}{\text{\% right lung anatomy}}\right)$. *Legend:* The blue and red lines refer to the SPECT studies A and B, respectively. The dashed and solid lines are the data uncorrected and corrected for the partial volume effect [Fleming et al. (2000b)], respectively.

Tables 7.1, 7.2 and 7.3 show that the aerosol particles inhaled by the volunteer did not deposit uniformly in all lobes. In fact, a lobar vertical gradient in the aerosol deposition was observed, the deposition per unit volume increasing from upper to lower lobes. The proportion of air and tissue in each unit volume (one voxel) is unknown in our study but there is evidence that alveolar volumes are greater in the upper than in the lower portions (e.g. Milic-Emili et al. (1966)), because of the lungs own weight (gravity effect). Therefore, in terms of deposition per air volume, this gradient would be more pronounced.

Similar lobar deposition and gradient were observed in both SPECT studies, strengthening our confidence in the measurements. Moreover, the similarity of the results in Tables 7.1 and 7.2 by comparison with the corresponding data in Table 7.3, which may be considered as the "gold-standard" for these measurements, emphasises the 3D reality of the lobar models created in Chapter 6. The percentage of activity in the SPECT images assessed using the lobes defined by the 3D in-house atlas fitted to the volunteer's lung shape, is quite different from that using our model, although a concentration gradient in the same direction was still observed. The fact that it is less marked, particularly in the left lung, may show the advantage of using a model that describes the volunteer's lobes, rather than approximated ones (see Section 6.4.2, p. 140). Furthermore, a larger difference would be expected in the case of 3D aerosol deposition studies showing inhomogeneous depositions throughout the lungs. This may occur in diseased or obstructed lungs, or using larger particles. Such distributions were not observed in the slice by slice analysis or volume rendering of the SPECT studies A and B. Further experiments are needed to confirm this. It would also be interesting to know the extent to which the location of the lobes and segments vary between subjects to investigate if the low resolution of SPECT can "mask" the differences. Alternatively, it would be valuable to simulate SPECT images from a known deposition distribution in lobes and segments of various size and shape. The errors in the lobar and segmental deposition concentration measured on the SPECT images using the original anatomical map or using a fitted standard model could be estimated.

The presence of such a gradient in the SPECT studies is in line with previous observations. For instance, Baskin et al. (1990) used aerosolised pentamidine radiolabelled with ^{99m}Tc-DTPA and ^{99m}Tc-HSA (unknown particle size distribution) with a slow and deep inspiration and measured the gradient on planar images. The

deposition measurements were related to air volume by using a planar equilibrium ^{133}Xenon ventilation scan (see below) and a vertical deposition increase per air volume from apex to base was noticed. A similar experiment, extended to 3D, is suggested here as an addition to our protocol, if deposition data per air volume are required. Division of the counts in each voxel of the original aerosol deposition scan by the counts in the corresponding voxel in a ventilation scan performed on the same volunteer is thus proposed. This additional scan can be achieved with an equilibrium ^{133}Xenon or ^{81}Krypton SPECT study, that images the air distribution in the lungs (poor resolution). The resulting image volume, labelled D/AV would thus represent the aerosol deposition (D) normalised for air volumes (AV). The additional study would not be difficult as both gases are used routinely in Nuclear Medicine departments for planar ventilation examinations. Because of the energy of ^{133}Xe and ^{81}Kr, the ventilation scan would have to respectively precede / follow the aerosol study. It would however increase the radiation dose to the subject.

It is the first time that quantification of a lobar gradient is presented. The role of the lobes in the gradient observed in planar imaging could not be assessed because the lobes overlap. Preferential deposition in the posterior base of the lungs had been observed in SPECT studies, after inhalation of aerosols in upright position of diameters ranging from 1.5 to 7 μm [Conway (1996)]. Still, the role of the lobes could not be assessed. The definition of the subject's lobar anatomy has not been the object of investigation yet, for applications to aerosol deposition distribution interpretation. In our opinion, this is primarily due to (1) the rather recent use of 3D multi-modality imaging and (2) the difficulty of applying a "global" model to any subject, given the anatomical variability related (but not quantified) in the literature. Intersubject variability was shown in Sections 3.3.3 and 3.4.3 to limit the assessment of aerosol deposition images and the validation of anatomical and prediction models. In this study, the influence of this variability was removed.

Similar quantification involving more subjects would be valuable for several applications. Firstly, it would provide details on the variations in the sites of deposition within the lungs, which is interesting for delivering a drug to specific areas, and also between subjects. A priori, segmental anatomical models, if built to mimic each subject (see Chapter 6), would also give more detailed deposition distribution; this is if the partial volume effect and low resolution are not limiting the image interpretation. This would also lead to a better understanding of the aerosol deposition in the lungs. Lastly, no data, to date, are available in

the literature to validate lobar deposition prediction models, although they are required for validating the predictions of aerosol deposition computer-models that provide this information. In particular, Yeh and Schum (1980) and Gerrity et al. (1981) have both predicted a vertical lobar deposition gradient, however in opposite directions. Quantified data may thus be included in validation studies of their computer-model by matching the aerosol characteristics, the flow and breathing patterns, and the anatomy (see Section 3.4, p. 42 and p. 64).

The shell assessment of a 3D nuclear image of aerosol deposition (SPECT or PET) cannot estimate lobar or segmental deposition. Transformation to deposition data related to the same subject's airway generation could not be studied in detail because of the limited set of data (see section 5.4, p. 141). Still, deposition measurements per shell offer a detailed description of the deposition in relation to the radial depth in the lungs. Results such as in Figure 7-1 for the right lung, showing deposition occurring largely at the lung periphery where it is uniformly distributed, agree with previous clinical studies using similar breathing pattern and fine aerosol characteristics measured with planar imaging (central to peripheral ratio, see Section 3.3.2, p. 55) and shell analysis (e.g. Fleming et al. (1996a)). It is however of note, at this point, that, inherently, the shell description would not be adequate to study aerosol deposition distributions that are very inhomogeneous. The shell formation is an automated computed process that relies only on the definition by the operator of the hilum. It is the basis of the assessment of aerosol deposition in several centres (e.g. Southampton General Hospital, Cleveland University Hospitals). In order to compare shell deposition data between the centres, it is important to know the extent to which the results are operator dependent. The reproducibility of the results shown between the 1995 study and the re-assessment presented here is encouraging. Again, transformation of the original SPECT data using a ventilation scan in the same subject (see above) would allow measurements of shell deposition per air volume.

Regarding this study, it would be interesting to quantify the deposition in relation to the subject's anatomy from both SPECT and pulmonary anatomical information obtained with the patient in vertical position. This is because (1) the lung contours and volume change from upright to horizontal positions (particle inhaling and imaging position respectively), and (2) the particles deposited in the lungs after inhalation in an upright position may be displaced when the patient lies down on the SPECT bed. Translocation of the drug and mucociliary clearance

may have occurred during the imaging time but we do not know to what extent. The relative ratios stated in Tables 7.1 to 7.3 thus assume that these processes took place uniformly in each lobe. In the shell analysis, it is ignored, although modelling of clearance of the drug through the lungs has recently been attempted [Fleming et al. (2000a)].

7.5 Conclusion

In this chapter, aerosol deposition was assessed in relation to the subject's own anatomy. This removed the influence of anatomical intersubject variability which is a limitation of (1) the current assessment techniques, (2) the prediction models and (3) the validation of predictions. This pilot study used the SPECT studies performed on the volunteer for whom the anatomical models were developed in the previous chapter.

The aerosol deposition per lobe was assessed and a vertical gradient increasing from the upper to the lower lobes was quantified. This data will help validate theoretical predictions. Unfortunately the partial volume effect limited the assessment of the deposition in each generation. In the future, a combination of better image processing on radionuclide images or the higher resolution imaging techniques should help overcome this limitation and describe the deposition in more detail.

The study demonstrates that better knowledge of the anatomy allows finer interpretation of the aerosol deposition, which will be more meaningful for both clinicians and the aerosol industry. Problems related to using a standard model, rather than a bespoke one were discussed, but only from one data set. More experiments are necessary. In particular, further study to assess the extent to which the low resolution of SPECT imaging can "hide" variations between subjects should be investigated. Assessment of deposition per shell appeared not to depend strongly on accuracy of the hilum definition in the present study. This should be confirmed with more experiments. For assessment of lobar and shell aerosol deposition per air volume, correction of the original activity map is suggested by use of an additional 3D ventilation scan.

Chapter 8

Conclusions and suggestions for further work

This project was undertaken within the Southampton Aerosol Group, which studies the fate of inhaled aerosols in the lungs, their consequences on health, and the relationship between deposition site and clinical effect in inhalation therapy. Clinical, research and economic interests in these topics have been proven by several collaborations with universities and companies in the last ten years.

Aerosol deposition distribution in the lungs can be assessed by radionuclide imaging. The Southampton Aerosol Group has, in particular, pioneered the use of multi-modality imaging for aerosol deposition studies and has developed techniques to analyse its spatial distribution. The group has also developed a method of predicting aerosol deposition distribution using computer-modelling of the particle paths in the airways.

Both techniques use anatomical models of the airways that lack 3D reality and that do not take into account the anatomical variability that exists between subjects. As a consequence, aerosol deposition assessment and predictions cannot be related to the subject's anatomy. It is then difficult to link deposition site with clinical effect and therefore to know where to target the drug. It is also difficult to validate aerosol deposition predictions from computer-modelling with *in vivo* measurements.

The group has previously made some attempt to assess distribution using simplified models of the airway anatomy. The thesis was concerned with improvements in these methods. The approach taken was to, first, investigate the 3D topol-

ogy and morphology of the airways. This represents the main contribution of the thesis. The modelling of realistic anatomy and the aerosol deposition measurements in relation to the subject's anatomy were then investigated. This was with the view to obtaining *in vivo* 3D anatomical data to relate the location of aerosol deposition to the subject's anatomical features such as airways, lobes and segments.

8.1 Summary Of The Work

An algorithm was developed to calculate semi-automatically both the morphology and the location in 3D space of the airways from their CT images. To be able to describe the 3D topology of the airways is new. Furthermore, the method is a large improvement from the time-consuming manual measurements of the airways and it allows both *in vivo* and *post mortem* analysis to be carried out. It was tested on the CT images of a tracheobronchial lung cast and applied to the CT images of the airway tree of a healthy volunteer. Diameter, length, branching and gravity angles and further angular parameters that define the orientation of the airways in space and at bifurcations were tabulated for the first nine conducting airways generations of the cast and the first six generations of the volunteer. The tabulating algorithm was shown to produce airway dimensions which compare well with the literature, where available. The analysis of the spatial distribution of the central airways showed clear lobar patterns. Non-planar geometry at bifurcations was also shown.

Next, a method was developed to automatically generate realistic 3D models of the airways from their CT images and the knowledge of the diameter and orientation of each airway tabulated with the previous algorithm. The resulting models can be expressed in terms of airway, generation or lobe. The method was applied to the cast and the volunteer's images. A method to model 3D realistic pulmonary segments followed on. It is based on an automated region growing process to simulate the "fight for space" that occurs during the lung formation. The identification of the segmental bronchi by the operator and the MR images of the lung outlines are also necessary. The resulting airway models are clearly 3D realistic. The segmental modelling method could not be validated because of the lack of *in vivo* data. But the 3D realism of the lobar models, obtained with the same method, is encouraging, although only one *in vivo* data set could be investigated.

The assessment of the volunteer's aerosol deposition distribution was then attempted using the airway and lobar models, created from his own anatomical data with the methods described above. The aerosol deposition studies were two supine SPECT examinations, both performed with fine radiolabelled particles inhaled in an upright position from a nebuliser. The study demonstrated that better knowledge of the anatomy allows improved interpretation of the aerosol deposition. The deposition assessment in the volunteer's lobar anatomy generated by the growing region modelling method was shown to be the same as in the anatomical map generated from the manual segmentation of the lobar fissures in the volunteer's CT images. This confirmed the 3D realism of the lobar model. A vertical gradient was quantified in the lobar concentration of aerosol per space volume in the volunteer's lobes, increasing from the upper to the lower lobes. For assessment of the deposition per air volume, correction of the original activity map was suggested by the use of an additional 3D ventilation scan. The deposition assessment in the volunteer's lobar model compared to that in a model describing the "standard" location and size of the lobes in anatomical books, gave different results, suggesting the advantage of using a model that describes the subject's own anatomy, rather than an approximated one. However, more experiments are necessary to conclude whether a precise anatomical model is essential to SPECT interpretation. The interpretation of the aerosol deposition in each airway generation was limited by the poor resolution of SPECT imaging.

8.2 Significance Of The Results

The dimensions obtained from the cast and the volunteer extend the data base on human lung morphology and thus contribute to the knowledge of lung morphometry. The analysis of CT images of more casts using this algorithm could quickly provide large sets of data, especially on branching angle values and 3D topology, on which there is little information in the literature. In turn, estimates of the anatomical variability existing between subjects may contribute to the understanding of the variability shown *in vivo* between subjects, in the response to a treatment.

The findings relative to the lobar patterns of the airways studied are important for improving the 3D realism of the conducting airway structure modelling, as they show that a "global" view and description of the airway distribution in the whole lung is not realistic. They are also very relevant for predicting aerosol deposition.

This is because the airway tree geometry has been shown to play a role in aerosol deposition mechanisms. The information brought on the spatial arrangement of the airways and the non-planarity of their geometry at bifurcations is particularly exciting as recent research suggests that it contributes to the clearance of material from bends [Caro et al. (1996), Caro et al. (2000)] and may therefore have implications on the aerosol deposition in the airways. The data obtained from the cast and the volunteer, thus, give preliminary information to investigate the above hypothesis by studying the 3D flow and aerosol deposition patterns in the airways. Furthermore, the cast and the volunteer's airway models have been recently given to the Department of Applied Biomedical Engineering, Cleveland State University to be used in Computational Fluid Dynamics simulations to study particle deposition at bifurcations.

The assessment of the lobar gradient in the volunteer's SPECT studies may be of value to aid in understanding the role of the lobes in aerosol deposition. These data, expressed in relation to the air volume in the lobes, may also contribute to validate theoretical computer-models that predict lobar aerosol deposition.

The determination of the relationship between air volume in airway generations and shells for the volunteer gave the opportunity to evaluate the existing conceptual shell-generation model. It highlighted certain errors in the model and this new information will help in developing an improved version.

8.3 Future Work

With a view to the routine use of the algorithm to tabulate the dimensions and topology from either more casts or *in vivo* studies, the full automation of the algorithm is an important aspect to consider. Development of techniques for eliminating the manual correction required at some bifurcations (29% of the branchings corrected in the cast data that contained 9 generations and 9% in the volunteer data that contained 6 generations), where clusters appeared in the skeletonization process, would thus be a valuable improvement of the algorithm. Investigation of new image processing methods to find the middle line of the airways would also be worthwhile. Suitable automated segmentation algorithms to extract the airway tree would also be welcome.

The use of CT imaging in the thesis was shown to limit the number of airways that could be imaged, particularly in *in vivo* situations where the X-ray dose to

the subject is to be kept low. The rapid development of hyperpolarized He-3 MR imaging, which is X-ray dose free and is shown very promising for imaging the airways, should thus be closely followed. One would hope for the replacement of the CT examination carried out on the subject by a He-3 MR examination to allow the visualisation of more airways and segmental outlines. The breathing and cardiac artefacts in MR imaging can already be eliminated; the financial costs and the scanner availability for such an examination are currently unknown.

The results presented regarding the modelling of the anatomical features and its use for the aerosol deposition assessment are encouraging, but represent only one dataset. Further *in vivo* experiments would be valuable. In practice, the number of imaging modalities required (three) in the protocol of the study presented here, may be limiting. Clearly, the segment modelling method requires more data for its evaluation. Also, the use of pulmonary arteries imaged with a time-of-flight MR scan, instead of the airways in the growing process may be envisaged. It would especially be of interest to study the shape of the lobes and segments in diseased lungs.

The extent to which the low resolution of SPECT imaging can "hide" anatomical variations between subjects should be investigated. For such study, the use of computer-simulated SPECT images would be valuable, derived from a known deposition distribution in lobes and segments of various size and shape. The errors in the lobar and segmental deposition concentration measured on the SPECT images using the original anatomical map or using a fitted standard model could be estimated. In the future, a combination of better image processing on radionuclide images or higher resolution imaging techniques should help describe the aerosol deposition in more detail, overcoming the limitations of the partial volume effect in current SPECT imaging.

Appendix A

Ethics Committee application form and approval

The Ethics Committee application form concerned the CT examination on the volunteer (see Section 5.2, p. 93). It was written by the author, who was the main applicant. Dr. J.S. Fleming, Dr. J.S. Conway, Mr. P. Halson, Dr. I.W. Brown and Dr. P.C. Jackson, of Southampton General Hospital, were also involved.

The appendix contains:

1. the South and West Local Research Ethics Committee application form.
2. the protocol of the study.
3. the recruitment letter.
4. the information sheet for volunteers.
5. the consent form.
6. the GP information sheet.
7. a copy of the Ethics Committee approval.

SECTION 1 Details of applicant(s)

1. **Short title of project** *(in not more than 6 words)*
3D airway morphology using CT

Full title
Investigation of the 3D morphology and topology of the first generations of conducting airways for 3D assessment of aerosol deposition

Summary of practical benefits/improvements in patient care which are envisaged
The study will answer the clinical need to know in which actual airway an inhaled aerosol is deposited. The central airways 3D morphology will also be used to improve deposition modelling that aims to minimise in vivo studies in the future when assessing the behaviour of various nebulised drugs.

2. **Applicant** *(All correspondence will be sent to this address unless indicated otherwise.)*

Surname: Sauret Forename: Veronique Title: Ms

Present appointment of applicant:
Clinical Scientist
Medical Physics & Bioengineering Department, Southampton General Hospital
Qualifications:
BSc, MSc

Address:
Medical Physics & Bioengineering Department, MP 29
Southampton General Hospital
Tremona Road, Southampton SO16 6YD
Tel: 01703 794470 Fax: 01703 794117 Out of hours tel: 01703 796738

3. **Other workers and departments/institutions involved**

Dr John S Fleming, Medical Physics & Bioengineering Dept, Southampton General Hospital

Dr Joy H Conway, University of Medicine, Southampton General Hospital

Dr Peter Halson, Medical Physics & Bioengineering Dept, Southampton General Hospital

Dr IW Brown, Consultant in Cardiothoracic Radiology, Southampton General Hospital

4. **Signature of relevant bodies**

I undertake to carry out the work in accordance with the principles of the Declaration of Helsinki (copy available from the LREC secretary) and its amendments.

Signature of applicant ..... Date .....

Signature of Head of Department/Supervisor/Principal in General Practice with overall responsibility for the project..... Date .....

NAME AND TITLE IN CAPITALS.....

I am fully aware of the details of this project and happy for it to continue as outlined here.

Signature(s) of relevant Clinical Director(s) where study is being conducted/Medical Director(s) signing on behalf of Trust(s) involved (where appropriate)

..... Date .....

NAME AND TITLE IN CAPITALS.....

SECTION 2 Details of project

This section must be completed. A copy of the protocol should be enclosed with the application form, but it is not sufficient to complete questions by referring to the protocol.

5. Aims and objectives of project (i.e., what is the intention of the project?)

It is proposed to investigate the 3D morphology and topology of the airways:

(a) to collect pilot data on the spatial location of the central conductive airways,
(b) to assess the spatial distribution of aerosol deposition in term of deposition per airway,
(c) to input the 3D morphological data in the deposition prediction algorithm developed here within the Southampton Aerosol Group and compare its prediction with (b).

Study endpoints: completed data collection on two subjects

6. Scientific background of study

Improvement of patient care by drug delivery to the lung is a major application of aerosol deposition studies. At Southampton General Hospital 3D vizualization of inhaled radiolabeled aerosol in the lung (Single Photon Emission Computed Tomography, SPECT) has been developed for this application within the established Southampton Aerosol Group. To assess what amount of aerosol is in each actual airway from the SPECT images, the knowledge of the subject's morphology is important.
This group has also develop an aerosol deposition prediction algorithm that can be greatly improved by real 3D information on the subject's central airways morphology.

In order to improve the assessment of aerosol deposition in both SPECT images and develop a sensible prediction model, the 3D morphology and topology of the subject's airways require investigation.

7. Brief outline of project (i.e., what do you intend to do?)

It is proposed to study two subjects who have been selected from the previous trial undertaken in 1994 by Dr J.H. Conway, Dr J.S. Fleming and Professor S.T. Holgate and that has provided SPECT images of aerosol deposition in the lung.

One 120mm long CT scan centered on the higher part of the patient's chest will image the trachea bifurcation and the first conductive airways.

The correlation between the previous SPECT images and the 3D morphology will be of clinical interest since it will give a true measure of the aerosol deposition in each airway.
The 3D morphological data will be used to test out the deposition prediction algorithm.

8. **Study design** *(e.g. cohort, case control)*

Descriptive clinical trial. Pilot study.

9. **i) How was the size of the study determined?**

It was considered the minimum size to obtain information in this pilot study. If the study is successful, a full trial will be considered.

ii) Was there formal statistical input into the overall study design?

☐ Yes ☒ No

If *Yes*, please give name of adviser:

iii) What method of analysis will be used?

The CT image data will be analysed to estimate the location, size and shape of the conducting airways using previously developed in house software.

10. **Does the study fall into any of the following categories?**

Pilot	☒ Yes	☐ No
Multi-centre study	☐ Yes	☒ No
Student project *(part of course requirement)*	☐ Yes	☒ No

If student project, what course is being undertaken, in which institution?

If this is a multi-centre study, please complete the details below, otherwise go to Question 11.

i) Which centres are involved?

ii) Which ethics committees have been approached, and what is the outcome to date?

iii) Who will have overall responsibility for the study?

iv) Who has control of the data generated?

11. **Where will the study take place and in what setting?**

The study will take place at the Department of Radiology, Southampton General Hospital

12. **Is any payment being made, or actively being sought by the investigator or department/unit in respect of this study (include research grants)?** ☐ Yes ☒ No

If Yes, complete the section below; if No, go to Question 13.

i) **Is the payment:**

a) A block grant ☐ Yes ☐ No

If *Yes*, give details, including amount and source of funding £

Name of funding body: .....

b) Based on the number of subjects recruited ☐ Yes ☐ No

If payment is based on number of subjects recruited (per capita/payment), state total sum payable for each subject completing the study. £

State number of subjects agreed.

Will patients have their travel costs paid? ☐ Yes ☐ No

If multi-centre study, state total number of subjects to be recruited.

ii) **Is the payment made in order to:**

			If *Yes* state sum
a) Pay a salary(ies)	☐ Yes	☐ No	£
b) Fund equipment	☐ Yes	☐ No	£
c) To support further departmental research	☐ Yes	☐ No	£
d) Other (state)	☐ Yes	☐ No	£

iii) **Who will have control of the funds? eg Charitable Trust etc.**

iv) **Does the investigator(s) have any direct personal involvement (eg financial, share-holding etc.) in the sponsoring organisation?** ☐ Yes ☐ No
(If *Yes*, give details.)

v) **Will all the costs incurred by the institution be covered by the grant?** ☐ Yes ☐ No

vi) **If the project is to be carried out in a Trust has the R&D lead in the Trust been notified of the project?** ☐ Yes ☐ No ☐ NA
If *no/NA* give reasons:

13. **Schedule**

Proposed starting date: 15.03.99 Proposed duration: 2 months

SECTION 3 Recruitment of subjects

14. How will the patients or subjects in the study be selected, approached and recruited; what inclusion and exclusion criteria will be used? STATE IF THEY ARE THE SUBJECT OF THERAPEUTIC OR NON-THERAPEUTIC RESEARCH

It is proposed to study two normal subjects who have been selected from the previous trial undertaken in 1994 by Dr Joy Conway, Dr John Fleming and Prof. Steve Holgate. They must not have declared asthma, respiratory or pulmonary diseases. They must have not undertaken an ionising radiation procedure in the last year. They must be male and over 18 years of age. They will be the subject of non-therapeutic research.

15. How many subjects will be recruited and of what age group?

2 male subjects will be recruited. Age range : 18-65.

16. How will the control group (if used) be selected, approached and recruited; what inclusion and exclusion criteria will be used? Type *NA* if no controls.

NA

17. How many controls will be recruited and of what age group?

NA

18. Are the subjects or controls included in this study involved in any other research investigation at the present time?

☐ Yes ☐ No ☒ Not known

If *Yes*, please give details.

19. Will healthy volunteers be used?

☒ Yes ☐ No

If Yes, complete details below. If No, go to Question 20.

i) What is their relationship to the investigator? None

ii) Will they receive any payment, and if so, what is the source of that funding? ☒ Yes ☐ No

If *Yes*, give details of payment per subject. Travel expenses will be covered by the Dept of Medical Physics & Bioengineering (Activity area: Asthma / Respiratory, project ID: RHM HOS/022)

Applicants should undertake to explain to volunteers that the researcher will contact their GP to ask about any drug therapy and that they must inform the researcher if they consult another doctor during the study,

SECTION 4 Consent

20. Is *written* consent to be obtained?

☒ Yes ☐ No

If *Yes*, please attach a copy of the consent form to be used.
(Guidance on consent is given in Appendices 2, 3, 4 in the Guidance Notes.)

If no written consent is to be obtained is it because one of the following methods of research is employed?

Postal questionnaire	☐ Yes	☐ No
Interview	☐ Yes	☐ No
Other	☐ Yes	☐ No

If *Other*, please justify.

21. Does the study include subjects for whom English is not a first language?

☒ Yes ☐ No ☐ NA

If *Yes* give details of arrangement made; if *No* please justify.

Subjects who took part in the previous trial spoke all English fluently. If required the translation services of the Trust will be used.

22. Are the subjects or controls in one of the following vulnerable groups?

Children under 16	☐ Yes	☒ No
People with learning difficulties	☐ Yes	☒ No
Other vulnerable groups e.g. mental illness, dementia	☐ Yes	☒ No

If Yes, please complete the details below, otherwise go to Question 23.

i) What special arrangements have been made to deal with the issues of consent and assent, e.g. is parental or guardian agreement to be obtained, and if so in what form?

ii) In what way, if any, can the proposed study be expected to benefit the individual patient/subject on whom it is performed?

23. Will the patient/subject be given a written information sheet or letter?
(For suggested format see Appendix 1 in Guidance Notes.)

☒ Yes ☐ No

If *Yes*, please attach copy to this application form.
If *No*, please justify.

SECTION 5 Details of interventions

24. Does the study involve the use of a new medicinal product or medical device, or the use of an existing product outside the terms of its product licence?

☐ Yes ☒ No

If Yes, please complete Annexe A in the Guidance Notes, otherwise go to Question 25.

25. Will any ionising or non-ionising radiation, or radioactive substances or X-Rays be administered to a patient or volunteer?

☒ Yes ☐ No

Please ensure information in Q14 includes exclusion criteria with regard to ionising radiation if appropriate.

If Yes, please complete Annexe B in the Guidance Notes, otherwise go to Question 26.

26. What investigations and/or interventions will subjects and/or controls have over and above routine care?

(Please complete the table below by selecting YES/NO options as appropriate. If YES, please give details.)

Investigation		
Self completion questionnaires	☐ Yes	☒ No
Interviews/interview administered questionnaires	☐ Yes	☒ No
Video/audio tape recording	☐ Yes	☒ No
Physical examination	☐ Yes	☒ No
Internal physical examination	☐ Yes	☒ No
Venepuncture*	☐ Yes	☒ No
Arterial puncture*	☐ Yes	☒ No
Biopsy material*	☐ Yes	☒ No
Other tissue/body sample*	☐ Yes	☒ No
Imaging investigations (not radiation)	☐ Yes	☒ No
Other investigations not part of normal care	☐ Yes	☒ No
Additional outpatients attendances	☐ Yes	☒ No
Longer inpatient stays	☐ Yes	☒ No
Local anaesthetic	☐ Yes	☒ No
General anaesthesia	☐ Yes	☒ No
Other	☒ Yes	☐ No

Details:

The study requires one 120mm CT chest scan.
The Radiology Department will be reimbursed by the Department of Medical Physics & Bioengineering for the procedure (Activity area: Asthma / Respiratory, Project ID : RHM HOS/022)

* *Please see guidance notes.*

If additional investigations or tests are involved with revenue consequences for the NHS the relevant head(s) of department(s) *must* be contacted.

Signature of Head of Department ..... Date .....

NAME IN CAPITALS..... Position.....

SECTION 6 Risks and ethical problems

27. Are there any ethical problems or considerations that the investigators consider to be important or difficult with the proposed study?

☐ Yes ☒ No

If *Yes*, please give details:

27a. Is it possible that the trial medication will not be available at the end of the trial?

☐ Yes ☐ No ☒ N/A

27b. If *yes*, is this made clear in the patient information sheet?

☐ Yes ☐ No

If *No*, give reasons

28. Are there any potential hazards to subjects or patients?

☒ Yes ☐ No

If *Yes*, please give details, and give the likelihood and details of precautions taken to meet them, and arrangements to deal with adverse events and overdoses, including reporting to the relevant authorities.

The calculation of the radiation dose was made by Mr P Halson, Head of Radiological Physics.

The risks associated with this radiation have been discussed with the Radiation Protection Adviser, Dr PC Jackson and are developed in the complement of Annexe B.

29. Is this study likely to cause discomfort or distress to subjects/patients?

☒ Yes ☐ No

If *Yes*, estimate the degree and likelihood of discomfort or distress entailed.

The procedure requires a 40 second breath-hold. This could cause a very slight discomfort to the subject.

30. **Will information be given to the patient's General Practitioner (*especially* if a drug is to be given or an invasive procedure is undertaken)?**

☒ Yes ☐ No

If *Yes*, please enclose an information sheet for the GP.
If *No*, please justify.

If the study is on hospital patients, has the consent of all consultants whose patients are involved in this research been obtained?

☐ Yes ☐ No

If the study is in general practice, has the consent of all the partners been obtained?

☐ Yes ☐ No

Where available, please enclose an information sheet for consultants or GPs.

SECTION 7 Indemnity and confidentiality

Product liability and consumer protection legislation make the supplier and producer (manufacturer) or any person changing the nature of a substance, e.g. by dilution, strictly liable for any harm resulting from a consumer's (subject or patient) use of a product.

31. i) What arrangements have been made to provide indemnification and/or compensation in the event of a claim by, or on behalf of, a subject for negligent harm?

Indemnification will be provided according to the prevailing policy of the Southampton University Hospitals NHS Trust for approved research.

ii) What arrangements been made to provide indemnification and/or compensation in the event of a claim by, or on behalf of, a subject for non-negligent harm?

Indemnification will be provided according to the prevailing policy of the Southampton University Hospitals NHS Trust for approved research.

If applicable, the arrangements involving a drug supplied by a company should conform to the most recent ABPI guidelines on patient indemnity or individual Trust documents

iii) Will a medical student be involved directly in the project?

☐ Yes ☒ No

32. In cases of equipment or medical devices, have appropriate arrangements been made with the manufacturer?
(Please indicate NA if not applicable.)

☐ Yes ☐ No ☒ NA

If *Yes*, give details.

33. i) Will the study data be held on a computer? ☒ Yes ☐ No

ii) If *Yes*, has the relevant Data Protection Officer been notified? ☒ Yes ☐ No

Give name of Data Protection Officer: Dr M Tristam .....

iii) If *No*, give reasons

34. Will the patient's medical records be examined? ☐ Yes ☒ No

If *Yes*, will information relevant to this study **only** be extracted ☐ Yes ☐ No

If extra information is extracted, please justify.

What, if any, additional steps have been taken to safeguard confidentiality of personal records?

All information will be handled in accordance with national and local guidelines concerning research confidentiality

35. Will the study include the use of any of the following?

Audio/video tape recording ☐ Yes ☒ No

Observation of patients ☐ Yes ☒ No

If *Yes* to either,

a) How are confidentiality and anonymity to be ensured?

b) What arrangements have been made to obtain consent?

c) What will happen to the tapes at the end of the study?

36. Will medical records be examined by research worker(s) outside the employment of the NHS?

☐ Yes ☒ No

If *Yes*, it is the responsibility of the principal investigator to ensure that research workers understand that they must:

i) undertake never to divulge information about patients or research subjects, recorded or otherwise, to anyone without the authority of the Consultant/GP under whose care the patient is;

ii) also understand that the names, addresses and places of work of patients or research subjects are confidential and must not be divulged.

Please ensure that you complete the check list on the front cover of the application form and enclose all relevant enclosures.

Annexe B

This form is to be used if the study involves the use of ionising or non-ionising radiation, radioactive substances or X-Rays. The Radiation Protection Adviser must be involved in implementing this section.

a) RADIOACTIVE SUBSTANCES

i) Details of substances to be administered. *(Please complete the table below.)*

Investigation	Radionucleide	Chemical form	Quantity of radio-activity to be administered (MBq)	Route	Frequency

ii) Estimated Effective Dose (Effective Dose Equivalent)** (mSv):

iii) Absorbed dose to organ or tissues concentrating radioactivity** (mGy) (Specify dose and organ.)

iv) Administration of Radioactive Substances Advisory Committee (ARSAC) Certificate holder

Name of person:

Position:

Certificate No.:

I have delegated authority to administer the radioactive substance(s) in this project to:

and I approve the arrangements that have been made.

Signature of Certificate holder ..... Date.....

b) X-RAYS

i) Details of radiographic procedures

Investigation	Organ(s)	Frequency
Helical CT scan	Chest (120 mm scan length, 3 mm slice width)	1

ii) Estimated Effective Dose (Effective Dose Equivalent)** (mSv) 2 mSv (details in Complement of Annexe B)

. .

c) NON IONISING RADIATION

i) Details of procedures

Investigation	Organ(s)	Frequency

ii) Who has given safety advice?

Investigation of the 3D morphology and topology of the first generations of conducting airways for 3D assessment of aerosol deposition

Complement to Annexe B : Estimated Effective Dose

1. Estimated Effective Dose

The Estimated Effective Dose will be of 2 mSv as calculated by Mr P Halson, Head of Radiological Physics. This estimation is based on measurements made by the Department of Medical Physics & Bioengineering on the CT scanner at Southampton General Hospital, together with data provided by the National Radiation Protection Board in its publication :

> "Normalised Organ Doses for X-ray Computed Tomography Calculated using Monte-Carlo Techniques",
> DG Jones & PC Shrimpton, NRPB, 1991 (NRPB-SR250).

This unusually low dose for a chest scan (5-8 mSv in clinical practice) is achieved by using a lower tube current (mA) than would be used in clinical practice and by imaging a shorter distance (120 mm) than would be imaged in clinical practice.

2. Radiation Protection Adviser

Dr PC Jackson, Radiation Protection Adviser, was involved in the discussions and has given advice on the risks to each volunteer.

The radiation dose to volunteer (2 mSv) falls within Category II limits (0.5 mSv to 5 mSv) of the World Health Organisation guidance on the use of ionising radiation in research, and in this case on normal volunteers. Advice has been given that the volunteers should be male of the age group 18-65 years and where possible should be selected from the upper half of the age range.

The radiation dose results in an associated risk of developing a fatal cancer of about 1 in 10,000. This equates to the excess risk of living in Cornwall for about 4 months as a consequence of greater exposure to radon gas, or equivalent to the risks of accidental fatality in the home or on the road.

Investigation of the 3D morphology and topology of the first generations of conducting airways for 3D assessment of aerosol deposition (052/99)

Project Protocol

1. Background

Improvement of patient care by drug delivery to the lung is a major application of aerosol deposition studies. At Southampton General Hospital 3D visualisation of inhaled radiolabeled aerosol in the lung (Single Photon Emission Computed Tomography, SPECT) has been developed for this application within the established Southampton Aerosol Group. Information on the amount of aerosol in each actual airway is of value in clinical research in optimising inhalation therapy and in understanding its mechanisms. This requires knowledge of the subject's morphology.

Aerosol deposition may also be predicted using computer modelling and this depends mainly on the location, size and shape of the first conducting airways. Therefore this group has also develop an aerosol deposition prediction algorithm that can be greatly improved by real 3D information on the subject's central airways morphology.

In order to improve the assessment of aerosol deposition in both SPECT images and develop a sensible prediction model, the 3D morphology and topology of the subject's airways require investigation.

2. Objectives

1) To get exact information on the spatial location of the central conducting airways,

2) To use this information to assess the spatial distribution of aerosol deposition in terms of deposition per airway from SPECT imaging data,

3) To input the 3D morphology of the subject in the deposition prediction algorithm developed here within the Southampton Aerosol Group and compare the predictions with 2).

3. Plan

It is proposed to study two male normal subjects, between 18 and 65, who have been selected from the previous trial undertaken in 1994 by Dr Joy Conway, Dr John Fleming and Prof. Steve Holgate and that has provided SPECT images of aerosol deposition in the lung. The subjects must not have declared asthma, respiratory or pulmonary diseases. They must have not undertaken a ionising radiation procedure in the last year. They will arrange the timing of the required investigation with Mr. Peter Halson, Head of Radiological Physics and Dr Brown, Consultant in Cardiothoracic Radiology.

3.1 Investigation

One 120mm long CT scan, centred on the higher part of the lung, will be carried out. This is in order to image 120 mm of the chest, including the trachea bifurcation and the central conducting airways (approx. down to generation 9). The trachea position will be evaluated from the previous SPECT images because they show the position of the hilum (large distinctive aerosol deposition) relative to the markers which were positioned on each nipple.

3.2 Settings

The CT chest scan will be carried out at Southampton General Hospital using the GE "HiSpeed Advantage" CT scanner with a large scan FOV and "SmartBeam" filter. The acquisition parameters will be the following:

- helical
- 3mm slice width
- pitch = 1
- 1 second rotation
- 120 kV, 120 mA tube current.

The scan requires 40 second breath-hold at Total Lung Capacity in order to avoid blurring on the images.

3.3 Radiation Dose

The Estimated Effective Dose will be of 2 mSv, as calculated by Mr P. Halson, Head of Radiological Physics. This estimation is based on measurements made by the Department of Medical Physics & Bioengineering on the CT scanner at SGH, together with data provided by the National Radiation Protection Board in its publication :

"Normalised Organ Doses for X-ray Computed Tomography Calculated using Monte-Carlo Techniques",

DG Jones & PC Shrimpton, NRPB, 1991 (NRPB-SR250).

The usual radiation dose for a CT examination of the chest is up to 8 mSv. This unusually low dose for a chest scan is achieved by using a lower tube current (mA) than would be used in clinical practice and by imaging a shorter distance (120 mm) than would be imaged in clinical practice.

The radiation dose to volunteer (2 mSv) falls within Category II limits (0.5 mSv to 5 mSv) of the World Health Organisation guidance on the use of ionising radiation in research, and in this case on normal volunteers. Dr PC Jackson, Radiation Protection Adviser, has given advice that the volunteers should be male of the age group 18-65 years and where possible should be selected from the upper half of the age range. The radiation dose results in an associated risk of developing a fatal cancer of about 1 in 10,000. This equates to the excess risk of living in Cornwall for about 4 months as a consequence of greater exposure to radon gas, or is equivalent to the risk of a fatal accident in the home or on the road.

3.4 Image Quality

The noise level on the images will be higher than images produced in clinical practice but will be adequate to visualise airways of diameter greater than 3 mm (i.e. in the first nine generations as quoted in Menache and Graham (1997) and Yeh and Schum (1980) from cast measurements).

3.5 Data Analysis

The airways will be segmented out manually from the CT images.

a) The airways images will be overlaid with the SPECT data to derive the aerosol deposition in terms of concentration per air volume in each airway. This will be the first direct estimation of airway deposition from imaging data. These results will also be compared with the estimates calculated from the

"conceptual airway model" technique used to interpret the deposition in the SPECT images from the previous trial (Fleming *et al*, 1994).

b) The 3D morphology and topology will be tabulated from the airways images using an algorithm previously developed by us (Sauret *et al*, 1998). The length and diameter of each airway will be averaged for comparison with published statistics on lung cast measurements (Yeh and Schum 1980, Menache and Graham 1997). The fully tabulated morphology will be used as input into the aerosol deposition prediction algorithm developed within the Southampton Aerosol Group (Hashish *et al*, 1998) in order to compare its predictions with the concentration per volume calculated in a).

4. Benefits

The assessment of the amount of aerosol in each airway answers the clinical need to know in which actual airway the aerosol is deposited. This will help understanding the mechanisms of the inhaled drug treatment by relating site of deposition to clinical efficacy and hence to optimisation of this form of therapy.

The improvement in modelling aerosol deposition will ultimately lead to a minimisation of the use of volunteers when different aerosols are investigated. Assessment of aerosol deposition models represents a major issue for testing out the behaviour of nebulised drugs largely used in asthma treatment for instance and also airborne particles such as nicotine and asbestos.

References

Fleming JS, Nassim M, Hashish AH, Bailey AG, Conway J, Holgate S, Halson P, Moore E and Martonen TB (1995) *J. Aerosol Med.* Vol. 8, No. 4, pp. 341-356.

Hashish AH, Fleming JS, Conway J, Halson P, Moore E, Williams TJ, Bailey AG, Nassim M and Holgate ST (1998) Lung deposition of particles by airway generation in healthy subjects: 3D radionuclide imaging and numerical model prediction. *J. Aerosol Sci.* Vol. 29, No.1/2, pp. 205-215.

Menache MG and Graham RC (1997) Conducting airway geometry as function of age. *Ann. occup. Hyg.* Vol. 41, Suppl 1, pp. 531-536.

Sauret V, Fleming JS, Bailey AG (1998) Development of an algorithm tabulating the 3D morphology of airway casts using CT. 4th Annual National Conference of the Institute of Physics in Engineering and Medicine, Brighton.

Yeh HC and Schum GM (1980) Models of human lung airways and their application to inhaled particle deposition. *Bull. Math. Biol.* Vol. 42, pp. 461-480.

Southampton University Hospitals NHS Trust

Department of Medical Physics and Bioengineering
Mailpoint 29
Southampton General Hospital
Tremona Road
Southampton SO16 6YD
Tel 01703 79
Fax 01703 794117

Date

Dear Mr .....,

Re: Investigation of the 3D morphology and topology of the first generations of conducting airways for 3D assessment of aerosol deposition (Ethics Committee ref. 052/99)

We are writing to you because we are recruiting volunteers who have participated in the previous trials to study the fate of aerosolized drugs in the lungs, to freely participate to our study.

Aerosol delivery to the lungs is common, especially in treatment of asthma which is a major interest at Southampton General Hospital. The fate and deposition site in the lungs of the aerosol, once inhaled, is however not well understood. The three-dimensional images of the aerosol deposition collected when you volunteered for our previous trial have helped to see qualitatively the deposition in your lungs. However the assessment of the amount of aerosol deposited in each airway, information of real clinical importance, is not possible only from these images. It also requires three-dimensional images, produced by CT scanners, of the same person's lung anatomy.

Our study is aiming to provide anatomical images of the major airways in the lungs. The procedure will involve a 12 cm long CT scan of the chest that lasts 40 seconds during which you will be asked to hold your breath. This is a modified protocol involving a much smaller radiation dose than a clinical thoracic CT scan. The radiation dose is equivalent to moving to Cornwall (which has higher natural background radiation than Southampton) for about 4 months of the year.

The new anatomical images and the images of deposition taken in your previous participation, since they will be from the same person, will lead to measurement of the aerosol deposition per airway.

If you are interested in participating to our study, please send us back the Reply Sheet enclosed or contact myself on (01703)794470 or Dr John Fleming on (01703)796202. You will be given the Information Sheet for Volunteers and the Consent Form to read. You may ask any questions you wish and you will be free to withdraw from the study at any time without giving reasons and without incurring displeasure or penalty. Your participation in the study will be entirely voluntary. You cannot participate to our study if you suffer from asthma, respiratory or pulmonary diseases or have undertaken an ionising radiation procedure in the last year.
The study will take place at the Department of Radiology, Southampton General Hospital and your travel expenses will be re-imbursed.

Thank you in advance for your co-operation.

Yours faithfully,

Ms V Sauret	Clinical Scientist, Medical Physics
Dr JS Fleming	Consultant Physicist
Dr JH Conway	Lecturer in Medicine and Physiotherapy
Mr P Halson	Head of Radiological Physics
Dr I Brown	Consultant in Cardiothoracic Radiology

Southampton University Hospitals NHS Trust

Department of Medical Physics and Bioengineering
Mailpoint 29
Southampton General Hospital
Tremona Road
Southampton SO16 6YD
Tel 01703 79
Fax 01703 794117

Information Sheet For Volunteers (052/99)

This project is aiming to provide information on the location, size and shape of the major airways in your lungs. This will be extremely useful for optimising the treatment in patients with asthma using inhalers.

The procedure you will undertake is called a CT scan. It allows us to see the inside of the body in three dimensions. If you haven't seen a scanner before, it looks like a 50cm long tunnel in the middle of an examination room. In this study we are especially interested in imaging the airways in your lungs so you will lie on a bed that the operator will position such that only your chest is actually inside the tunnel. The scanning equipment sends x-rays through the chest to detectors that capture the part of radiation that hasn't been absorbed by the tissue. A computer linked to the scanner will work out images of your chest in three dimensions.

Just before the procedure starts, you will be asked to breathe in deeply to fill in your lung with the maximum air. This is in order to get a picture of your airways fully dilated. During the procedure, which lasts 40 seconds, you will also be asked to hold your breath, keeping all the air inside. This is to get a clear picture of your chest without blurring. The procedure should not be uncomfortable at all.

The main hazard from the procedure is that you will be exposed to radiation in the form of x-rays. X-rays are used routinely for diagnostic procedures but there is a risk that exposure of this form of radiation can predispose an individual to an excess risk of cancer. The risk of developing a fatal cancer from this exposure of radiation is 1 in 10,000. This risk is equivalent to moving to Cornwall (which has higher natural background radiation than Southampton) for about 4 months of the year, or is equivalent to the risk of fatal accident in the home or on the road.

Please remember that you may ask any questions you wish, and that you are free to withdraw from the project at any time without giving reasons and without incurring displeasure or penalty. Your participation in this study is entirely volunteer. Your travel expenses will be re-imbursed.

If you have any additional enquiry, please contact Ms Sauret on (01703)794470.

Southampton University Hospitals NHS Trust

Department of Medical Physics and Bioengineering
Mailpoint 29
Southampton General Hospital
Tremona Road
Southampton SO16 6YD
Tel 01703 79
Fax 01703 794117

Consent Form

Study Title: **Investigation of the 3D morphology and topology of the first generations of conducting airways for 3D assessment of aerosol deposition (052/99)**

Please ask the participant to complete the following:

	Please cross out as necessary
Have you read the Participant Information Sheet?	Yes / No
Have you had an opportunity to ask questions and discuss this study?	Yes / No
Have you received satisfactory answers to all your questions?	Yes / No
Have you received enough information about the study?	Yes / No

To whom have you spoken? .....

Do you understand that you are free to withdraw from the study:

- At any time?
- Without having to give a reason for withdrawing?
- And without affecting your future medical care? Yes / No

Do you agree to take part in this study? Yes / No

Signed ..... Date .....

(Name in block letters) .....

Signed (Researchers):..... Date .....

Southampton
University
Hospitals
NHS Trust

Department of Medical Physics and
Bioengineering
Mailpoint 29
Southampton General Hospital
Tremona Road
Southampton SO16 6YD
Tel 01703 79
Fax 01703 794117

GP Information Sheet

Investigation of the 3D morphology and topology of the first generations of conducting airways for 3D assessment of aerosol deposition (052/99)

Dear Doctor,

We aim to complete the data collection on your patient:

Name .....

who took part in 1994 in a clinical trial looking at aerosol deposition.
The procedure will involve a 120mm long CT scan of the chest with a 40 second breath-hold. This is a modified protocol involving a much smaller radiation dose than a clinical thoracic CT scan.
This study will give us the exact spatial location of the central conductive airways. The data analysis of the images will then allow us to assess the spatial distribution of aerosol deposition pattern provided by the previous trial.

We are writing to inform you that your patient has been invited to take part in this study which will take place mid-March 99.

If you require any further information, do not hesitate to contact Ms V Sauret or Dr JS Fleming on (01703)794470.
Thank you in advance for your co-operation.

Yours faithfully,

Ms V Sauret
Clinical Scientist, Medical Physics

Dr JS Fleming
Consultant Physicist

Dr JH Conway
Lecturer in Medicine and Physiotherapy

Mr P Halson
Head of Radiological Physics

Dr I Brown
Consultant in Cardiothoracic Radiology

Southampton
University
Hospitals
NHS Trust

Southampton & S.W. Hants
Joint Research Ethics Committee
Trust Management Offices
Mailpoint 18
Southampton General Hospital
Tremona Road
Southampton SO16 6YD

Tel 01703 794912
Fax 01703 798678

Ref: CPW/DBL

11th May 1999

Ms V Sauret
Department of Medical Physics and Bioengineering
Mailpoint 29
SGH

Dear Ms Sauret

Submission No:052/99 - 3D airway morphology using CT.

Following the conditional approval and in response to your letter dated 19th April 1999, I am pleased to confirm **full approval** having received the amended recruiting letter as requested in our letter of 6th April 1999

This approval was granted on Chairmans action and was brought to the attention of the Committee at their meeting on 28th April 1999.

This committee is fully compliant with the International Committee on Harmonisation/Good Clinical Practice (ICH) Guidelines for the Conduct of Trials involving the participation of human subjects as they relate to the responsibilities, composition, function, operations and records of an independent EthicsCommittee/Independent Review Board. To this end it undertakes to adhere as far as is consistent with its Constution, to the relevant clauses of the ICH Harmonised Tripartite Guideline for Good Clinical Practice, adopted by the Commission of the European Union on 17 January 1997.

Yours sincerely,

pp Jane Carr. Vice Chair.

Clair Wilkinson (Ms)
Research Ethics Administrator

Glossary

Effective Radiation Dose The effective radiation dose is an estimate of the possible biological damage per unit dose of differing types of radiation to a tissue. It is calculated on the basis of:

1. the type of radiation used. Each type of radiation is associated with a "radiation weighting factor". X-ray and γ radiations have a weighting dose factor of 1. Radiofrequency waves, not ionising radiations, have a weighting dose factor of 0.
2. the type of tissue irradiated. Different organs or tissues have different risks assigned to them of developing cancer or genetic effects, following biological damage. Therefore each type of tissue is associated with a "tissue weighting factor".

When the radiation interacts with the atoms of the body, exchange of energy occurs. The absorbed dose is the energy absorbed by the atoms per unit mass and is measured in Grays (Gy). The product of the absorbed dose and the radiation weighting factor is the equivalent dose. The SI unit for the equivalent dose is the Sievert (Sv). The product of the equivalent dose and the weighting factor for an organ or tissue is the effective dose. It is expressed in Sieverts.

A 5 mSv dose results in an associated risk of developing a fatal cancer of about 1 in 5 000. This equates to the excess risk of living in Cornwall for about 10 months as a consequence of greater exposure to radon gas, or equivalent to the annual risk of death from working in a coal mine in the U.K. [National Radiation Protection Board (1998)].

Voxel Unit element of a volume image. A unit element within a slice of the volume, may be called a pixel, term commonly used in 2D imaging.

Neighbourhood Let p be a voxel. Its neighbours are the voxels that have a diagonal, a corner, a face or an edge in common with p.

n-Connectivity In 3D, p has 26 neighbour-voxels q. Such voxels are said to be 26-connected to p. 6-connected voxels refers specifically to the voxels q having a face in common with p.

Bibliography

J.E. Agnew. *Aerosols and the Lung: Clinical and Experimental Aspects*, pages 49–70. Butterworths, London, 1984.

J.E. Agnew. Characterising lung aerosol penetration. *Journal of Aerosol Science*, 4:237–249, 1991.

K.C. Arun, T.S. Huang, and S.D. Blostein. Least-squares fitting of 2 3-D point sets. *IEEE Transactions on Pattern Analysis and Machine Intelligence*, 9(5): 698–700, 1987.

M.I. Baskin, A.G. Abd, and J.S. Ilowite. Regional deposition of aerosolized pentamidine. Effets of body position and breathing pattern. *Annals of Internal Medicine*, 113:677–683, 1990.

F.J. Beekman. *Fully 3D SPECT reconstruction with object shape dependent scatter compensation.* PhD thesis, University of Utrecht, 1995.

M.S. Berridge, Z. Lee, and D.L. Heald. Pulmonary drug distribution and kinetics by positron tomography. *Journal of Aerosol Medicine*, 12(2):117, 1999.

J.D. Blanchard, Heyder J., C.R. O'Donnell, and J.D. Brain. Aerosol-derived lung morphometry: comparisons with a lung model and lung function indexes. *Journal of Applied Physiology*, 71(4):1216–1224, 1991.

M. Bland. *An introduction to medical statistics.* Oxford Medical Publications (2nd edition), 1997.

E.A. Boyden. The structure of the pulmonary acinus in a child of six years and eight months. *American Journal of Anatomy*, 132:275–300, 1971.

J.D. Brain and J.D. Blanchard. *Aerosols in medicine. Principles, diagnosis and therapy. 2nd edition*, chapter 5. Elsevier, 1993.

J.D. Brain and P.A. Valberg. Deposition of aerosol in respiratory tract. *American Review of Respiratory Diseases*, 120:1325–1373, 1979.

R.H. Brown and E.A. Zerhouni. New techniques and developments in physiologic imaging of airways. *Radiologic Clinics of North America*, 36(1):211–230, 1998.

P. Camner, M. Anderson, K. Philipson, A. Bailey, A. Hashish, N. Jarvis, M. Bailey, and M. Svartengren. Human bronchiolar deposition and retention of 6-, 8-, and 10-μm particles. *Experimental Lung Research*, 23:517–535, 1997.

C.G. Caro, R.C. Schroter, N. Watkins, and S.J. Sherwin. Steady inspiratory flow in planar and non-planr models of human bronchial airways. In *King's College London meeting of Physiological Society*, page (submitted), 2000.

C.J. Caro, D.J. Doorly, M. Tarnawski, K.T. Scott, Q. Long, and C.L. Dumoulin. Non-planar curvature and branching of arteries and non-planar-type flow. *Proceedings of the Royal Society London Series A*, 452:185–197, 1996.

H.-K. Chan, E. Daviskas, S. Eberl, M. Robinson, G. Bautovitch, and I. Young. Deposition of aqueous aerosol of technicium-99m diethylene triamine penta-acetic acid generated and delivered by a novel system (AER_x) in healthy subjects. *European Journal of Nuclear Medicine*, 26:320–327, 1999.

T.L. Chan, M. Lippmann, V.R. Cohen, and R.B. Schlesinger. Effect of electrostatic charges on particle deposition in a hollow cast of the human larynx-tracheobronchial tree. *Journal of Aerosol Science*, 9:463–468, 1978.

H.K. Chang and A.S. Menon. *Aerosols in medicine. Principles, diagnosis and therapy. 2nd edition*, chapter 4. Elsevier, 1993.

J.H. Conway. *The assessment of intra-pulmonary deposition of aerosols using multi-modality imaging.* PhD thesis, University of Southampton, 1996.

M. Dolovich, C. Nahmias, and G. Coates. Unleashing the PET: 3D imaging of the lung. In *Proceedings of Respiratory Drug Delivery VII*, pages 215–230, 2000.

M.J. Egan and W. Nixon. A model of aerosol deposition in the lung for use in inhalation dose assessments. *Radiation Protection Dosimetry*, 11(1):5–17, 1985.

W.H. Finlay and K.W. Stapleton. The effect on regional lung deposition of coupled heat and mass transfer between hygroscopic droplets and their surrounding phase. *Journal of Aerosol Science*, 26(4):655–670, 1995.

W.H. Finlay, K.W. Stapleton, H.K. Chan, P. Zuberbuhler, and I. Gonda. Regional deposition of inhaled hygroscopic aerosols: *in vivo* SPECT compared with mathematical modeling. *Journal of Applied Physiology*, 81(1):374–383, 1996.

J.S. Fleming. A technique for using CT images in attenuation correction and quantification in SPECT. *Nuclear Medicine Communications*, 10:83–97, 1989.

J.S. Fleming, J.H. Conway, P.S. Walker, E. Bondesson, L. Borgström, T.B. Martonen, and S.T. Holgate. The influence of pulmonary clearance on quantitative, three dimensional radionuclide imaging of inhaled aerosol deposition. In *Respiratory Drug Delivery VII*, volume 2, pages 523–526, 2000a.

J.S. Fleming, P. Halson, J. Conway, E. Moore, M. Nassim, A.H. Hashish, A.G. Bailey, S. Holgate, and T.B. Martonen. Three-dimensional description of pulmonary deposition of inhaled aerosol using data from multimodality imaging. *Journal of Nuclear Medicine*, 37:873–877, 1996a.

J.S. Fleming, A.H. Hashish, J. Conway, R. Hartley-Davies, M. Nassim, M.J. Guy, J. Coupe, S. Holgate, E. Moore, A.G. Bailey, and T.B. Martonen. A technique for simulating radionuclide images from the aerosol deposition pattern in the airway tree. *Journal of Aerosol Medicine*, 10(3):199–212, 1997.

J.S. Fleming, A.H. Hashish, J. Conway, M. Nassim, S. Holgate, P. Halson, E. Moore, A.G. Bailey, and T.B. Martonen. Assessment of deposition of inhaled aerosol in the respiratory tract of man using three-dimensional multimodality imaging and mathematical modeling. *Journal of Aerosol Medicine*, 9(3):317–327, 1996b.

J.S. Fleming, M. Nassim, A.H. Hashish, A.G. Bailey, J. Conway, S. Holgate, P. Halson, E. Moore, and T.B. Martonen. Description of pulmonary deposition of radiolabeled aerosol by airway generation using a conceptual three dimensional model of lung morphology. *Journal of Aerosol Medicine*, 8(4):341–356, 1995.

J.S. Fleming, V. Sauret, J.H. Conway, S.T. Holgate, A.G. Bailey, and T.B. Martonen. Evaluation of the accuracy and precision of lung aerosol deposition measurements from SPECT using simulation (in press). *Journal of Aerosol Medicine*, 2000b.

I. Fogelman and M. Maisey. *An atlas of clinical nuclear medicine.* Martin Dunitz, 1988.

J.B. Forrest. Structural aspects of gas exchange. *Federation Proceeding*, 38:209–214, 1979.

C.S. Garrard, T.R. Gerrity, J.F Schreiner, and D.B. Yeates. Analysis of aerosol deposition in the healthy human lung. *Archives of Environmental Health*, 36 (4):184–193, 1987.

T.R. Gerrity, C.S. Garrard, and D.B. Yeates. Theoretic analysis of sites of aerosol deposition in the human lung. *Chest*, 80(6):898–901, 1981.

T.R. Gerrity, P.S. Lee, F.J. Hass, A. Marinelli, P. Werner, and R.V. Lourenco. Calculated deposition of inhaled particles in the airway generations of normal subjects. *Journal of Applied Physiology*, 47(4):867–873, 1979.

R.C. Gonzales and P. Wintz. *Digital Imaging Processing (2nd edition).* Addison-Wesley Publishing Company, Inc., 1987.

B. Haefeli-Bleuer and E.R. Weibel. Morphometry of the human pulmonary acinus. *Anatomical Record*, 220:401–414, 1988.

J.E. Hansen, E.P. Ampaya, G.H. Bryant, and J.J. Navin. Branching pattern of airways and air spaces of a single human terminal bronchiole. *Journal of Applied Physiology*, 38:983–989, 1975.

A.H. Hashish and A.G. Bailey. Electrostatic enhancement of particle deposition in the lung when using jet and ultrasonic nebulisers. *Institute of Physics Conference Series*, 118(1):45–50, 1991a.

A.H. Hashish and A.G. Bailey. The importance of electrostatic charge on the deposition of fibrous particles in human and rat lungs. *Institute of Physics Conference Series*, 118(1):51–56, 1991b.

A.H. Hashish, A.G. Bailey, and T.J. Williams. A mathematical model of the human lung which accounts for the depositional effect of charge on aerosol particles. In *Proceedings of the 2nd Conference of the Aerosol Society*, pages 121–126, 1988.

A.H. Hashish, A.G. Bailey, and T.J. Williams. Selective deposition of pulsed charged aerosols in the human lung. In *Proceedings of Drug Delivery to the Lungs IV*, pages 15–19, 1993.

A.H. Hashish, J.S. Fleming, J. Conway, P. Halson, E. Moore, T.J. Williams, A.G. Bailey, M. Nassim, and S. Holgate. Lung deposition of particles by airway generation in healthy subjects: three-dimensional radionuclide imaging and numerical model prediction. *Journal of Aerosol Science*, 29(1/2):205–215, 1998.

K. Higashi. Fluorine-18-FDG PET imaging is negative in bronchioalveolar lung carcinoma. *Journal of Nuclear Medicine*, 39(6):1016–1020, 1998.

W. Hofmann and L. Koblinger. Monte Carlo modeling of aerosol deposition in human lungs. Part II: Deposition fractions and their sensitivity to parameter variations. *Journal of Aerosol Science*, 21(5):675–688, 1990.

W. Hofmann, L. Koblinger, R. Bergmann, J.S. Fleming, A.H. Hashish, and J.H. Conway. Spatial aerosol deposition patterns in the human lung: stochastic predictions vs experimental SPECT data. *Annals of Occupational Hygiene*, 41 (Suppl. 1):576–581, 1997.

K. Horsfield and G. Cumming. Angles of branching and diameters of branches in the human bronchial tree. *Bulletin of Mathematical Biophysics*, 29:245–259, 1967.

K. Horsfield and G. Cumming. Morphology of the bronchial tree in man. *Journal of Applied Physiology*, 24(3):373–383, 1968.

K. Horsfield, G. Dart, D.E. Olson, G.F. Filley, and G. Cumming. Models of the human bronchial tree. *Journal of Applied Physiology*, 31(2):207–217, 1971.

International Commission on Radiological Protection Task Group. *Publication 66. Human respiratory tract model for radiological protection.* Pergamon, 1994.

International Commission on Radiological Protection Task Group on Lung Dynamics. Deposition and retention models for internal dosimetry of the human respiratory tract. *Health Physics*, 12:173–207, 1966.

G.A. Johnson, L. Hedlund, and J. MacFall. A new window into the lung. *Physics World*, pages 35–38, 1998.

H.-U. Kauczor. Helium-3 imaging of pulmonary ventilation. *British Journal of Radiology*, 71:701–703, 1998.

H.-U. Kauczor, D. Hofmann, K-F Kreitner, H. Nilgens, R. Surkau, W. Heil, A. Potthast, M.V. Knopp, E.W. Otten, and M. Thelen. Normal and abnormal pulmonary ventilation: visualization at hyperpolarized He-3 MR imaging. *Radiology*, 201(2):564–568, 1996.

H.-U. Kauczor, R. Surkau, and T. Roberts. MRI using hyperpolarized noble gases. *European Radiology*, 8:820–827, 1998.

H. Kitaoka, R. Takaki, and B. Suki. A three-dimensional model of the human airway tree. *Journal of Applied Physiology*, 87(6):2207–2217, 1999.

L. Koblinger and W. Hofmann. Analysis of human morphometric data for stochastic aerosol deposition calculations. *Physics in Medicine and Biology*, 30(6): 541–556, 1985.

L. Koblinger and W. Hofmann. Monte Carlo modeling of aerosol deposition in human lungs. Part I: Simulation of particle transport in a stochastic lung structure. *Journal of Aerosol Science*, 21(5):661–674, 1990.

L. Lam, S.W. Lee, and C.Y. Suen. Thinning methodologies – A comprehensive survey. *IEEE Transactions on Pattern Analysis and Machine Intelligence*, 14 (9):869–885, 1992.

H.D. Landahl. On the removal of airborne droplets by the human respiratory tract. I. The lung. *Bulletin of Mathematical Biophysics*, 12:43–56, 1950.

C.F. Lange and W.H. Finlay. Introducing new dimensions in the modelling of pharmaceutical aerosols. In *Proceedings of Respiratory Drug Delivery VII*, pages 569–571, 2000.

L. Latecki and C.M. Ma. An algorithm for a 3D simplicity test. *Computer Vision and Image Understanding*, 63(2):388–393, 1996.

B.L. Laube. *In vivo* measurements of aerosol dose and distribution: clinical relevance. *Journal of Aerosol Medicine*, 9(Suppl. 1):S–77–S–91, 1996.

Z. Lee, M.S. Berridge, W.H. Finlay, and D.L. Heald. Airway generation mapping of aerosol drug deposition data. *Journal of Aerosol Medicine*, 12(2):131, 1999a.

Z. Lee, D.L. Heald, and M.S. Berridge. Comparison of PET and gamma scintigraphy: validation studies. *Journal of Aerosol Medicine*, 12(2):134, 1999b.

S. Lobregt, P.W. Verbeek, and F.C.A. Groen. Three-dimensional skeletonization: principle and algorithm. *IEEE Transactions Pattern Analysis and Machine Intelligence*, PAMI-2(1):75–77, 1980.

C.M. Ma and M. Sonka. A fully parallel 3D thinning algorithm and its applications. *Computer Vision and Image Understanding*, 64(3):420–433, 1996.

P.T. Macklem, R.G. Fraser, and D.V. Bates. Bronchial pressures and dimensions in health and obstructive airway disease. *Journal of Applied Physiology*, 18(4): 699–706, 1963.

J.S. Magnussen, P. Chicco, A.W. Palmer, D.W. Machey, M. Magee, I.Provan, C. Murray, G. Bautovitch, K. Allman, G. Storey, and H. Van der Wall. Optimization of the scintigraphic segmental anatomy of the lungs. *Journal of Nuclear Medicine*, 38:1987–1991, 1997.

G. Malandain and G. Bertrand. Fast characterization of 3D simple points. In *IEEE International Conference on Pattern Recognition. Proceedings*, pages 232–235, 1992.

T.B. Martonen. Measurement of particle dose distribution in a model of a human larynx and tracheobronchial tree. *Journal of Aerosol Science*, 14:11–22, 1983.

T.B. Martonen, Y. Yang, D. Hwang, and J.S. Fleming. Computer simulations of human lung structures for medical applications. *Computers in Biology and Medicine*, 25(5):431–446, 1995.

T.B. Martonen, Z. Zhang, G. Yu, C. Musante, D. Hwang, R. Segal, and J.S. Fleming. Targeted delivery of inhaled proteins. *Journal of Aerosol Medicine*, 12(2):133, 1999.

C. Melandri, G. Tarroni, V. Prodi, T. De Zaiacomo, M. Formignani, and C.C. Lombardi. Deposition of charged particles in the human airways. *Journal of Aerosol Science*, 1983.

M.G. Menache and R.C. Graham. Conducting airway geometry as a function of age. *Annals of Occupational Hygiene*, 41(Suppl. 1):531–536, 1997.

J. Milic-Emili, J.A.M. Henderson, M.B. Dolovitch, D. Trop, and K. Kaneko. Regional distribution of inspired gas in the lung. *Journal of Applied Physiology*, 21(3):749–759, 1966.

K. Mori, J.-I. Hasegawa, J.-I. Toriwaki, H. Anno, and K. Katada. Automated extraction and visualization of bronchus from 3D CT images of lung. In *Computer Vision, Virtual Reality and Robotics in Medicine. Proceedings*, pages 542–548, 1995.

P.E. Morrow and C.P. Yu. *Aerosols in medicine. Principles, diagnosis and therapy. 2nd edition*, chapter 6. Elsevier, 1993.

J.D. Mortensen, J.D. Young, L. Stout, A. Stout, B. Bagley, and R.N. Schaap. A numerical identification system for airways in the lung. *Anatomical Record*, 206: 103–114, 1983.

National Radiation Protection Board, editor. *Living with radiation.* National Radiation Protection Board, 1998.

F.H. Netter. *Atlas of Human Anatomy.* CIBA-GEIGY Limited, 1991.

S.P. Newman, A.R. Clark, N. Talaee, and S.W. Clarke. Lung deposition of 5 mg intal from a pressurised metered dose inhaler assessed by radiotracer technique. *International Journal of Pharmaceutics*, 74:203–208, 1991.

D.E. Olson, G.A. Dart, and G.F. Filley. Pressure drop and fluid flow regime of air inspired into the human lung. *Journal of Applied Physiology*, 28(4):482–494, 1970.

P.R. Owen. Turbulent flow and particle deposition in the trachea. In *Ciba Foundation Symposium on circulatory and respiratory mass transport*, pages 236–252, 1969.

H. Parker, K. Horsfield, and G. Cumming. Morphology of distal airways in the human lung. *Journal of Applied Physiology*, 31(3):386–391, 1971.

S. Perring, Q. Summers, J.S. Fleming, M.A. Nassim, and S.T. Holgate. A new method of quantification of the pulmonary regional distribution of aerosols using combined CT and SPECT and its application to nedocromil sodium administered by metered dose inhaler. *British Journal of Radiology*, 67:46–53, 1994.

R.F. Phalen, M.J. Oldham, C.B. Beaucage, T.T. Crocker, and J.D. Mortensen. Postnatal enlargement of human tracheobronchial airways and implications for particle deposition. *Anatomical Record*, 212:368–380, 1985.

R.F. Phalen, H.C. Yeh, O.G. Raabe, and D.J.Velasquez. Casting the lungs *in situ*. *Anatomical Record*, 177:255–264, 1973.

R.F. Phalen, H.C. Yeh, G.M. Schum, and O.G. Raabe. Application of an idealized model to morphometry of the mammelian tracheobronchial tree. *Anatomical Record*, 190:167–176, 1978.

C.G. Phillips and S.R. Kaye. Diameter-based analysis of the branching geometry of four mammalian bronchial trees. *Respiration Physiology*, 102:303–316, 1995.

C.G. Phillips and S.R. Kaye. On the asymmetry of bifurcations in the bronchial tree. *Respiration Physiology*, 107:85–98, 1997.

C.G. Phillips, S.R. Kaye, and R.C. Schroter. Diameter-based analysis of the branching geometry of the bronchial tree. Part I. Description and application. *Respiration Physiology*, 98:219–226, 1994.

P.R. Phipps, I. Gonda, D.L. Bailey, P. Borham, G. Bautovich, and S.D. Anderson. Comparison of planar and tomographic gamma scintigraphy to measure the penetration index of inhaled aerosols. *American Review of Respiratory Diseases*, 139:1516–1523, 1989.

J.N. Pritchard, S.J. Jefferies, and A. Black. Sex-differences in the regional deposition of inhaled particles in the 2.5-7.5 μm size range. *Journal of Aerosol Science*, 17:385–389, 1986.

O.G. Raabe, H.C. Yeh, G.M. Schum, and R.F. Phalen. *Tracheobronchial Geometry: Human, Dog, Rat, Hamster (Report LF-53).* Albuquerque, NM: Lovelace Foundation for Medical Education and Research, 1976.

P.A. Rinck, editor. *Magnetic Resonance in Medicine.* Blackwell Scientific Publications, 1993.

G. Rudolf, J. Gehart, J. Heyder, C.F. Schiller, and W. Stahlhofen. An empirical formula describing aerosol deposition in man for any particle size. *Journal of Aerosol Science*, 17(3):350–355, 1986.

A.A. Salam. Investigation of the use of the simulation in evaluation of image interpretation in radionuclide image. Master's thesis, University of Surrey, 1998.

V. Sauret, J.S. Fleming, and A.G. Bailey. Three dimensional topology and morphology of airways using lung cast CT images. *Journal of Aerosol Medicine*, 12 (2):126, 1999a.

V. Sauret, J.S. Fleming, and A.G. Bailey. 3D computer asymmetric model of the airways. *Nuclear Medicine Communications*, 21(2):208, 2000a.

V. Sauret, J.S. Fleming, and A.G. Bailey. 3D realistic anatomical model of the central airways to improve aerosol deposition predictions and medical analysis. In *Proceedings of Respiratory Drug Delivery VII*, pages 527–529, 2000b.

V. Sauret, J.S. Fleming, and A.G. Bailey. Realistic three-dimensional model of the central airways using healthy volunteer CT images. In *World Congress in Medical Physics and Bioengineering CD-Rom Proceedings*, pages WE–B305–01, 2000c.

V. Sauret, J.S. Fleming, A.G. Bailey, P. Halson, and K.A. Goatman. Interpretation of SPECT data on aerosol deposition in relation to the airway tree. *Nuclear Medicine Communications*, 21(4):393, 2000d.

V. Sauret, K.A Goatman, J.S. Fleming, and A.G. Bailey. Development of an algorithm tabulating the three dimensional morphology of airway casts using CT images. In *IPEM Fourth Annual Conference Proceedings*, page 181, Brighton, 1998.

V. Sauret, K.A Goatman, J.S. Fleming, and A.G. Bailey. 3D topology and morphology of branching networks using computed tomography - Applications to the airway tree. In *Proceedings of Medical Image Understanding and Analysis*, pages 73–76, 1999b.

V. Sauret, K.A Goatman, J.S. Fleming, and A.G. Bailey. Semi-automated tabulation of the 3D topology and morphology of branching networks using CT: application to the airway tree. *Physics in Medicine and Biology*, 44:1625–1638, 1999c.

R.B. Schlesinger and L.A. McFadden. Comparative morphometry of the upper bronchial tree in six mammalian species. *Anatomical Record*, 199:99–108, 1981.

J.P. Schreider and O.G. Raabe. Structure of the human respiratory acinus. *American Journal of Anatomy*, 162:221–232, 1981.

T.T. Soong, P. Nicolaides, C.P. Yu, and S.C. Soong. A statistical description of the human tracheobronchial tree geometry. *Respiration Physiology*, 37:161–172, 1979.

W. Stahlhofen, G. Gebhart, and J. Heyder. Experimental determination of the regional deposition of aerosol particles in the human respiratory tract. *American Industrial Hygiene Association Journal*, 41(6):385–398, 1980.

W. Stahlhofen, G. Rudolf, and A.C. James. Intercomparison of experimental regional aerosol deposition data. *Journal of Aerosol Medicine*, 2:285–308, 1989.

B. Suki, R. Majumdar, R. Takaki, and H. Kitaoka. A three-dimensional model of the human airway tree: application for airway-parenchymal interaction. In *The First Joint BMES/EMBS Conference Serving Humanity, Advancing Technology*, page 349, 1999.

D.B. Taulbee and C.P. Yu. A theory of aerosol deposition in the human respiratory tract. *Journal of Applied Physiology*, 38:77–85, 1975.

B.H. Thompson, W.J. Lee, J.R. Galvin, and J.S. Wilson. Virtual hospital: Lung anatomy. *http://www.vh.org/Providers/Textbooks/LungAnatomy*, 1999.

A. Thurlbeck and K. Horsfield. Branching angles in the bronchial tree related to order of branching. *Respiration Physiology*, 41:173–181, 1980.

G.J. Tortora and S. Reynolds-Grabowski. *Principles of anatomy and physiology.* HarperCollins Publishers Inc., 1996.

S. Webb. *The physics of medical imaging.* Institute of Physics Publishing Ltd, 1988.

W.R. Webb, N.D. Muller, and D.P. Naidich. *High-resolution CT of the Lung.* Raven Press, 1992.

E.R. Weibel. *Morphometry of the human lung.* Heidelberg:Springer Verlag, 1963.

E.R. Weibel. *The Lung: Scientific Foundations*, chapter Design of airways and blood vessels considered as branching trees. Raven Press, 1976.

B.J. West, V. Bhargava, and A.L. Golderberg. Beyond the principle of similitude: Renormalization in the bronchial tree. *Journal of Applied Physiology*, 60(3): 1089–1097, 1986.

T.A. Wilson. Design of the bronchial tree. *Nature*, 18:668–669, 1969.

S.A. Wood, E.A. Zerhouni, J.D. Hoford, E.A. Hoffman, and W Mitzner. Measurement of three-dimensional lung tree structures by using computed tomography. *Journal of Applied Physiology*, 79(5):1687–1697, 1995.

H.-C. Yeh and G.M. Schum. Models of human lung airways and their application to inhaled particle deposition. *Bulletin of Mathematical Biology*, 42:461–480, 1980.

H.-C. Yeh, G.M. Schum, and M.T. Duggan. Anatomic models of the tracheobronchial and pulmonary regions of the rat. *Anatomical Record*, 195:483–492, 1979.

C.P. Yu and C.K. Diu. A probabilistic model for intersubject deposition variability of inhaled particles. *Aerosol Science Technology*, 1:335–362, 1982.